

University of Southampton Research Repository

Copyright © and Moral Rights for this thesis and, where applicable, any accompanying data are retained by the author and/or other copyright owners. A copy can be downloaded for personal non-commercial research or study, without prior permission or charge. This thesis and the accompanying data cannot be reproduced or quoted extensively from without first obtaining permission in writing from the copyright holder/s. The content of the thesis and accompanying research data (where applicable) must not be changed in any way or sold commercially in any format or medium without the formal permission of the copyright holder/s.

When referring to this thesis and any accompanying data, full bibliographic details must be given, e.g.

Thesis: Author (Year of Submission) "Full thesis title", University of Southampton, name of the University Faculty or School or Department, PhD Thesis, pagination.

Data: Author (Year) Title. URI [dataset]

University of Southampton

Faculty of Medicine

Cancer Sciences

Inertial Microfluidic Circuits for Investigating Receptor Activation Dynamics

by

Marios Stavrou

Thesis for the degree of Doctor of Philosophy

University of Southampton

Faculty of Medicine

Cancer Sciences

Inertial Microfluidic Circuits for Investigating Receptor Activation Dynamics

by

Marios Stavrou

Thesis for the degree of Doctor of Philosophy

Supervisors
Dr. Jonathan J. West
Prof. Donna E. Davies

University of Southampton

ABSTRACT

Faculty of Medicine

Cancer Sciences

Inertial Microfluidic Circuits for Investigating Receptor Activation Dynamics

Marios Stavrou

The ErbB family of receptor tyrosine kinases members comprises epidermal growth factor receptor (EGFR), ErbB2, ErbB3 and ErbB4. These receptors recognize external cues (ligands) and subsequently undergo signal transduction that direct the downstream activation of other proteins such as GRB2 and Shc in the signalling cascade and ultimately direct cell fate. Ligand binding induces conformational changes, receptor dimerization and autophosphorylation. Current techniques lack the temporal resolution required to observe receptor activation dynamics that occur over sub-second timescales. Traditionally, quench flow analysis has been used. However, this approach involves turbulent flows that disrupt the cell membrane. Microfluidics involves gentle, laminar flow and has been used for rapid whole cell quench flow analysis to reveal new insights into EGFR autophosphorylation dynamics (Chiang Y. and West J. Lab Chip, 2013, p.1031). In my PhD, I have developed a novel platform based on inertial microfluidics coupled with Dean flow principles. High velocities (m/s) transport within microfluidic channels was used to focus cells to lateral positions within the ligand streams in less than a millisecond (0.5 ms), followed by a curved incubation channel where Dean forces drove cells to a common position, to produce a uniform cell velocity and thus uniform incubation times (CV = <5%). The cells were transported to a second inertial focusing channel and were laterally focused into a quench buffer in order to preserve the receptor intermediates for analysis by multiplexed flow cytometry. The novel microfluidic device successfully monitored the early dynamics of EGFR signalling (25-2000 ms) and unravelled new information on the phosphorylation of two important tyrosine residues, Y1068 and Y1173, found on the EGF receptor. The Y1068 was characterized by high levels of phosphorylation compared to the levels of Y1173 in the sub-second time window. These findings can be used for identifying potential therapeutic targets.

Table of Contents

ABSTRACT	4
Table of Contents.....	5
Research Thesis: Declaration of Authorship	8
Acknowledgements.....	9
Definitions & Abbreviations.....	10
1. Introduction	12
1.1 Receptor Biology	12
1.1.1 EGFR	12
1.1.2 HER-2.....	14
1.1.3 HER-3.....	14
1.1.4 HER-4.....	15
1.1.5 Epidermal Growth Factor Receptor (EGFR) structure.....	16
1.1.6 Ligands of the ErbB family	19
1.1.7 Epidermal Growth Factor Receptor (EGFR) signal transduction.....	20
1.1.8 Early phosphorylation events of Epidermal Growth Factor Receptor (EGFR) ...	22
1.2 Conventional techniques for investigating EGFR signalling	26
1.2.1 X-ray.....	26
1.2.2 Mass spectrometry.....	27
1.2.3 Fluorescence Resonance Energy Transmission (FRET) &.....	27
Fluorescence-Lifetime Imaging Microscopy (FLIM).....	27
1.3 Investigating receptor activation dynamics with stopped and quench flow dynamics.....	29
1.4 Microfluidics.....	32
1.4.1 Active Methods	32
1.12.2 Optical and optoelectronic tweezers	34
1.4.2 Passive methods	39
1.4.3 Inertial microfluidics	44
Reynolds number (Re) and particle Reynolds number (Rp)	45
1.5 Aims.....	48
2. Materials and Methods	49
2.1 Concept and Design.....	49

2.1.1 Inertial Microfluidics	49
2.1.2 Dean Flow	49
2.1.3 Hydraulic Resistance	49
2.2 Dimensions of time machines versions 1.0, 1.5 and 2.0.....	52
2.3 Microfluidic device manufacturing	56
2.3.1 PDMS microfluidic device replication.....	56
2.3.2 Polyurethane master moulds	56
2.3.3 Device packaging.....	56
2.4 Microfluidic operation.....	57
2.4.1 Microfluidic hardware	57
2.4.2 Sample preparation (polystyrene particles) and density matching.....	59
2.4.3 Fluorescence microscopy	59
2.4.4 Quantitative image analysis to identify particle/cell position	59
2.5 Cell culture.....	62
2.6 Western blot analysis.....	63
2.7 Flow cytometry.....	67
2.8 Gating strategy for cell membrane integrity and cell receptor analysis	69
2.9 Cell viability assay - Propidium Iodide (PI).....	70
2.10 Cell stimulation, intracellular staining and Flow cytometry	70
2.11 Statistical analysis.....	74
3. Results – Chip optimization and evaluation	75
3.1 Microfluidic circuit development and characterisation	75
3.2 Determination of the optimal dimensions for the inertial focusing element.....	75
3.3 Investigating the effect of channel miniaturisation	80
3.4 A new microfluidic circuit to improve focusing and obtain shorter switch times	81
3.5 Cell viability is not affected by inertial microfluidic transport	85
3.6 Assessing the reproducibility of cell incubation times.....	85
3.7 The aspect ratio of the incubation channel influences incubation time control	89
3.8 Velocity and positional evolution before and after each curvature of the incubation channel	92
3.9 Validating microfluidic resistors for removing non-focussed cells	99
3.10 Methanol based fixation causes air pocket formation and clogging of the microfluidic device.....	106
4. Results on phosphorylation studies	110
4.1 Validation of antibodies by Western blot analysis.....	110
4.2 Establishing a flow cytometry methodology for measuring EGFR phosphorylated tyrosine residues.....	117
4.3 Investigating EGFR phosphorylation levels in the sub-second time window.....	123
5. Conclusion and future work.....	135

5.1 Poor temporal resolution characterises the conventional techniques used for studying EGFR phosphorylation dynamics	135
5.2 The development of a circuit based on the inertial microfluidics coupled with Dean flow allowed sub-second cell stimulation and quenching.....	136
5.3 The Inertial microfluidics coupled with Dean flow surpasses the limitations of other microfluidic techniques	136
5.4 Capturing early phosphorylation events of EGFR in sub-second time resolution	137
5.5 pY1068 phosphorylation levels are higher compared to pY1173 not only in longer stimulation but also in sub-second stimulation times.....	138
5.6 Future work.....	139
5.7 Conclusions	141
6. References.....	142

Research Thesis: Declaration of Authorship

Print name: Marios Stavrou

Title of thesis: Inertial Microfluidic Circuits for Investigating Receptor Activation Dynamics

I, Marios Stavrou declare that this thesis and the work presented in it is my own and has been generated by me as the result of my own original research.

I confirm that:

1. This work was done wholly or mainly while in candidature for a research degree at this University;
2. Where any part of this thesis has previously been submitted for a degree or any other qualification at this University or any other institution, this has been clearly stated;
3. Where I have consulted the published work of others, this is always clearly attributed;
4. Where I have quoted from the work of others, the source is always given. With the exception of such quotations, this thesis is entirely my own work;
5. I have acknowledged all main sources of help;
6. Where the thesis is based on work done by myself jointly with others, I have made clear exactly what was done by others and what I have contributed myself;
7. Either none of this work has been published before submission, or parts of this work have been published as: [please list references below]:

Signature:

Date:

Acknowledgements

Firstly, I would like to thank my supervisor Dr. Jonathan J. West and Professor Donna E. Davies for their continuous support, advices, feedback and motivation in order to complete my PhD study.

My sincere thanks also goes to Dr. P. Holloway, Dr. M. Hedge and Dr. J. Butement, Dr. R. Mingels, K. Muller, Dr. C. Honrado and the others in CHB lab for always being there for me.

Brook Lab will always be in my heart for supporting and motivating me (special thanks to Natalie, Franco and Rob).

Special thanks to my friends Aris P., Aris A., Nikos P., Marios K., Marios A. Marios K., Panos E., Panayiotis G. and Mike H. for all the fun.

Last but not the least, I would like to thank my family and my girlfriend Stella for their long lasting support through the years even in my difficult times.

“Don’t give up. Push through the droughts. Channel the inevitable disappointments back into your craft. Break molds. Think. Create. But most importantly, stay alive. And in the meantime, make it about others. That seems to work. Stay strong. Live on. And power to the local dreamer.” - Tyler Joseph

Definitions & Abbreviations

Akt	Protein Kinase B
APC	Allophycocyanin
ATP	Adenosine triphosphate
AREG	Amphiregulin
BSA	Bovine serum albumin
BTC	Betacellulin
CHO cells	Chinese hamster ovary cells
CTCs	Circulating tumour cells
CV	Coefficient Variation
DEP	Dielectrophoresis
Dh	Hydraulic diameter of channel
DLD	Deterministic lateral displacement
DMEM	Dulbecco's modified eagle medium
DNA	Deoxyribonucleic acid
EGF	Epidermal growth factor
EGFR	Epidermal growth factor receptor
ERK	Extracellular signal-regulated kinases
ERPA	Extended range proteomic analysis
FBS	Foetal bovine serum
FITC	Fluorescein isothiocyanate
FLIM	Fluorescence lifetime imaging
FRET	Fluorescence resonance energy transmission
GdnHCL	Guanidine hydrochloride
Grb2	Growth factor receptor bound protein 2
HER2	Human epidermal growth factor 2
HER3	Human epidermal growth factor 3
HER4	Human epidermal growth factor 4
JNK	c-Jun N-terminal kinase
MAPK	Mitogen-activated protein kinase
MFI	Median fluorescence intensity

MS	Mass spectrometry
PBS	Phosphate-buffered saline
PDMS	Polydimethylsiloxane
PE	Phycoerythrine
PFA	Paraformaldehyde
PFF	Pinched flow fractionation
PI	Propidium iodide
PI3K	Phosphoinositide 3 kinase
PLA	Proximity ligation assay
PTB	Phosphotyrosine-binding
PVDF	Hybond p polyvinylidene fluoride
Re	Reynolds number
Rp	Particle Reynolds number
SDS	Sodium dodecyl sulfate
SSAW	Standing surface acoustic waves
STE	Stream thinning elements
TBS	Tris-buffered saline
TBST	Tris-buffered saline Tween
TGF- α	Transforming growth factor alpha
TIPY-MS	Tandem immunoprecipitation-mass spectrometry
VEGF	Vascular endothelial growth factor

1. Introduction

The ability of cells to communicate and interact with the environment is a fundamental process in biology. Receptors reside on cell surfaces in order to receive external signalling molecules called ligands. Signal transduction initiates upon ligand interaction with the binding domain of the receptor, subsequently leading to conformational and biochemical changes that initiate signalling pathways that control cell fate such as cell growth and apoptosis. Structural biology (e.g. X-ray crystallography) provides ultra-high resolution protein shape information. However, it does not provide any information on the intermediate states during signal transduction and cannot be used to characterize entire membrane-tethered proteins. Resolving the dynamics and mechanisms of receptor signal transduction requires the development of new high speed processing techniques that can manage membrane-tethered receptors.

1.1 Receptor Biology

Receptors are usually composed of an extracellular, a transmembrane and an intracellular domain. Ligands bind the extracellular ligand-binding domain of the receptor and cause direct changes on the intracellular domain of the receptor. These changes induce activation of downstream signalling cascades that lead to cellular responses.³ Such signalling mechanisms are important for normal cell processes such as growth and development. However, abnormal activation leads to a variety of diseases, most notably cancer.¹⁸⁻²⁰

1.1.1 EGFR

Epidermal growth factor receptor (EGFR, HER1) is a tyrosine kinase and cell-surface receptor that belongs to the ErbB receptor family. EGFR activation is involved in normal cell functions. Findings from knockout animal models revealed the importance of EGFR in the development of different organs. Null mutations of EGFR are embryonic lethal due to malfunction and developmental abnormalities of lungs, pancreas and the central nervous system.²¹ As well as controlling lung development, EGFR activation leads to upregulation of genes associated with goblet cell differentiation and mucin production in airway epithelial cells *in vitro*.²² Abnormal expression of EGFR and EGF-like ligands leads to carcinogenesis and

progression of various types of carcinomas *via* different mechanisms (inhibition of apoptosis, activation of angiogenesis, cell proliferation).^{23 24}

EGFR was discovered in 1975 by binding ¹²⁵I-labelled EGF to the surface of fibroblasts.²⁵ EGFR is a transmembrane 170-kDa protein and is heavily N-glycosylated to promote protein-protein interactions (ligand-receptor interactions), while also affecting the 3D configuration feature that is essential for signal transduction. The human EGFR gene is ~200kb and is composed of 28 exons and 27 introns. It is found on chromosome 7 (7p12). The extracellular domain is encoded by exons 1-6, exon 17 encodes for the transmembrane domain and exons 18-28 encode for the intracellular domains. The tyrosine kinase domain is encoded by exons 18-24 while exons 25-28 encode for the cytoplasmic domain of the receptor where the tyrosine residues are located (Figure 1).¹⁵

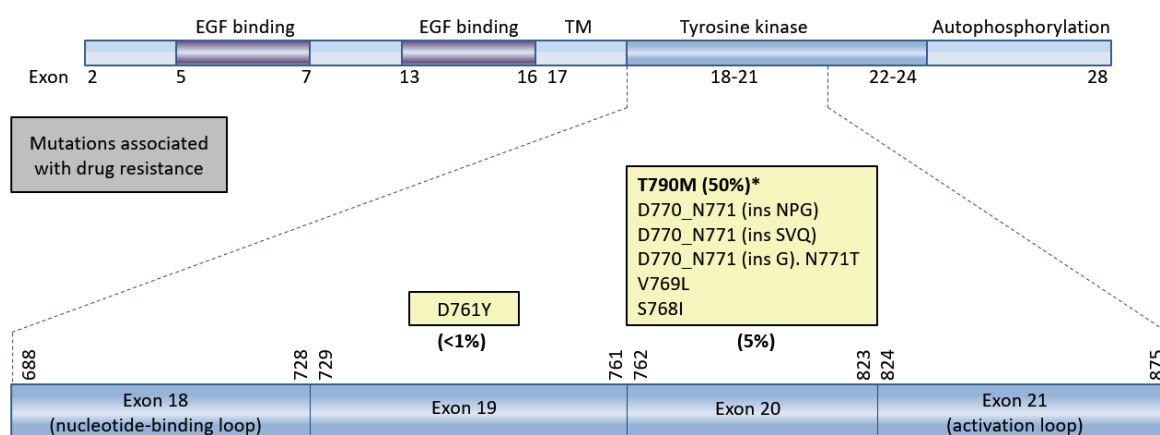


Figure 1. EGFR structure with the important tyrosine residues and the most common mutation sites. Adapted from Sharma *et al.*, 2007.¹⁵

The ErbB receptor family is composed of four different members: EGFR, HER-2, HER-3 and HER-4 (Figure 2). The intracellular tyrosine kinase domain is highly conserved in the majority of ErbB receptors (EGFR, HER-2, HER-4). However, HER-3 lacks tyrosine kinase activity due to substitutions of important amino acids and therefore, it is unable to autophosphorylate. The extracellular domains of the ErbB receptors are less conserved indicating that they have different ligand binding specificity.^{26 27}

1.1.2 HER-2

HER-2 is a major partner of EGFR for the formation of heterodimers. Heterodimer complexes EGFR-HER-2 are more stable at the cell surface compared to complexes containing other ErbB members (EGFR-HER-3 or EGFR-HER-4). HER2 is not able to accept any ligand (Figure 2).³ However, when it is in complex with EGFR, it causes decreased ligand dissociation. This leads to longer activation of the EGFR associated signalling pathways. Another feature that characterizes EGFR-HER-2 heterodimers is the ability to remain on the cell surface for longer periods of time and subsequently undergoing endocytosis at slower rates than the EGFR homodimers.²⁸ In addition, EGFR-HER-2 heterodimers are recycled to the cell surface. However, this is not observed with the EGFR homodimers that are degraded by the cell.²⁸

1.1.3 HER-3

HER-3 is a protein composed of 1342 amino acids (aa). Neuregulins are the ligands that bind this receptor in order to activate it. The lack of an active kinase domain is due to the evolutionary divergence at important amino acid residues of the kinase domain leading to an inactive conformation. However, HER-3 acts as an allosteric activator and signalling substrate after dimerization with the other members of the ErbB family.²⁹

The 14 tyrosines found in the C-tail of HER-3 serve as docking sites for PTB and SH2 binding proteins which are involved in various intracellular signalling pathways (e.g. PI3K and Akt signalling pathways). The formation of HER-3 heterodimers grants oncogenic capabilities to the other ErbB kinase active members, which can exploit this activity for survival. Therefore, HER-3 heterodimers are associated with resistance to HER-2 and EGFR inhibitors in HER-3 driven breast cancer and lung cancer, respectively.³⁰

1.1.4 HER-4

HER-4 is a member of the ErbB receptor tyrosine-kinase family and a partner of EGFR in the formation of an EGFR-HER4 heterodimer. HER-4 has an important role in the development of cardiovascular and nervous system. HER-4 knock-out mice survived until their embryonic day 10.5 because of abnormalities in the hindbrain and their cardiac trabeculae. HER-4 had been found to be upregulated in 30% of the breast cancer patients causing increased proliferation, migration and metastasis.³¹

Each of the ligands associated with the ErbB receptors induce different biological potencies in a cell by preferential recruitment of different signalling molecules (Figure 2). For example, the ligands involved with HER4 can induce similar level of tyrosine phosphorylation compared to the ligands involved with the other ErbB members. However, phosphorylated tyrosine residues in the receptor differ with each ligand.

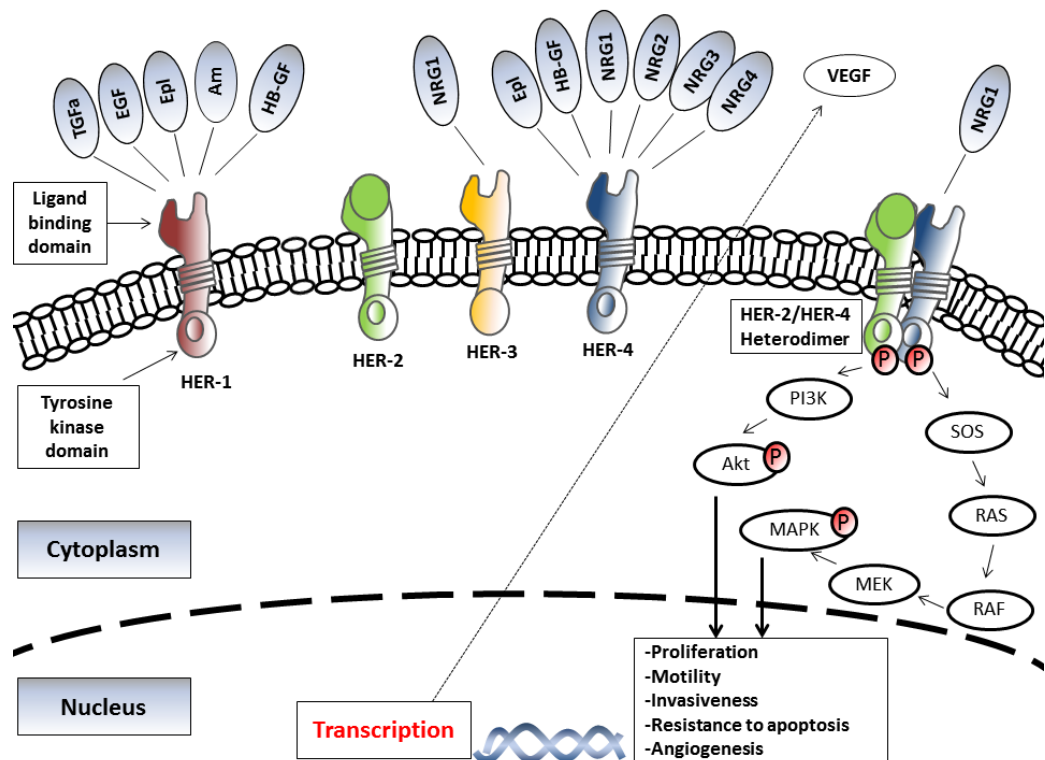


Figure 2. ErbB family members with their associated ligands stimulate or inhibit the downstream signalling pathways. HER-2 does not have an associated ligand and HER-3 does not have a tyrosine kinase domain. HER-2 heterodimers promote cell proliferation, motility, invasiveness and resistance to apoptosis. EGFR signalling is associated with increased production of proangiogenic factors and VEGF in tumours. Adapted from Burgess *et al.*, 2003.¹³

1.1.5 Epidermal Growth Factor Receptor (EGFR) structure

EGFR is composed of an extracellular ligand-binding domain, a hydrophobic transmembrane domain and a cytoplasmic tyrosine kinase domain.^{26 32} The extracellular region of EGFR is composed of four different domains (DI, DII, DIII, and DIV). Domain I and III are essential for the binding of the ligand to the receptor. Domains II and IV are cysteine rich domains that have disulphide-bonded modules essential for the formation of the dimerization arm with another EGFR monomer (homo-dimerization) or monomers from the other members of the ErbB family (hetero-dimerization). Dimerization activates the kinase domain and subsequently autophosphorylates multiple tyrosine residues found on the C-terminal (~190 a.a) of EGFR (Figure 3).² It is well known that the tyrosine residues of a monomer are *trans*-phosphorylated by the tyrosine kinase of the receptor pair subsequently, leading to the phosphorylation of the cytoplasmic proteins required for the activation of the downstream signal transduction cascades e.g. ERK/MAPK pathway, Akt and JNK pathways are associated with DNA synthesis and cell proliferation.³³ These pathways control phenotypes such as cell migration, adhesion and proliferation (Figure 4).^{2 34 35} The role of these tyrosine residues had been found to be fundamental for the regulation of receptor activation and signal transduction.²⁶ However, the sequence of events (e.g. autophosphorylation) that occur during receptor activation that drives signal transduction are poorly understood due to the low temporal resolution that characterize these events and the limitations of the conventional techniques to capture them.

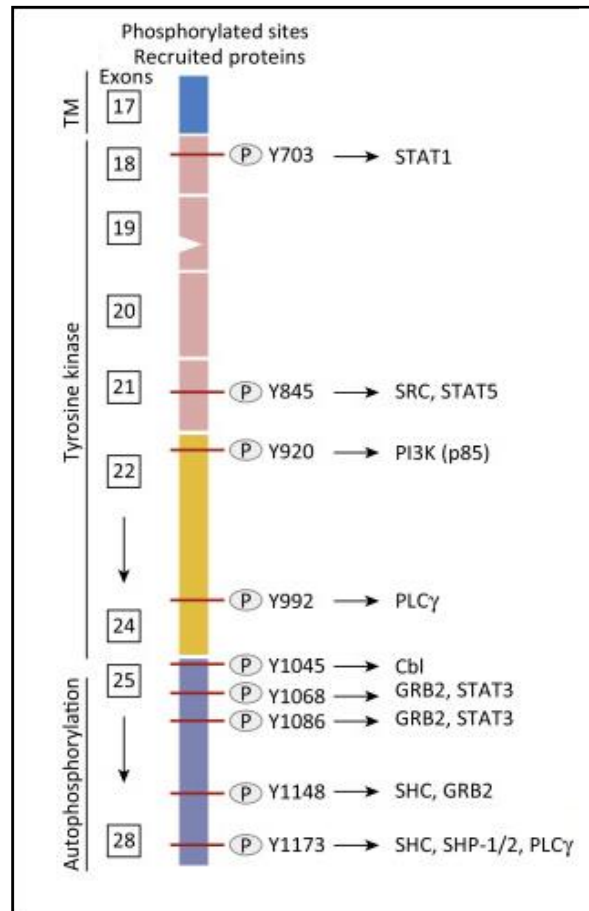


Figure 3. Proteins associated with specific tyrosine residues on phosphorylated EGFR. These proteins use the tyrosine residues as docking sites in order to become phosphorylated and subsequently induce downstream signalling cascades. From Shostak and Chariot, 2015.²

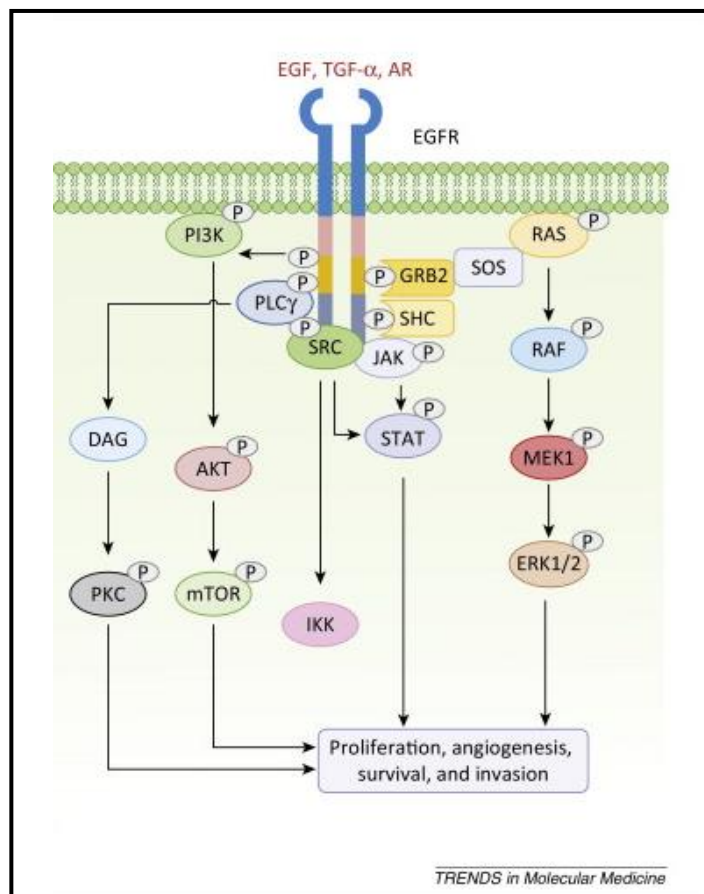


Figure 4. The most important signalling pathways and associated biomolecules that are activated upon EGFR dimerization and autophosphorylation. These pathways are involved in several cell processes (e.g. proliferation, angiogenesis, survival and invasion). From Shostak and Chariot, 2015.²

1.1.6 Ligands of the ErbB family

The EGF receptor has seven different ligands. As we know, EGF receptor exists primarily as a monomer. The binding of a ligand cause the receptor to undergo a substantial conformational change allowing dimerization with a second EGFR monomer. The seven ligands can be divided based on their affinity for the ErbB family members. EGF, TGF- α , AREG and epigen bind only to EGF receptor. BTC, heparin-binding EGF and epiregulin bind ErbB4. The EGF, TGF- α , BTC and heparin-binding EGF have affinities of 0.1-1 nM. On the other hand, AREG, epiregulin and epigen exhibit affinities 10-100 fold lower than the previously mentioned ligands. It shows clearly that there is a variation in receptor affinity and specificity. In addition, these different ligands have been found to induce different biological effects. A study in 32D myeloblast-like cells expressing the EGFR showed that TGF- α and AREG induce higher levels of cell proliferation compared to EGF and heparin-binding EGF.³⁶ Also, EGF stimulation of human fibroblasts leads to cell migration by involving p70^{S6k}. TGF- α causes cell migration through phospholipase C. Furthermore, CHO cells expressing only EGF receptors showed maximal tyrosine phosphorylation within 2 min of stimulation with the four different ligands (EGF, TGF- α , BTC and AREG).³⁶ However, only the EGF, TGF- α , and BTC stimulated twice as much phosphorylation as AREG. The phosphorylation was transient because it got dephosphorylated 5 min after ligand stimulation. On the other hand, phosphorylation caused by AREG declined slower.

1.1.7 Epidermal Growth Factor Receptor (EGFR) signal transduction

Monomers of EGFR are found in a closed, tethered auto-inhibition state, with dimers found in an untethered open state and with conformational changes that are modulated by ligand binding. Various ligands can bind and promote EGFR activation. These include epidermal growth factor (EGF), amphiregulin, transforming growth factor α (TGF- α), heparin binding EGF and epiregulin.³⁷ The binding of EGF and EGF-like ligands to the extracellular domain of the EGF receptor initiates the dimerization of homo- or hetero-dimers of the receptor and leads to the stabilization of the conformation of the extracellular region of the receptor to induce activation of the tyrosine kinase domain for asymmetric intermolecular (*trans*) autophosphorylation.¹⁹ This process is illustrated in Figure 5 and involves the phosphorylation of several tyrosine residues on the cytoplasmic tail of the receptor.⁴ There are ~10 tyrosine residues that become phosphorylated after receptor dimerization.³⁸ The phosphorylated tyrosine residues have an important role as docking sites for proteins (e.g. PI3K, GRB2) that contain Src homology 2 (SH2) and phosphotyrosine binding (PTB) domains (Figure 5).³² These interactions are necessary to elicit downstream signalling cascades such as the MAPK, Akt, and JNK pathways that are involved in DNA synthesis and cell proliferation *via* up-regulation of transcription factors.³⁹ Furthermore, it should be mentioned that the phosphorylation of several tyrosine residues (e.g. Tyr974 or Tyr1045) could have a negative regulatory effect on EGFR, by induction of EGFR endocytosis and EGFR ubiquitilation, respectively. In addition, HER2 overexpression had been found to alter the phosphorylation patterns and favors receptor stability and sustained signalling. This happens when high levels of HER2 block the tyrosine sites (Y1045 and Y1068) on the EGFR which serve as docking sites of c-Cbl and GRB2, respectively. This promotes phosphorylation of Y1173, a docking site of phospholipase C gamma and Gab adaptor proteins. HER2's ability to alter the autophosphorylation pattern on itself and its heterodimerized partner (EGFR) causing an increase on ErbB associated signalling pathways, cell transformation and tumorigenic potency and resisting endocytosis and receptor degradation.^{40 41}

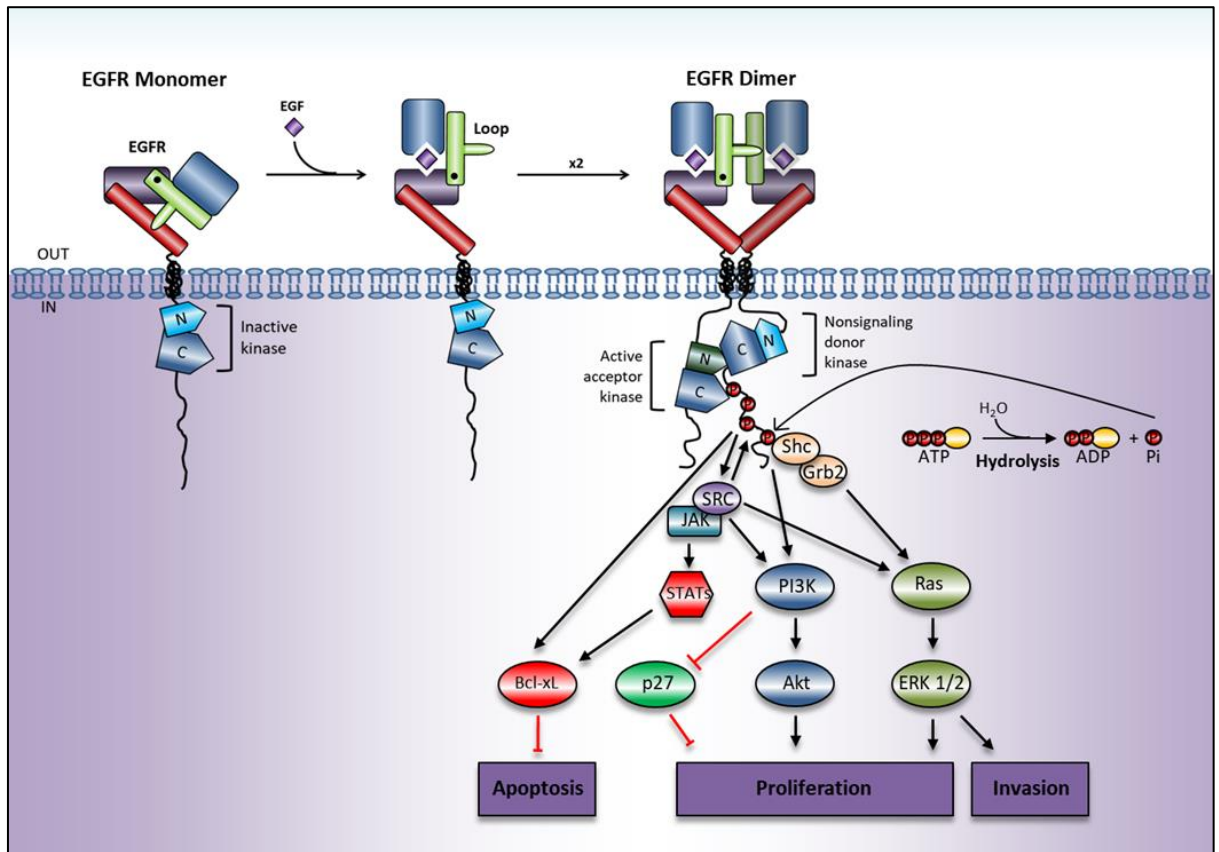


Figure 5. EGFR conformational stages pre-/post-activation by ligand binding followed by ATP hydrolysis, phosphorylation of the receptor tyrosine residues that lead to signal transduction and activation of downstream signalling pathways. Four different domains comprise the extracellular domain of EGFR. Binding of ligand between domain I and domain III induce conformational rearrangements and stabilizes the extended conformation of the extracellular region of the receptor. Subsequently domain II is responsible for the formation of a dimerization arm with another monomer of the receptor. Adapted from Yewale *et al.*, 2013.⁴

1.1.8 Early phosphorylation events of Epidermal Growth Factor Receptor (EGFR)

Moehren and Khololenko in 2002 were the first to study the early phosphorylation events of EGFR and immediate downstream signalling.¹ They were able to examine EGFR phosphorylation by placing the cells into vials with a Teflon stirrer and maintaining the temperature at 37 °C in a water bath. EGF was added by pipetting in order to stimulate the cells' receptors and preserving the reaction by the addition of the quench buffer. The cells were then analysed by Western blotting. They were able to observe that the tyrosine phosphorylation of the receptor reached saturation in 5 s following ligand addition. This was followed by the phosphorylation of downstream signalling proteins (Shc, PI3K and PLC- γ) in 10 s (Figure 6), to infer the sequence within the signalling pathway.

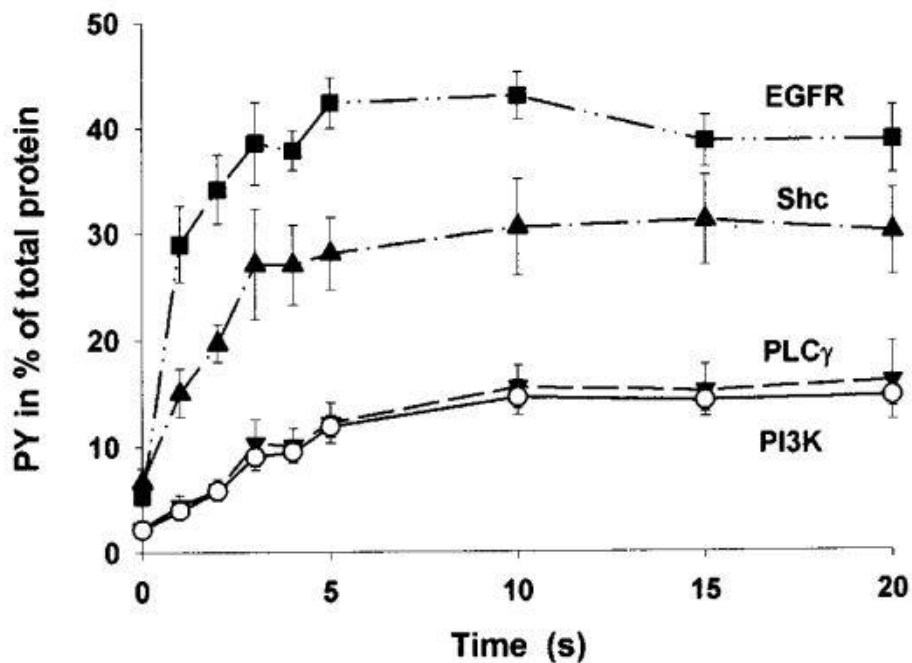


Figure 6. Total phosphorylation of EGFR and its interacting partners at 37 °C. Phosphorylation of EGFR reaches saturation 5 s after stimulation, followed by activation of Shc and then PLC- γ and PI3K. From Moehren *et al.*, 2002.¹

It was the first time that early phosphorylation of EGFR events were recorded in the temporal resolution of a few seconds (1-10 s) and it gave information on the downstream signalling pathways. However, the time required to achieve homogenization of the large volume of reagents (ligand and quench) using a magnetic stirrer is of the order of few seconds. Hence, the stimulation and quench of cells takes longer time to occur, reducing the actual incubation time and the overall temporal precision. This was also confirmed by an experiment using the same mixing methodology. 10 μ L of red dye mimicking the ligand were added into 1.25 mL of water, immediately 3 volumes of water were added to mimic the quench buffer. The time required for complete homogenization of the 'ligand' and the water was in the order of few seconds (3-4 s, Figure 7). In larger volumes, complete homogenization requires longer time scales. Nevertheless, the research by Moehren and Kholodenko demonstrates the value of temporal control for understanding signalling pathways, while also highlighting the need for faster processing techniques with much greater (millisecond) temporal resolution to investigate receptor activation mechanisms.¹

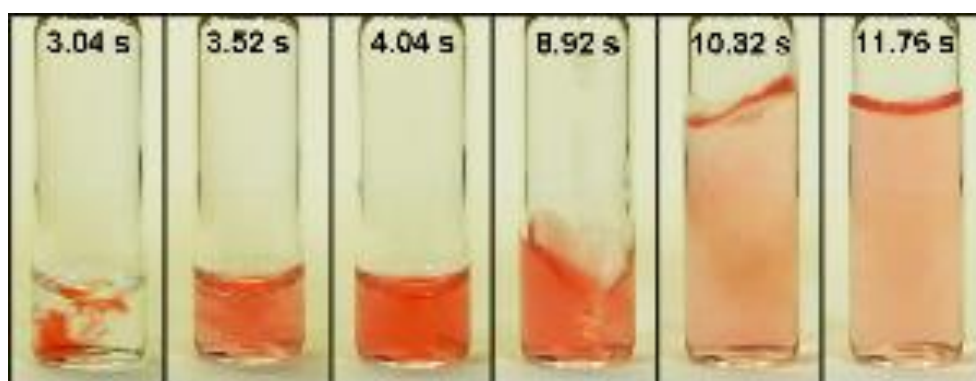


Figure 7. Macroscopic mixing mimicking the methodology used by Moehren and Khololenko, 2002.¹ Red coloured dye ('ligand') was added into water. It took more than 3 s to achieve complete homogenization. When the volume of the water was increased ('quench'), the complete homogenization took even longer. Adapted from Chiang Y.Y.¹³

In 2007, Dengjel and colleagues examined the early phosphorylation events of EGFR by replacing the conventional mixing of cells with the ligand and the quench buffer with the use of a continuous quench flow system. This involved syringe pumps with a so called T-mixer junction for the union of cells with ligands and following incubation in tubing of defined length, a second T-mixer to combine the quench buffer to arrest phosphorylation and preserve reaction intermediates.⁵ The stimulation and quenching time were manipulated by altering the length of the incubation tubing. Quantitative mass spectrometry involving the SILAC method showed that the phosphorylation of three of the tyrosine residues (Y1092, Y1172, Y1197) found on the EGFR c-tail occurs within 5-10 s after the stimulation of cells (Figure 8). These data shows that the phosphorylation rate compared to the ones obtained by Moehren and Kholodenko is slower.¹ However, on closer inspection of the supplementary data it is evident that only a small fraction (1:10 ratio) of the cells are stimulated (SI fig2).⁵ To understand this, the experiment was replicated with the same bore tubing and flow conditions using red dye to observe the laminar, non-turbulent streams (Figure 9).

At these large scales, it is evident that the cells were not mixed with the ligand and the quench buffer because the mixing was diffusion-dependent due to the laminar flow that occurs within the tubing. Therefore, only a small portion of the cell population was stimulated and quenched, and for many at sub-saturation ligand concentrations due to diffusion. Both methods were important for the study of EGFR phosphorylation events. However, they are not capable of achieving sub-second time resolution and they lack incubation control because of the asynchronous stimulation and quenching approaches. Also, they do not have uniform incubation velocities due to the velocity parabola in laminar flow systems.

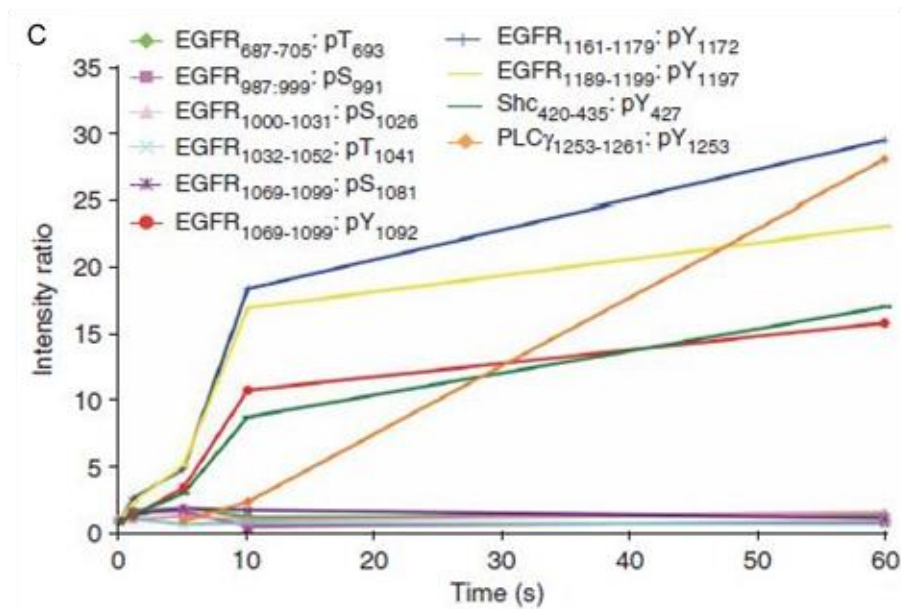
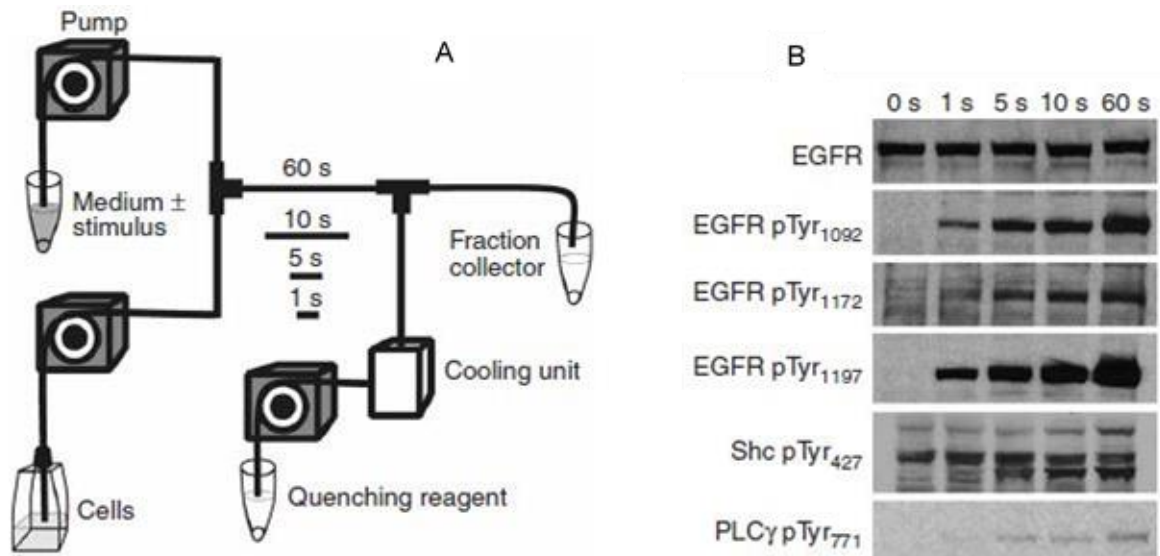


Figure 8. Continuous quench flow system set up that had been used to investigate early cell signalling events (qPACE) (A). Western blotting analysis was used to examine the phosphorylation of various tyrosine residues on the EGFR and downstream signalling partners *e.g.* Shc and PLC γ (B). Mass spectrometry was used for the analysis of the samples collected from the qPACE. Shc phosphorylation was found to occur at the same time as the phosphorylation of the tyrosines on the EGFR, 5 s after stimulation with the EGF (C). From Dengjel *et al.*, 2007.¹⁵

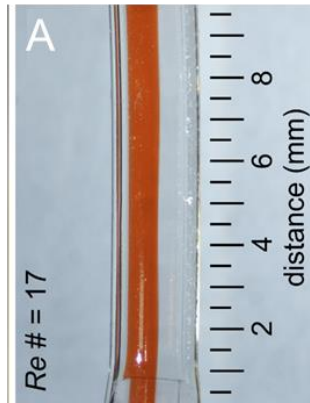


Figure 9. Laminar flow observed in a bore tubing with $Re \# = 17$ (A) to replicate the experiment of Dengjel *et al.*, 2007.⁵ Mixing is only limited by diffusion in the space where the two laminar flow streams meet.

1.2 Conventional techniques for investigating EGFR signalling

There are a number of methods for studying EGFR activation and each method can reveal different types of information. For example, Western blotting analysis can be used to obtain information on the molecular weight of proteins, complexes and activated states and also to identify post-translational modifications such as phosphorylated residues. The conventional techniques such as X-ray crystallography, Mass spectrometry, FRET & FLIM will be discussed in this chapter.

1.2.1 X-ray

In addition, X-ray crystallography had been used to examine EGFR structure with atomic resolution, and infer conformational changes and the function of its domains during the receptor's monomer and dimer state.^{42 43} X-ray crystallography has also been used to reveal information on how mutations of Leu834/Leu837 drive overactivation of EGFR and how different inhibitors (*e.g.* gefitinib) act on the receptor for treatment.⁴⁴ This allowed a great amount of data on EGFR to be obtained. However, this method has some limitations. X-ray crystallography has atomic resolution giving information only on the protein domains of the receptor (crystal form). However, crystallization of the cell membrane is not achievable therefore, it does not give any information on the dynamics of the receptor.

1.2.2 Mass spectrometry

Mass spectrometry had been used to profile the phosphoproteome driven by EGFR signalling in combination with affinity-purification, extended range proteomic analysis (ERPA)^{45 46} or tandem immunoprecipitation-mass spectrometry (TIPY-MS)⁴⁷ were able to identify the EGFR tyrosine residues.⁴⁸ However, mass spectrometry cannot be used to fully characterize EGFR phosphorylation due to the varying stoichiometry and low abundance of the phosphorylation modification, and the limitations of MS sensitivity.⁴⁹ In addition, there is no method to instantly add ligand and immediately stop the reactions. Nevertheless, mass spectrometry is a good technique but need advanced sample preparation methods to allow reaction intermediates, complexes and dynamics to be revealed.

1.2.3 Fluorescence Resonance Energy Transmission (FRET) & Fluorescence-Lifetime Imaging Microscopy (FLIM)

The limitations of the techniques mentioned in section 1.2, 1.2.1, and 1.2.2 (Western blotting analysis, X-ray crystallography and mass spectrometry) led to the development of molecular labels for real time imaging such as fluorescence resonance energy transmission (FRET) and fluorescence-lifetime imaging (FLIM). These imaging methods were developed to quantify the biochemical and spatio-temporal protein-protein interactions (e.g. conformational changes). FRET works when a photosensitive chromophore (donor) transfers energy to a nearby acceptor chromophore (Figure 10).⁵¹

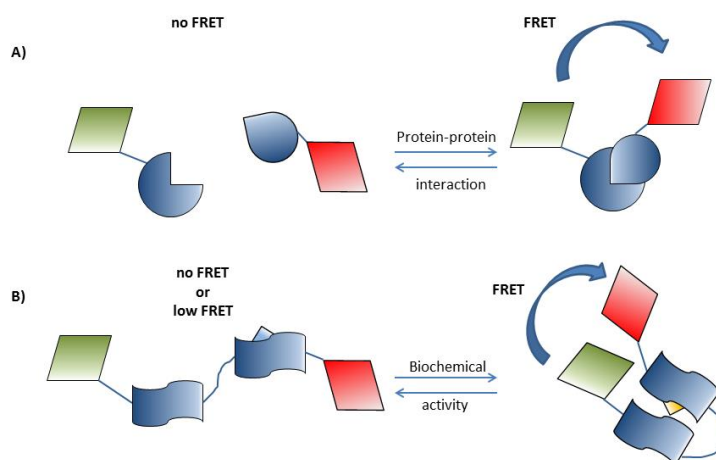


Figure 10. Protein-protein interaction (donor and acceptor) lead to emission of a FRET signal (A), Biochemical interactions can be studied using FRET when the donor and acceptor are in close proximity (B).

FRET involves the following factors: (i) the transfer of energy from the donor to the acceptor is distance-dependent, (ii) the overlap between the donor emission and the acceptor excitation spectra. The distance between the donor and acceptor is called the Forster distance (R_0) and occurs between 2-8 nm (50% FRET).⁵⁰ This method is extremely promising. However, it cannot be used to study large molecule and multiprotein complexes if the fluorescent tags are insufficiently close, because it will emit no signal. In addition, FRET cannot provide the temporal resolution to study the reaction intermediates due to the long exposure times required to obtain enough photons to study the fluorescent decay of FRET using FLIM.⁵¹

Fluorescence lifetime imaging microscopy (FLIM) is used to measure the lifetime of the fluorescent event (*e.g.* the time required for the fluorophore to become excited and then dropping to the ground state). For nearly all the fluorophores, the rate of the energy transfer to the environment is depending on the concentration of the various factors such as oxygen, ions, pH value and the proteins found in the cell which are known as fluorescent quenchers.⁵² FRET/FLIM require the use of receptor constructs that are fused with fluorescent peptides (*e.g.* GFP) which are prepared by molecular cloning. These labels require sensitive detectors and long exposure times. Therefore, they do not have the temporal resolution to examine these millisecond scale intermediate reactions (*e.g.* EGFR autophosphorylation).

All the methods mentioned in section 1.2.1-1.2.3 are extremely promising and they had been used for the study of biological reactions. However, they are not able to immediately deliver ligands to cell surfaces hence, they are not able to achieve high temporal resolution (sub-second time points). A method able to immediately deliver ligands to cells, giving accurate control of cell incubation in the ligand, quench the reaction and preserving the intermediate reactions (sub-second) for further off-line analysis using techniques such as Western blotting analysis, fluorescence microscopy, mass spectrometry and flow cytometry is essential.

An interesting methodology was used by Reynolds and colleagues in 2003 to study the lateral signal propagation of EGFR activation by stimulating MCF 7 breast cancer cells using low or high density EGF-beads for 2 min.⁵³ The low-density EGF-coupled beads were able to cause an increase in the phosphorylation tyrosine levels of EGFR but only at the bead contact point. On the other hand, high-density EGF-coupled beads were able to cause an increase of EGFR phosphorylation through

the whole plasma membrane. This experiment showed that a density threshold of EGF is required in order to reach phosphorylation propagation. Contact can be confirmed by visualisation but the drawback is the low throughput (1 cell at a time) and it is only involving focal/point stimulation so they observed receptor recruitment and dimerization and its signalosome assembly which is driven by diffusion in that particular area of the membrane. Therefore, this methodology cannot be used to understand the phosphorylation activation dynamics of EGFR because it does not have the temporal resolution required to transport the ligand in milliseconds, efficient whole cell incubation and quench of the reaction.

In addition, cell-based assays using fluorescent lifetime on cells were able to reveal information on the spatial changes of the receptor during its phosphorylation states. Both immunoblotting and cell-based assays are incapable of capturing the dynamic events of tyrosine kinase activation in a single cell that occur in millisecond-scale range. The sequence of events, the mechanism, underpinning the activation of EGFR has not been identified due to the low temporal resolution of conventional methods for changing the biochemical environment around cell membranes. The use of magnetic stirring can only attain mixing times of the order of a second, far exceeding the millisecond-scale processes involved in receptor activation. Thus, the development of new techniques with high temporal resolution are required to study the biochemical, conformational and dimerization mechanisms involved in receptor activation.

1.3 Investigating receptor activation dynamics with stopped and quench flow dynamics

Biochemical kinetics were studied using stopped flow technology in order to rapidly initiate chemical reactions such as polymerization or enzyme kinetics.^{54 55} Figure 11 shows how stopped flow technology works. Two syringes containing the samples (e.g. enzyme and substrate) are driven at high velocity and mixed by turbulence in a chamber. The mixture flows into an observation cell that is connected with a stop-syringe. Optical recording begins when the stop-syringe is filled by the activation of an acquisition trigger. The most common method to capture the optical signal is by the use of photometric detectors such as UV/Vis or fluorescence detectors (more

sensitive). In addition, circular dichroism had been used for the study of protein folding obtained by the use of the stopped-flow method. These two methods had been used for the study of lysozyme.⁵⁶ Lysozyme was firstly denatured by guanidine hydrochloride (GdnHCL) in order to induce unfolding of the protein. The backbone secondary structure was measured by the far-UV circular dichroism band (222 nm) and the side chain tertiary structure was measured by the near-UV circular dichroism.⁵⁷ The time resolution of this method is known as the dead time (the time the reactant is added until the time the switch is triggered) with typical instruments providing a dead time of 1-2 ms and more advanced systems providing 250 μ s dead times.

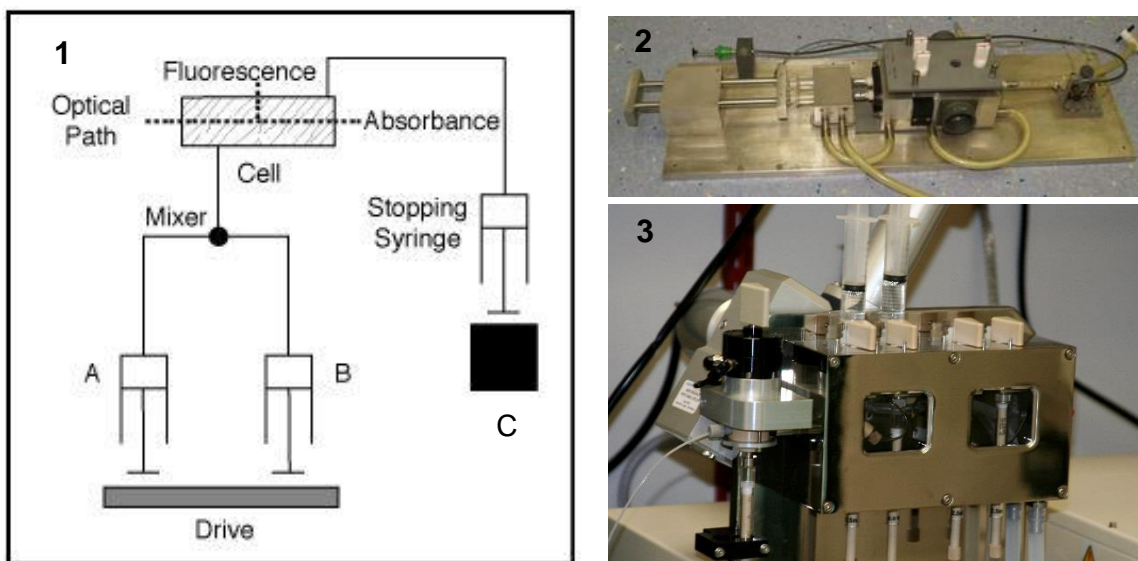


Figure 11. Diagram of a stopped flow instrument (1), syringe A contains the enzyme and syringe B the substrate. The syringes are driven by a syringe drive ram and the samples are transported to a mixer at high velocity. The mixing of the samples stop when the stopping syringe is filled and stopped by the trigger-switch (C). The fluorescent signature of the reaction within the mixing chamber can be detected by adding a fluorescence detector. Laboratory set up used for examining the kinetic resolution of a conformational transition and the ATP hydrolysis step of a Dictyostelium Myosin II mutant (2).⁶ Adapted from www.actin.aok.pte.hu (A), www.le.ac.uk (B), adapted from Wladimir Labeikovsky – Flickr (C).

Quench flow analysis is an extension of the stopped flow technique when there is an absence of a distinct optical signature for measuring reaction state and progress. Quench flow analysis involves, like stopped flow analysis, high-speed turbulent

mixing of reagents followed by introduction into a delay line, with the length and velocity determining the incubation time, after which a second high-speed turbulent mixing process is used to mix a quench buffer, to arrest the reaction. The preserved reaction states are retrieved for off-line analysis using any number of techniques, from mass spectrometry to antibody labelling. By using multiple runs, each with different incubation times, the kinetics and dynamics of the biomolecular reactions can be determined. However, stopped and quench flow techniques require turbulent mixing and associated high Reynolds numbers ($>10,000$, see 1.4.3 section). Turbulent mixing cannot be used to investigate reactions in whole cells, such as is required to investigate receptor activation and signal transduction within the bilayer membrane. Here, the high shear turbulent conditions tear the cell membrane and damage associated processes.⁵⁸

A quench flow device was developed and used for rapid mixing and freezing of cells with millisecond range time resolution and dead time of ~ 30 ms in order to study the synchronous exocytosis in paramecium cells. A biological event that was not easy to examine due to the short life-time and the low frequency of membrane fusion events. *Paramecium tetraurelia* is a ciliated protozoan that have >1000 secretory vesicles on its plasma membrane. These secretory vesicles were rapidly stimulated with aminoethyl dextran and immediately frozen with liquid propane (< -180 °C) to fix the dynamic events that occur in millisecond range scale (~ 30 s membrane fusion). Cell damage induced by this procedure (quench flow) is avoided due to the use of *Paramecium tetraurelia* which has a ragged waxy pellicle that prevents cell damage in turbulent flow.⁵⁹ This characteristic tough outer wall (pellicle) protects against the strong shear forces that occur during quench flow compared to the delicate bilayer membrane of mammalian cells that cannot withstand these forces. Therefore, in order to study the dynamics of mammalian receptors, a gentle cell handling approach is required in order to prevent cell membrane disruption but must also allow rapid interactions between cells and ligands and the rapid arrest of the reaction. For the study of the biological reactions that occur within a few milliseconds, time precision is a major issue. Conventional techniques in the lab such as pipetting or mixing are not sufficiently rapid to provide the temporal control. Therefore, breakthrough technologies such as microfluidics have the potential to be applied to the challenge.

1.4 Microfluidics

Microfluidics is the science and technology of precise manipulation and processing of small volumes of fluids (μL , nL and pL) using channels with dimensions of tens to hundred micrometres and giving laminar flow. The microfluidic systems are mainly replicated in the polymer- polydimethylsiloxane (PDMS). The absence of conventional techniques that can manipulate and analyse single cells is a drawback for science. However, this is where microfluidics can be used as a powerful tool for scientists worldwide in order to accomplish these tasks.⁶¹

1.4.1 Active Methods

Droplet microfluidics have been used to mix reagents within milliseconds.¹¹ Convective mixing occurs inside the moving droplet and it is in the order of ~ 2 ms (Figure 12 A).¹¹ For processes that do not have fluorescent reporters this approach is currently unfeasible for those requiring absorbance or Raman sensing. In addition, complex reactions, such as receptor activation in membranes, a continuous quenched flow approach is required. One of the most common characteristics of droplet microfluidics is the use of surfactant to stabilize the oil-water interface to avoid destruction of the droplets by shear forces while they are rapidly transported. However, the use of surfactants prevents the fusion of the droplets. Thus, it makes quench reactions for preserving any biological reactions impossible. Ignoring the use of surfactant, it allows droplet fusion by either altering the surface energy patterns (e.g. a part of the channel is hydrophilic allowing droplet fusion. However, it should be mentioned that having hydrophilic and hydrophobic regions in the same device is hard to fabricate (Figure 12 B).¹⁶ The time required to fuse two droplets is ~ 7 ms. The high throughput and the absence of surfactant lead to the formation of fragmented droplets. The use of surfactant combined with electrical field (electrofusion) has been used to resolve these issues but the electric field may not leave the cell membrane intact (destabilize cell membrane and cause pore formation, Figure 12 C) and this is technically highly demanding.¹⁷ Therefore, a new method where the cells will be displaced into the ligand and the quench buffer in the order of a few milliseconds is essential. As mixing of cells with the ligand and the quench buffer is not efficient under laminar flow conditions, cell displacement (*i.e.* displacement into neighbouring streamlines) can be used as an alternative way to

initiate and arrest cellular processes under laminar flow conditions in a few milliseconds.⁶²

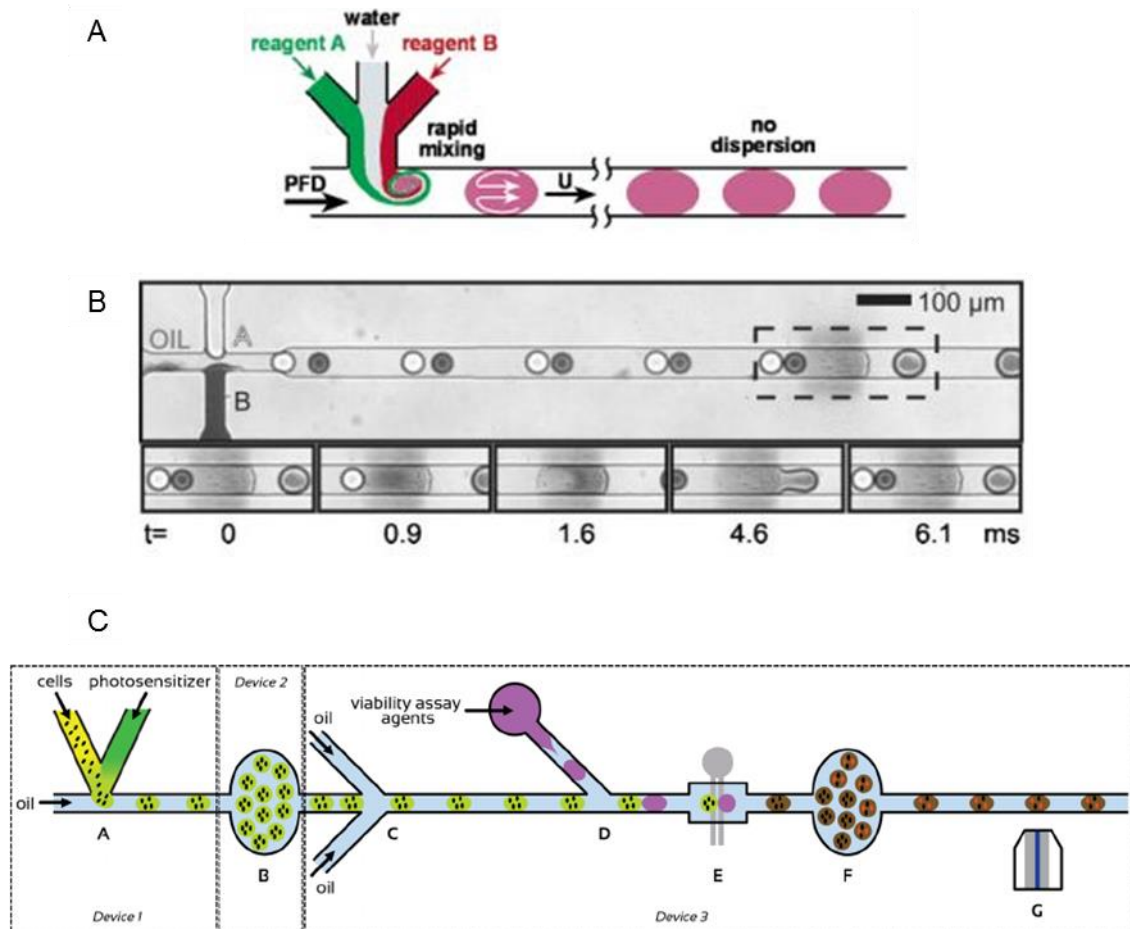


Figure 12. Shear vortices allows rapid mixing of the reagents within the droplets (~ 2 ms) (A). From Song and Ismagilov, 2003.¹¹ Fusion of droplets can be achieved either in a hydrophilic area of the chip (B). From Fidalgo *et al.*, 2007¹⁶ or by applying an electric field to the droplets in order to fused droplets that contain cells and photosensitizer with viability assay agents (C). From Cho *et al.*, 2013.¹⁷

Dielectrophoresis (DEP) is an active microfluidic technique that has been used to manipulate cells and particles. The cells are placed in a non-uniform electrical field where a net force is applied on them leading to cell movement. DC or AC currents can either be used to generate an electric field. DEP can be classified as a positive (pDEP) and negative (nDEP) based on the direction of the cell movement towards or against the high electric field current and the value of the Clausius-Mossotti factor (f_{cm}) (Figure 13). Cell migration is influenced by the electrical permeability of the cells and the fluid. The cells with higher permeability than the fluid migrate towards the field maxima (Positive DEP). The negative DEP is preferable due to the minimal effects on the cell function or viability which can occur in a high electric field. This technique has been used to displace cells into a rhodamine coloured PBS stream and vice versa. The time of the displacement was < 0.5 s.²⁰ However, the switch time is not suitable to study the phosphorylation reaction intermediates of any biological process that occurs in few milliseconds.

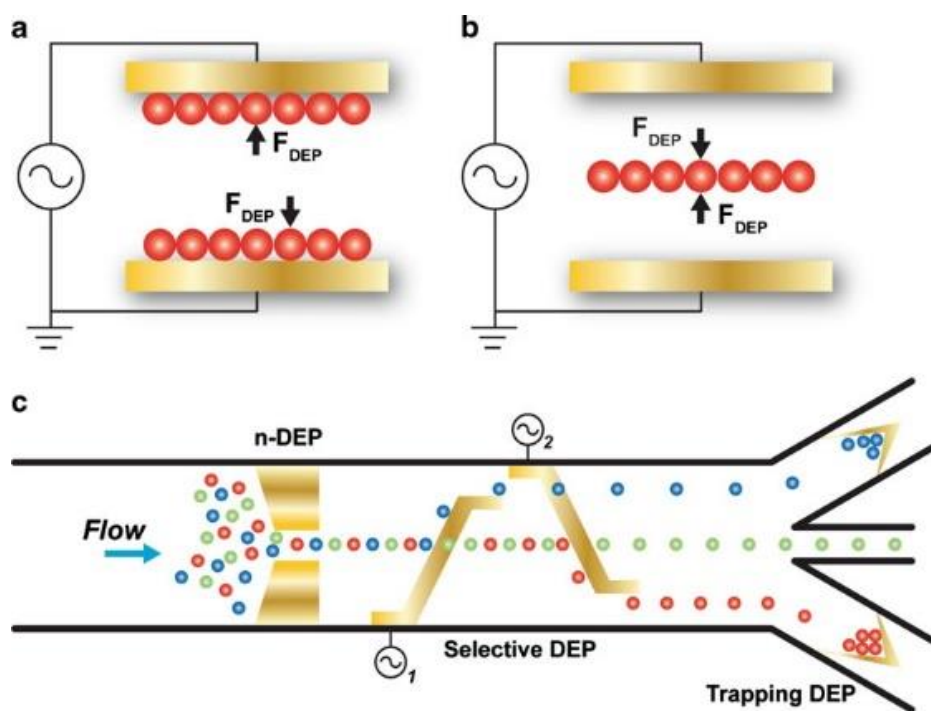


Figure 13. Dielectrophoresis (DEP) can be either positive (a) or negative (b). This influences the position of the particles within the device. In a microfluidic device, both elements can be used to influence the position of the particles and achieve displacement and separation (c). From Gossett *et al.*, 2010.¹²

In addition, optical tweezers are an active technique where light is used to move objects in flows. The use of optical tweezers have been proved excellent for cell manipulation because it allows cell function preservation and precise 3D spatial control. The cell trapping occurs due to a mismatch in the refractive index between the cell and the surrounding fluid. This mismatch gives rise to optical scattering and gradient forces. The optical scattering forces push the objects away from the light source whereas the gradient forces attract the object to the point of the highest intensity produced by the light source (Figure 14). Under these forces the particle is transported towards the beam maxima and it becomes trapped (gradient forces > optical scattering forces). The formed forces are then used to move the objects.⁶³ In one study, yeast cells were transported in saline environment and then back into their media in laminar flow conditions using optical tweezers.⁶⁴ They were able to study osmotic alterations that occur to the yeast cells in a saline environment and their immediate recovery into their medium. Wong and colleagues in 2011 used laser tweezers for an automated cell sorter implemented with Raman spectroscopy which can be used without fluorescent labels (Figure 14).⁶⁵ However, the use of optical tweezers is characterized by slow processing and thus limiting any potential for high throughput cell sorting and in fast flow a lot of light is required to switch cells fast enough but this either fails or is phototoxic leading to cell death. The use of optoelectronic tweezers allow cell trapping, transport and sorting without labels. Optoelectronic tweezers are characterized by the projection of optical images on a photosensitive substrate. This allows the formation of transient electrodes on the bottom surface. An AC field was used to precisely sort particles. The implementation of optoelectronic tweezers with microfluidic devices allows single cell sorting with high precision but low throughput (~10 cells/second).

These active techniques are difficult to fabricate and assemble due to the location of the DEP electrodes within the device and electromechanical expertise is required to properly use these devices. In addition, their slow switch time (>20 ms) is a setback for examining intermediate reactions that occur under 20 ms.

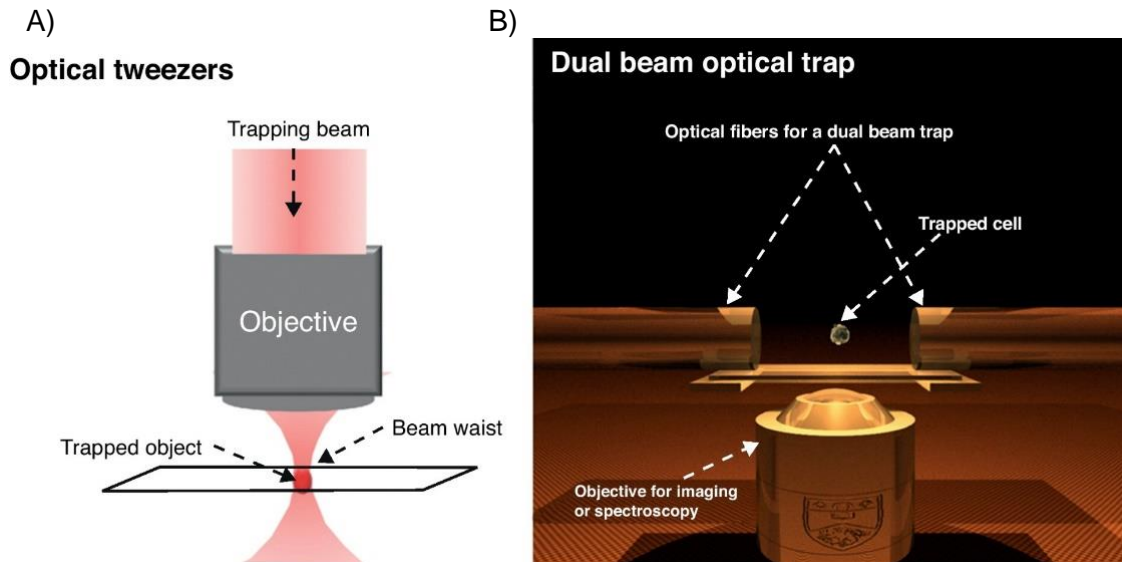


Figure 14. Two different optical trapping geometries. A tightly focused laser beam traps a particle (A). Optical fibres were used to trap a cell at the centre of the counter propagating dual beams (B). An objective lens was used to extract images or perform further analysis such as Raman spectroscopy. From Quidant *et al.*, 2011.⁶³

In addition, magnetic forces had been used for cell manipulation.⁶⁶ The fabrication of microfluidic devices using magnetic forces is easier compared to the DEP devices (electrodes required to be implemented within the device) due to the external location of the magnetic actuators. Magnetic manipulation can be used either with magnetic objects or magnetic labelled objects when they are located within a magnetic field. Wong and colleagues in 2016 used magnetofluidics in order to isolate magnetically tagged cancer cells (HeLa cells, Figure 15).⁸ They were capable of isolating the magnetically tagged HeLa cells with an efficiency of 79%. Magnetic forces were also used by Sasso and colleagues in 2012 to transport magnetic beads into biotin-FITC (fluorescent label) and then transport them onto a wash stream. At the end of the wash stream, the beads were detected by a fluorescence detection system. This type of system can be used to perform immunoassays.⁶⁷

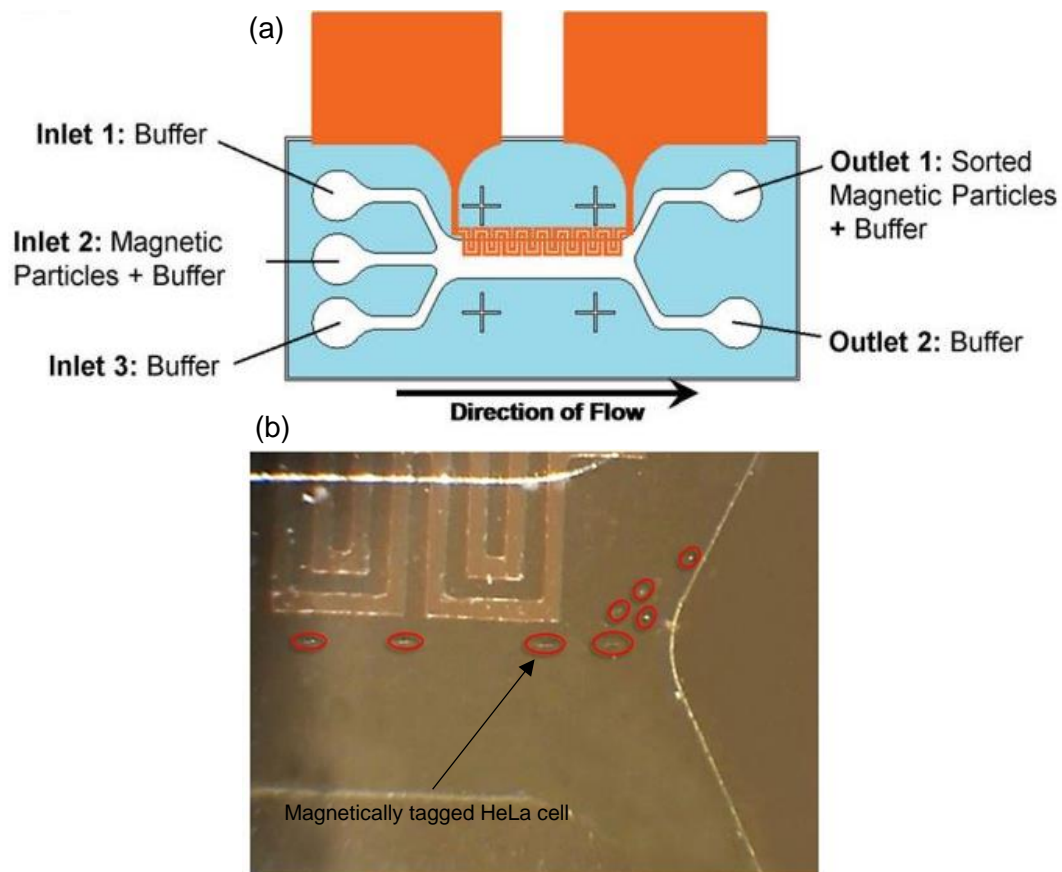


Figure 15. Microfluidic device (a) used to sort magnetically tagged HeLa cells (b). From Wong *et al.*, 2016.⁸

Acoustic waves had been used to manipulate cells or particles. The forces generated by the acoustic waves are between 100-400 pN and they can transport the cells or particles closer or away from the acoustic source. Lenshof and colleagues in 2012 were able to transport particles into different buffers using standing surface acoustic waves (SSAW) transducers.⁶⁸ It should be mentioned that the average flow rate (Q) of this system was 80 $\mu\text{L}/\text{min}$. In addition, a high throughput imaging cytometer was developed by Glynne-Jones and colleagues in 2015 using ultrasonic focusing principles and achieving imaging in flow of up to 104 mm/s and processing 208,000 beads per second.¹⁰ ATDCS (pre-chondrocytic) cell line and primary leukaemia cells were also imaged with a throughput of 52,350 and 60,400 cells per second.¹⁰ This method can be used to detect and identify circulating tumour cells (CTCs) in blood samples with high throughput and precision (Figure 16).

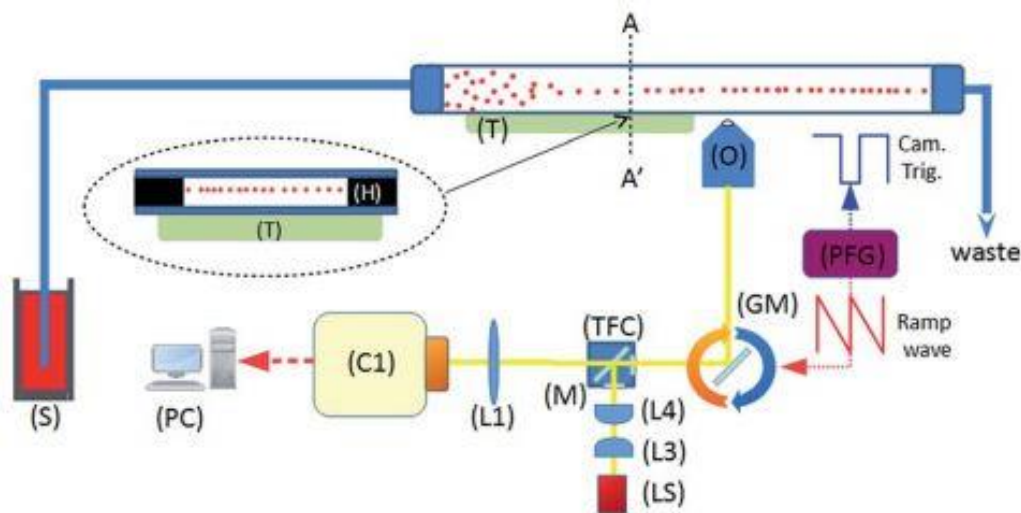


Figure 16. A piezoelectric transducer (T) is used to induce an ultrasonic standing wave in a rectangular channel. Particles are transported using a syringe pump and they are acoustically focused. In this system there is an imaging objective (O), a tube lens (L1), white light source (LS), illumination optics (L3, L4). The angle of the rotating galvo mirror (GM) is controlled by the programmable function generator (PFG). The camera (C1) is also triggered by the PFG. From Glynne-Jones *et al.*, 2015.¹⁰

In summary, active methods can be used to deflect cells into a ligand stream and then into a quench buffer stream. However, this will require careful selection of material and fabrication methods in order to reduce the limitations due to the particle-medium refraction index contrast and the acoustic contrast factor. The use of micro- to nanoscopic scale magnetic beads for cell manipulation might block the interaction of the ligand and the receptors and interfere with the receptor signal transduction. The forces on a cell can only be in the order of pN which translates into switching times of 10's of milliseconds which are insufficient for investigating the intermediates of receptor activation dynamics. Another limitation of the active methods is the dependence of their efficiency factors on the size of the particles (Table 1). This indicates that less force will be applied in smaller cells compared to larger cells thus, the temporal control required for the study of receptor activation dynamics is lost.

Table 1. Comparison of the efficiency factor and switch time between active methods for cell deflection		
	Efficiency Factor	Switch time (τ_{switch})
Dielectrophoresis (DEP)	Object size (r^3), permittivities of liquid and object	80 ms ²⁰
Magnetism	Object size (r^3), effective susceptibility of object relative to the liquid	150 ms ⁶⁷
Acoustics	Object size (r^3), density and corresponding compressibility of the liquid and object	25 ms ⁶⁴
Optical tweezers	Object size (r^3), shape, material and position of the object with respect to the spatial profile of the beam	30 ms ⁶⁹

1.4.2 Passive methods

Deterministic lateral displacement (DLD) is a passive technique that uses the principle of stream thinning by an angled array of pillars (Figure 17). The pillar size, gap and angle are finely tuned to discriminate different-sized particles based on their trajectory. If the particles exceed the critical size, they are bumping on the pillars and they get displaced. This is called bump or displacement mode. Cells with a radius smaller than the laminar stream are transported within are not displaced but they follow their original path. This mode is called streamline mode. DLD had been used for separating cancer cells, blood cells and bacteria based on their size.^{70 71 72} Morton and colleagues in 2008 successfully used this technique to wash, label and

lyse cells. Platelets were processed through the DLD microfluidic system and they were displaced into a labelling buffer stream (PE-anti-CD41) and subsequently into a washing buffer stream.⁷³ In addition, *Escherichia coli* cells were displaced into a lysis buffer stream (8% SDS) allowing collection of the cell nucleus.⁷⁴ The use of DLD can switch cells depending on the velocity. However, there are a few limitations using this technique. The high risk of clogging can cause the cells to use alternative routes with associated changes in the times of ligand and quench buffer interactions and thus varied incubation times, therefore incubation time control is lost. In addition, while high velocity can be used to increase switch speed, the magnitude of cell deformation increases, such that the effective size of the cells is decreased and they are no longer displaced.

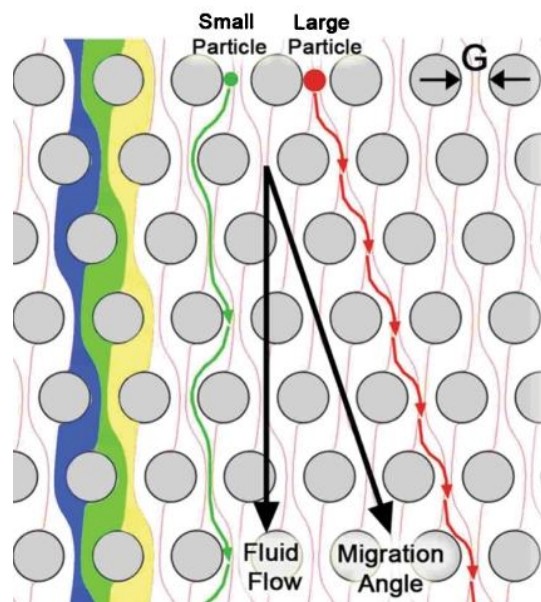


Figure 17. Deterministic lateral displacement of small and large particles in streamline and displacement modes, respectively. From Gossett *et al.*, 2010.¹²

Yamada and colleagues in 2004 developed a cell deflection method which is similar to DLD and it is called pinched flow fractionation (Figure 18).⁷⁵ In this system, the particles are transported to a flow stream that shrinks because of the channel confinement. This causes the cell to touch the wall. When it touches the wall, the cell centre point gets displaced by a few micrometres based on how thin the stream is.

The cell is then displaced further into a wider expansion channel. The deflection position can be found by the following equation:

Equation 1.
$$y = (W_p - r_{particle}) * \frac{W_B}{W_p}$$
 Yamada *et al.*, 2004

$r_{particle}$ is the radius of the particle, W_p the width of the pinched segment, W_B is the width of the expansion channel.

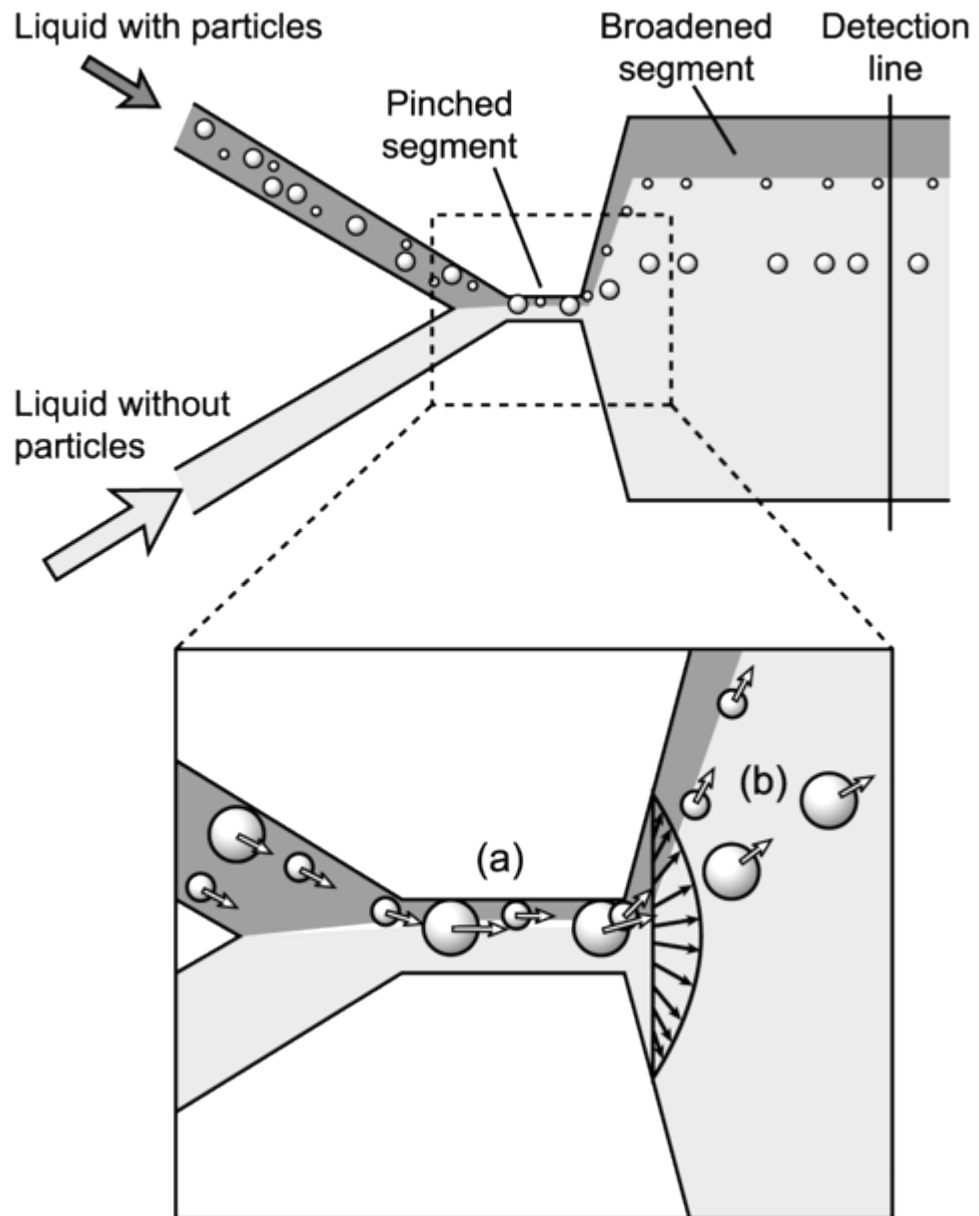


Figure 18. Pinched flow fractionation (PFF) principles in a microfluidic system. Various size particles are focused to the same area of the pinched segment channel (a) the particles are then displaced by the flow based on their size (b) From Yamada *et al.*, 2004.⁷³

A microfluidic method called whole cell quenched flow analysis was developed to examine cell surface processes which are mediated by a ligand/receptor interaction (e.g. EGF/EGFR and IGF-1/IGF-1R) with extreme temporal resolution (milliseconds). This method was an extension of PFF but for the first time microfluidics has been used to control incubation times and not for size-based sorting. This device consisted of two stream thinning elements (STE) and an incubation channel, the length of which and the velocity defines the incubation time (Figure 19).¹⁴ Subsequently, the receptor activation intermediates were preserved by the addition of a quench buffer for further analysis, in this case by laser confocal microscopy.

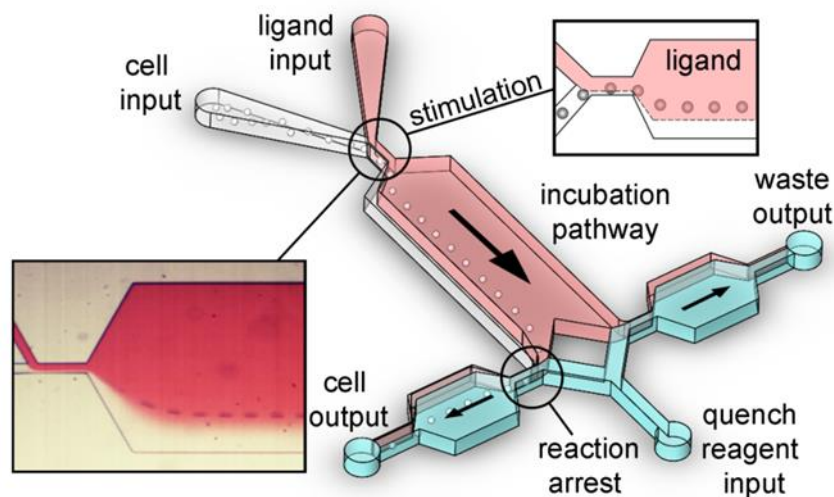


Figure 19. Whole cell quenched flow analysis. Cells were stimulated by the ligand when the cells were deflected into the ligand stream (red dye) and the reaction was arrested after the arrival at the reaction arrest zone by their deflection into a quenched buffer. From Chiang *et al.*, 2013.¹⁴

The switch times obtained using this technique were 2.2 ms in the first stream thinning element with a mean velocity $\sim 100 \text{ mm s}^{-1}$. The switch time for the cells to be displaced into the quench buffer was 550 μs (Figure 20). This allowed to stimulate and preserve the reaction intermediates that occur in short millisecond timescales.¹³

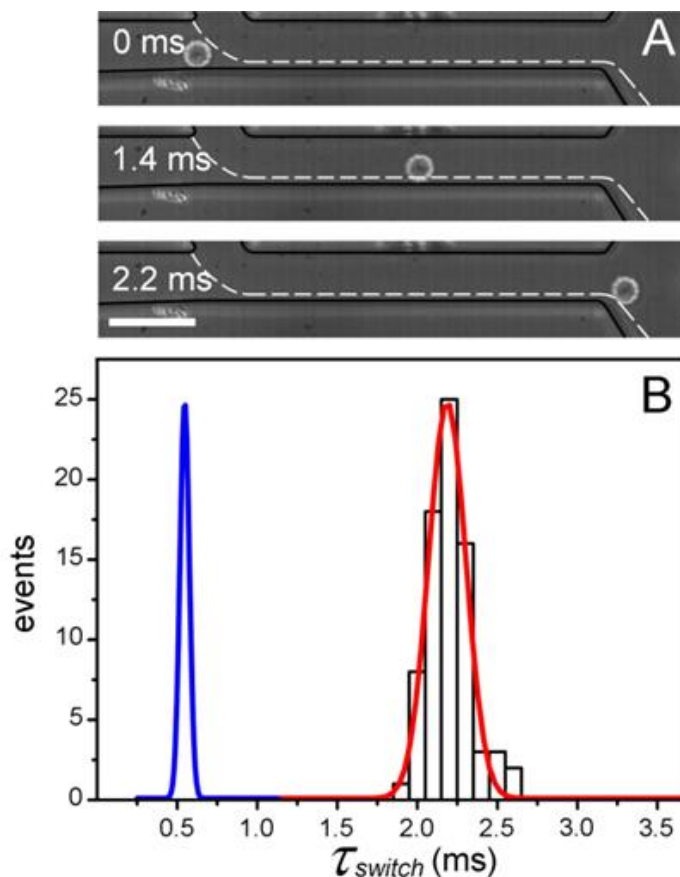


Figure 20. HeLa S3 cells were switched into the ligand stream in 2.2 ms (A), the switch time of the cell into the quench buffer was 550 μ s (B). From Chiang and West, 2013.¹³

The contemporary model of EGFR activation considers ligand binding, that enables diffusion-mediated dimerization in the cell membrane for *trans* phosphorylation between the two receptor intracellular domains. The highly temporally resolved pY1173 data generated from the whole cell quenched flow analysis approach suggested that *cis* phosphorylation may precede *trans* phosphorylation and occurs between 100 ms and 250 ms which is followed by a sharp dephosphorylation (500 ms) and then reaching phosphorylation saturation levels (>1s, Figure 21).¹³ The development and use of the whole cell quench flow technique was promising and successful for the study of the biological reactions that occur in such low temporal resolution. However, this technique was time consuming due the use of multilayer fabrication in order to ensure vertical focusing of cells under the mid-height of the channel allowing velocity coefficient of variation (3.6% with multilayer, 12.8% without multilayer fabrication) and low throughput (e.g. 1 time point per hour due to the high dilution factor 1/64).¹⁴

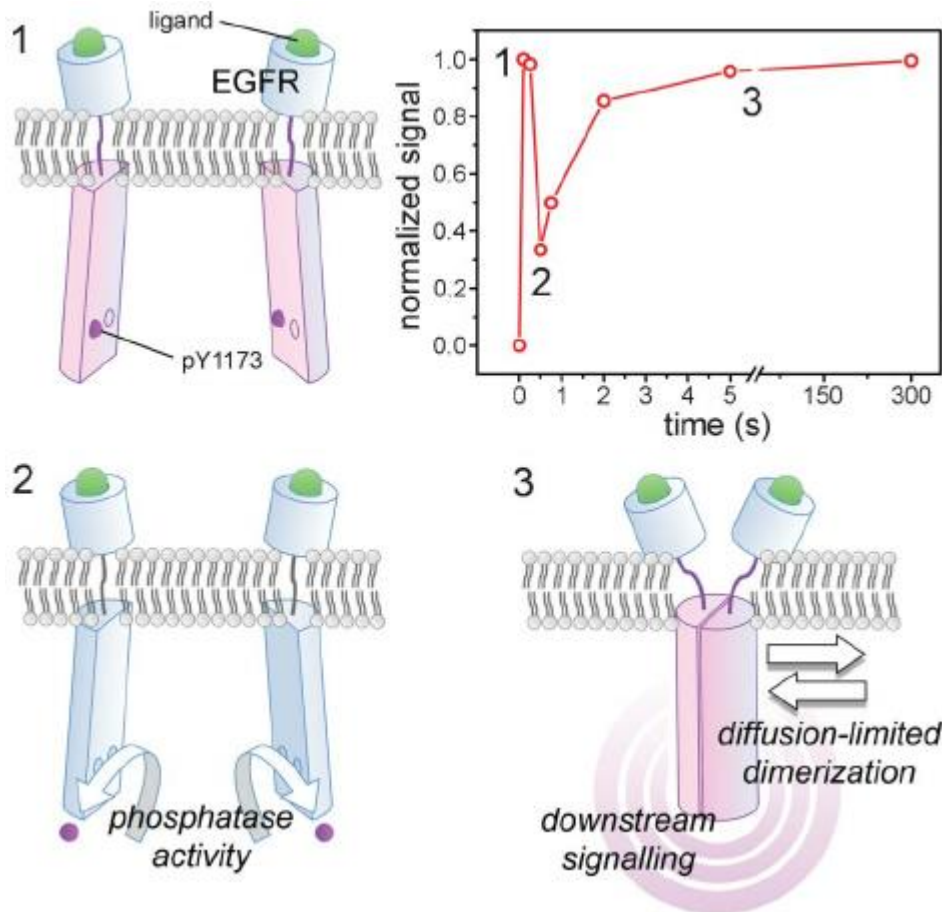


Figure 21. Proposed model of *cis*-phosphorylation based on the recorded data. EGF binds to the ligand binding site on the EGFR leading to phosphorylation of the Y1173 residue (1). Subsequently, it is followed by a rapid dephosphorylation due to phosphatase activity (2) and then a diffusion-limited dimerization and *trans*-phosphorylation of Y1173 (3). Unexpected sub-second biphasic EGFR activation was revealed by whole cell quenched flow analysis. From Chiang and West 2013.¹³

1.4.3 Inertial microfluidics

In the last two decades, Inertial microfluidics attracted the interest of scientists due to the high throughput, high precision of cell manipulation, low cost and simple structure that characterizes this technology. Inertial microfluidics operate in an intermediate range ($1 < Re < 100$) between Stokes regime and turbulent regime ($Re \sim 2000$) where inertia and viscosity of the fluid is finite compared to other microfluidic techniques where fluid inertia is negligible (Stokes flow regime, $Re \rightarrow 0$). The inertia and viscosity of the fluid give rise to inertial effects such as: (i) inertial focusing and (ii) secondary flow (Dean flow). Inertial focusing is a phenomenon that rises when randomly distributed particles at the entrance of a straight microfluidic channel are

focused to equilibrium positions due to the effect of two opposite forces. These two forces (i) lift force F_L shear gradient (interaction of the fluid velocity parabola on the particle), moving them towards the walls and away from the microchannel center and (ii) the wall lift force F_L is developed due to the interaction of the particle with the microchannel walls and transporting the particles towards the center of the channel. The balance of these two opposite forces cause the particles to move to equilibrium positions within the channel (Figure 22). So far, inertial focusing has been used to enrich cells based on size as the force and focusing length is dependent on the size of the cells and for continuous cell staining.^{76 77 78} The lift force, F_L , can be found:

Equation 2.

$$F_L = \frac{f_L \rho U^2 a^3}{w} \text{ Di Carlo, 2009.}^9$$

(F_L : lift force, f_L : ~ 0.02–0.05 for channel aspect ratios (height/width), U : maximum channel velocity, ρ : fluid density (kg/m³), a : particle diameter, w : width of channel)

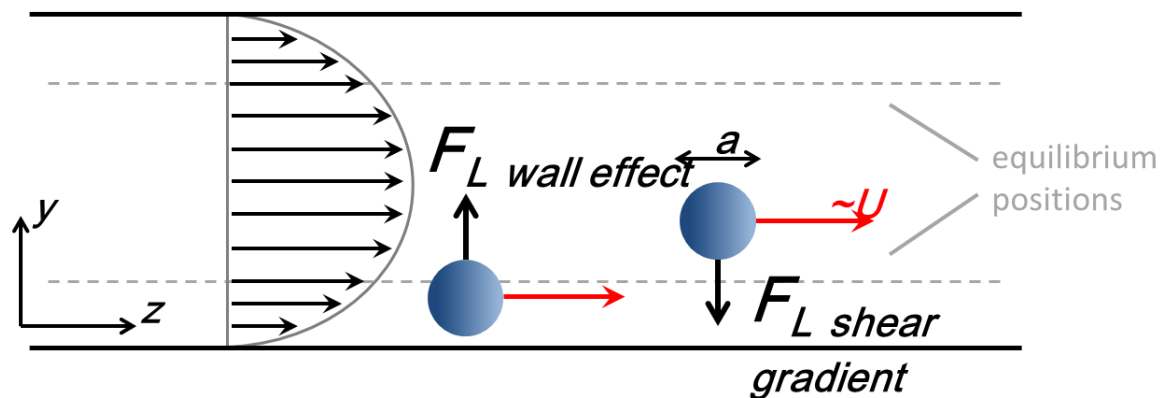


Figure 22. The wall effect force and the shear gradient force that influence the focusing of particles to two equilibrium positions within the microfluidic channel. From Di Carlo, 2009.⁹

Reynolds number (Re) and particle Reynolds number (R_p)

The channel Reynolds number (Re) and the particle Reynolds number (R_p) are dimensionless numbers used to describe the flow of fluid and the flow of particles within a microfluidic channel, respectively. The inertial microfluidic system operates with moderate Reynolds numbers 1-100 (Figure 23). The Reynolds number is

influenced by the mean velocity of the fluid, the density and viscosity of the fluid and the hydraulic diameter of the channel. In theory, the particle Reynolds number should be ≥ 1 and no more than 5 (5-fold dynamic range to avoid 4 equilibrium positions within the inertial focusing channel, Figure 24). When $Re \geq 8$ a further 2 equilibrium positions emerge at the top and bottom of the channel centre-line.

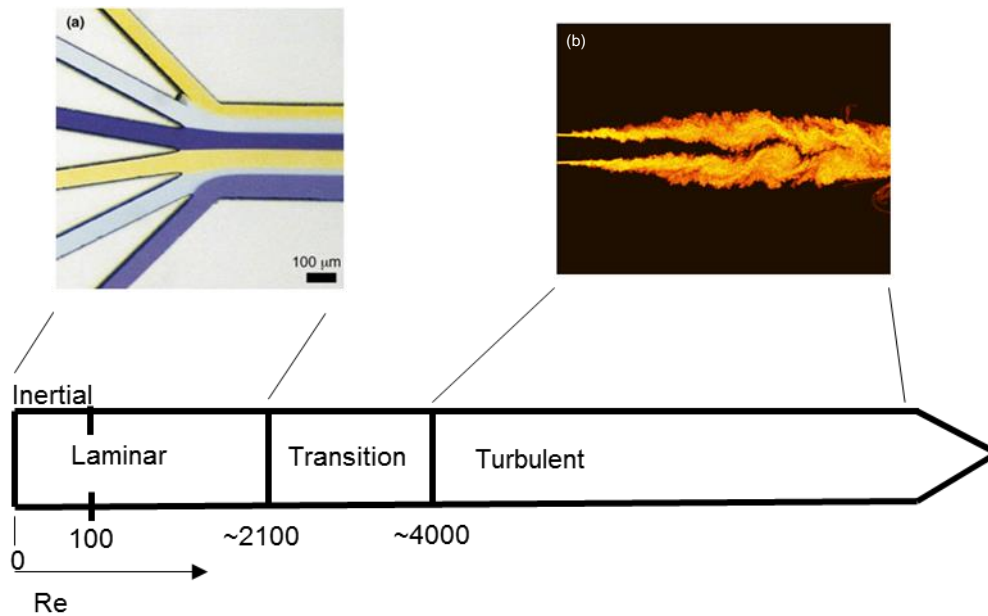


Figure 23. Reynolds number is a dimensionless number that describes the flow of the fluid within a channel or a pipe. Reynolds number between 0-2100 the flow of the fluid is characterized as laminar. Between 0-100 is characterized as inertial. Above ~4000 the flow is turbulent. The transition between laminar to turbulent is between ~2100 - ~4000.

Microfluidic behaviour is strongly linked with the channel dimensions, which is described by the hydraulic diameter:

$$\text{Equation 3. } Dh = \frac{2wh}{w+h} \quad \text{Di Carlo, 2009.}^9$$

(Dh : hydraulic diameter of the channel (μm), w : width of the channel, h : height of the channel).

The Reynolds number describes the relative inertial and viscous components of the flow and is defined as follows:

$$\text{Equation 4. } Re = \frac{\rho U D h}{\eta} \quad \text{Di Carlo, 2009.}^9$$

(Re : Reynolds number, ρ : density of the fluid (kg/m^3), U : mean velocity of the fluid (m/s), Dh : hydraulic diameter of the channel (μm), η : dynamic viscosity of the fluid).

The particles Reynolds number describes the relative dimensions of a particle within a microchannel in the context of the Reynolds of the underlying flow. It is important as it describes whether a flow is laminar or turbulent.

$$\text{Equation 5.} \quad Rp = Re \left(\frac{a}{Dh^2} \right) \quad \text{Di Carlo, 2009.}^9$$

(Rp : particle Reynolds number, a : particle diameter, Dh : hydraulic diameter of the channel (m).

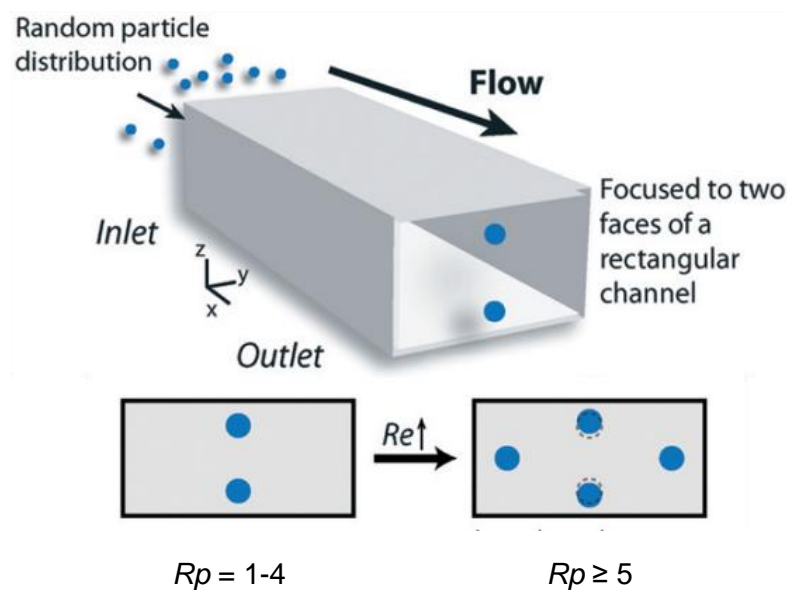


Figure 24. Randomly distributed particles are focused to two equilibrium positions at the end of a rectangular microfluidic channel. An increase in the Reynolds number leads to the development of four equilibrium positions in the microfluidic channel. From Di Carlo,

Dean forces act and affect particles to reach equilibrium positions when they are transported within curved channel geometries.^{9 12} Dean forces occur in curved channel geometries due to a flow momentum mismatch in the centre and the area near the wall of the curved channel. The fluid has a higher velocity at the channel centreline, moves outwards and causes the fluid closer to the channel walls to move inwards. These changes give rise to the formation of two counter rotating vortices called Dean vortex. The secondary forces allow the particles to reach equilibrium positions more quickly. The magnitude of these secondary flows that occur at the bottom and top halves of the channel due to two counter rotating vortices (Figure 25) can be interpreted from the Dean number ¹²:

Equation 6. $De = Re \sqrt{Dh/R}$ Di Carlo, 2009.⁹

(R is the radius of the curvature of the channel, D_h is $(2wh)/(w+h)$, in which w and h are the width and height of the channel, respectively.)

It should be mentioned that a smaller radius of the curvature of the channel leads to a larger Dean number and subsequently larger Dean force. Therefore, the particles reach equilibrium positions faster.

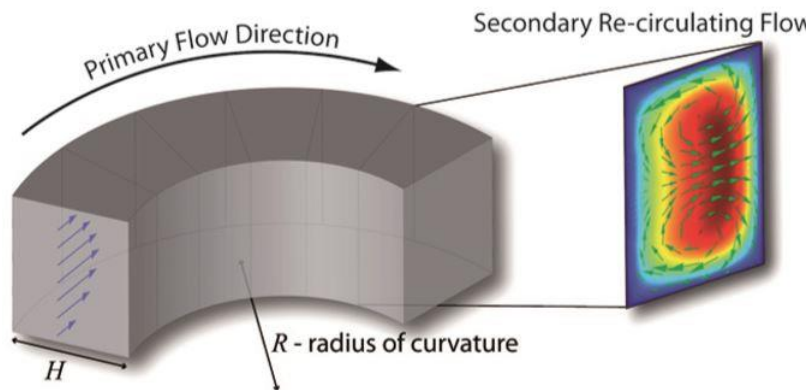


Figure 25. Dean flow occurs in curved channels when faster moving fluid close to the centre of the channel moves outwards and the fluid close to the walls moves inward. This leads to the formation of two-counter rotating vortices at the top and base of the primary flow in the curved channel. From Di Carlo, 2009.⁹

1.5 Aims

This project aims to: (i) develop a microfluidic device for rapid ligand and quench buffer interactions for ultrafast stimulation of cells with ligands and immediate quench of the reaction, (ii) assess different techniques such as Western blot analysis and Flow cytometry to monitor EGFR signalling and (iii) investigate EGFR signalling using the developed microfluidic device for sub-second timescales.

2. Materials and Methods

2.1 Concept and Design

As seen in figure 28, different microfluidic elements were implemented together in order to accomplish ultrafast stimulation of cells and precise incubation of cells. The design for the inertial microfluidic systems was performed using the Draftsight-Dassault Systemes software.

2.1.1 Inertial Microfluidics

General considerations and simplified rules were followed in order to design an effective inertial microfluidic device.⁷⁶ One of the factors kept in consideration were the forces that act on the particle within the microchannel (F_L shear gradient and the F_L wall effect, Figure 22). F_L wall effect directs the particle away from the wall and the F_L shear gradient directs the particle away from the centre of the channel. The F_L shear gradient is developed due to the parabolic velocity profile formed within the microfluidic channel. In addition, the channel width should be 5-7 times larger than the particle diameter (α , or $\alpha/w \geq 0.2$) in order to achieve precise focusing of particles to two equilibrium positions in a rectangular channel ($h > w$) to affect lateral displacement into two equilibria positions.

2.1.2 Dean Flow

The design of the incubation channel element was based on the use of the Dean force coupled inertial flow principles in order to achieve uniform incubation times by focusing the cells to a common position and therefore, a common velocity.

2.1.3 Hydraulic Resistance

The balance of the hydraulic resistance is important in order to be able to remove 50% of the volume that contains any untreated cells (with ligand or quench) hence, reducing the background noise in the offline analysis data.

The hydraulic resistance is an equivalence of electrical resistance and can be calculated using an equivalent model to Ohms' law ($I = \frac{V}{R}$, $R_H = \frac{8\mu L}{\pi r_H^4}$).

A law stating that the electric current (I) is proportional to the voltage (V) and inversely proportional to the resistance (R). Using the equation 7 and 8, the hydrodynamic resistance and thus the length of each microfluidic element of our circuit was calculated in order to balance the hydraulic resistance of the circuit. The circuit was designed to remove cells that are not treated with ligand and quench buffers. This can be achieved using balanced resistors, such that the flow bifurcates: After the first inertial focusing stage into the ligand stream, a 50% volume is delivered downstream and the remaining 50% (with any untreated cells) is ejected from the first outlet. Following the addition of the quench buffer, the flow again bifurcates, delivering 50% of the volume to the cell outlet and the remaining 50% to the waste outlet (with any untreated cells). With a 1:1 cell:ligand ratio, followed by a 1:1 cell:quench ratio, the circuit can be operated using parallel syringes in a single syringe pump. The models, shown in Figure 26 A, were used to identify the correct model for interpreting the pressure and resistance distributions and thus design the correct hydraulic resistance lengths to ensure flow bifurcation for the two waste outlets.

$$\text{Equation 7. } R_H = \frac{8\mu L}{\pi r_H^4} \quad \text{Oh KW et. al., 2011.}^{89}$$

R_H : hydraulic resistance (N.s/m⁴), μ : viscosity of the fluid, L : length of the channel, π : 3.14159, r_H : rectangular cross section channel.

$$\text{Equation 8. } r_H = (wh)/(w + h) \quad \text{Oh KW et. al., 2011.}^{89}$$

r_H : rectangular cross section channel, w : width of the channel (μm), h : height of the channel (μm).

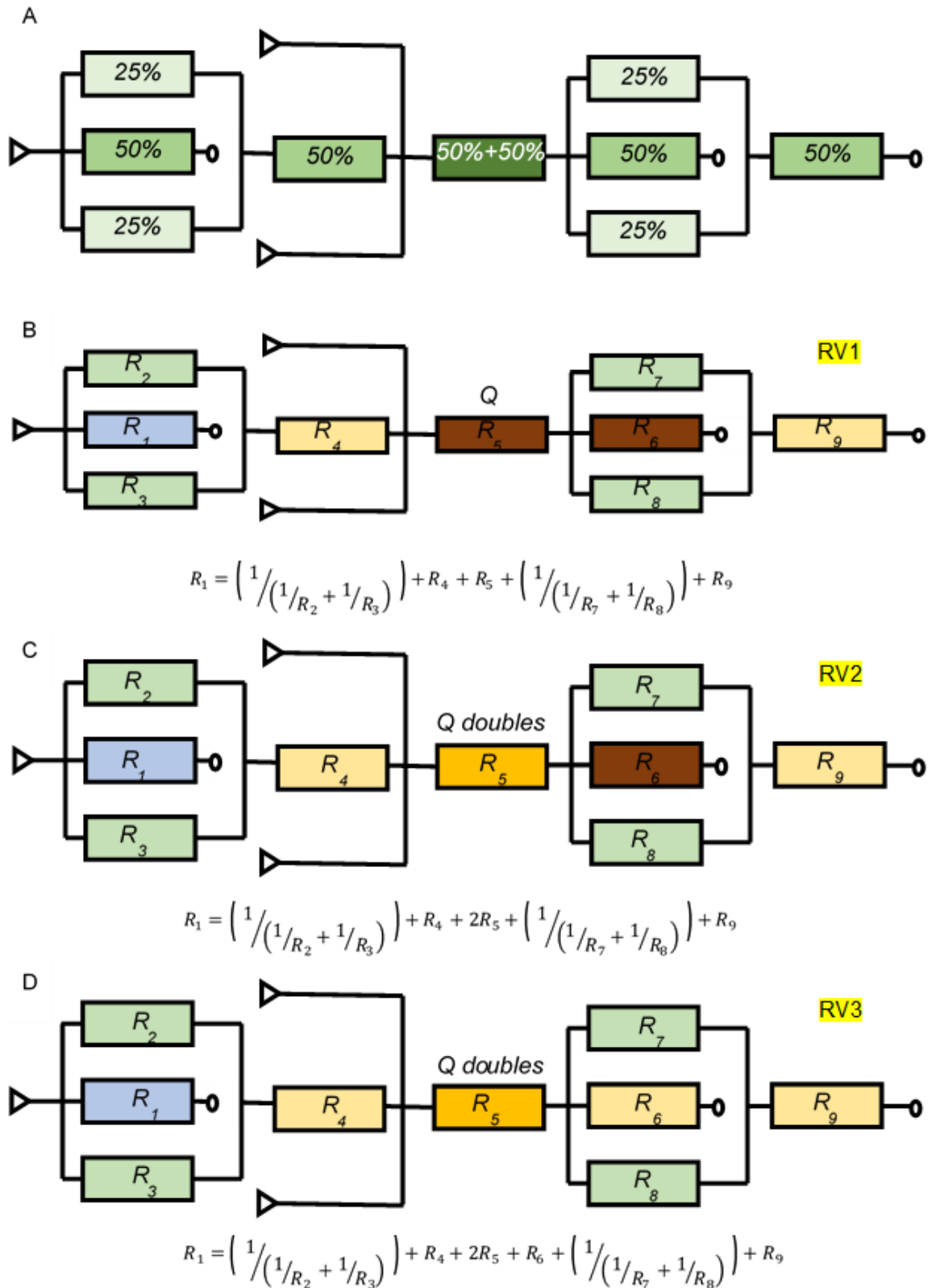


Figure 26. Flow rate volumetric distribution requirements for the new design of the microfluidic circuit (A), RV1 microfluidic circuit was design without considering that the flow rate doubles on the resistor (R5) and the R6 (B) in the design of the RV2 microfluidic circuit we considered that the flow rate doubles but not the R6 (C) for the RV3 design we considered that the flow rate doubles on the resistor (R5) and the R6 (D).

2.2 Dimensions of time machines versions 1.0, 1.5 and 2.0

According to the inertial and Dean focusing principles mentioned in section 2.1, inertial focusing occurs when the channel dimensions are no larger than 5-7 times the particle diameter ($15\ \mu\text{m}$) or $\alpha/w \geq 0.2$ (α : particle diameter, w : channel width) to achieve precise focusing to two equilibrium positions in a rectangular channel ($h > w$). Therefore, the inertial focusing channel element of the circuit was designed to have the following dimensions: height of $100\ \mu\text{m}$ and width $50\ \mu\text{m}$ producing an aspect ratio of 2, but with various lengths (2 mm, 4 mm, 6 mm and 8 mm) in order to find the shortest length required for precise cell focusing into the ligand streams (Figure 27). However, in the practice of microfabrication, the SU-8 layer and thus the microfluidic structures were $85\ \mu\text{m}$.

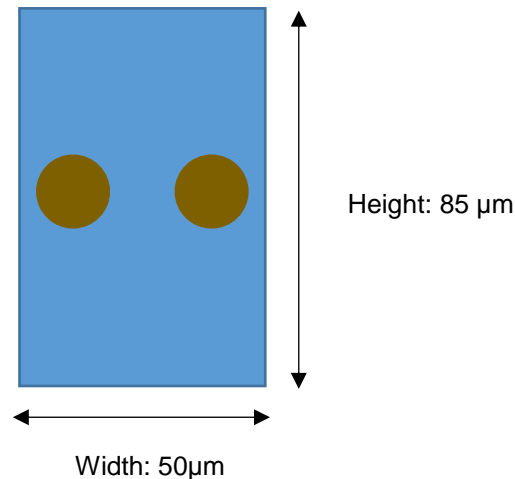
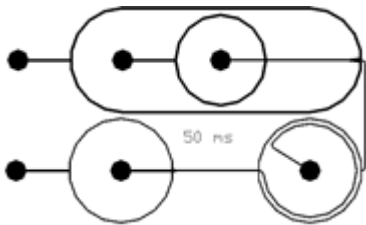


Figure 27. $15\ \mu\text{m}$ polystyrene particles are focused to two equilibrium positions in an inertial microfluidic channel of $50\ \mu\text{m}$ width and $85\ \mu\text{m}$ height.

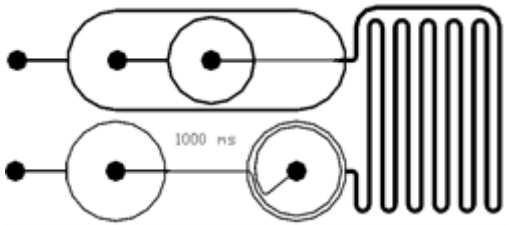
The incubation channel was designed to have an aspect ratio of 1:3 ($h:w$): The channel had the following dimensions $250\ \mu\text{m}$ width and $85\ \mu\text{m}$ height. The length of the incubation channel defines the time of cell incubation within the ligand.

The dimensions of each microfluidic element in a complete microfluidic circuit can be found in Table 2.

Inertial focusing channel (Height)	85 μm
Inertial focusing channel (Width)	50 μm
Focusing length	1,2,4,6,8 mm
Incubation channel (Height)	85 μm
Incubation channel (Width)	250 μm
Incubation channel length (50 ms incubation)	10 mm
Incubation channel length (1000 ms incubation)	200 mm

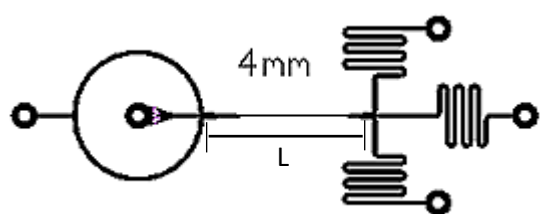


Microfluidic circuit Version 1.0
(50 ms incubation)



Microfluidic circuit Version 1.0
(1000 ms incubation)

Inertial focusing channel (Height)	50 μm
Inertial focusing channel (Width)	25 μm
Focusing length (L)	1, 2, 3,4, 5 mm



Microfluidic circuit version 1.5 was consisted of an inertial microfluidic element only.

Table 4. Dimensions of the next generation microfluidic circuit version 2.0

Inertial focusing channel (Height)	65 μm
Inertial focusing channel (Width)	30 μm
Focusing length	1, 2, 3, 5 mm
Incubation channel (Height)	65 μm
Incubation channel (Width)	65, 120, 300 μm
Incubation channel length (25 ms incubation)	17.6 mm
Incubation channel length (50 ms incubation)	28.1 mm
Incubation channel length (1000 ms incubation)	34.9 mm
RV1, RV2 and RV3 differ only at the ring length -12.50, 20.78, 23.60 mm (red arrow)	

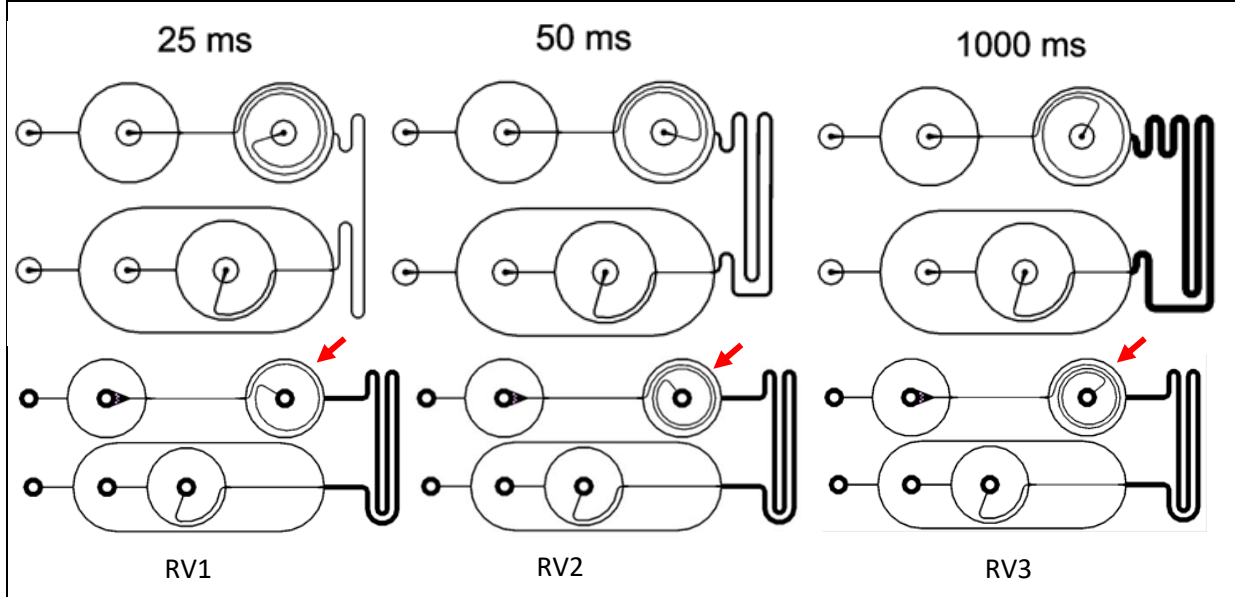
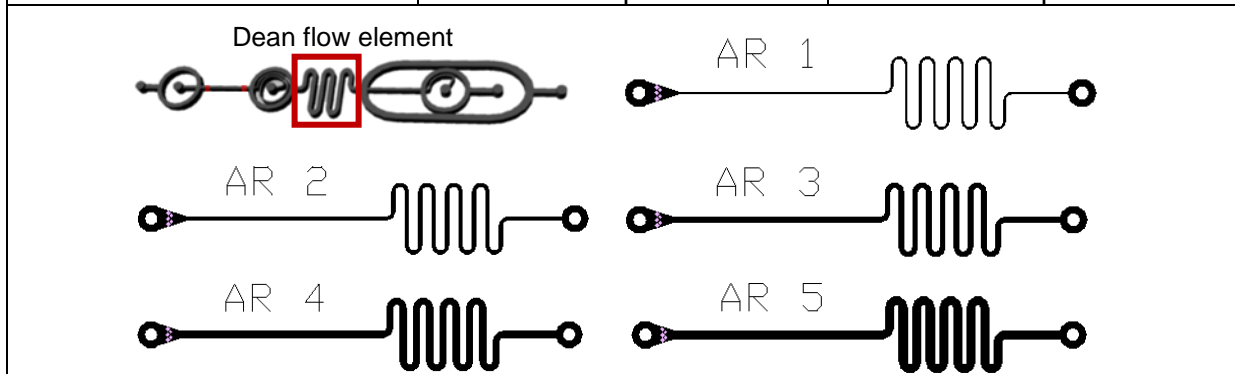


Table 5. Dimensions of the microfluidic devices to study the effects of Dean flow

Device name	Height	Width
Dean flow element	85 μm	260 μm
AR 1	65 μm	60 μm
AR 2	65 μm	120 μm
AR 3	65 μm	180 μm
AR 4	65 μm	240 μm
AR 5	65 μm	300 μm



The microfluidic circuit was designed for the creation of lateral laminar flow and without mixing, to achieve rapid cell stimulation and quench of the reaction based on the lateral displacement of cells using inertial microfluidics (Figure 28). An optimal high-speed microfluidic system characterized by high throughput with rapid stimulation of EGFR, followed by an incubation channel for uniform and reproducible incubation times and immediate quench to preserve the dynamic events of EGFR activation is required. Various active and passive cell manipulation techniques have been described in Chapter 1. However, active cell manipulation methods that use force fields (e.g. electric and acoustic fields) for transporting cells lead to long switch times (> 20 millisecond) and cause cell death due to the localised heating on the cells.⁷⁹ Thus, such techniques are inefficient to resolve the EGFR activation dynamics that occur in millisecond-scale timescales.

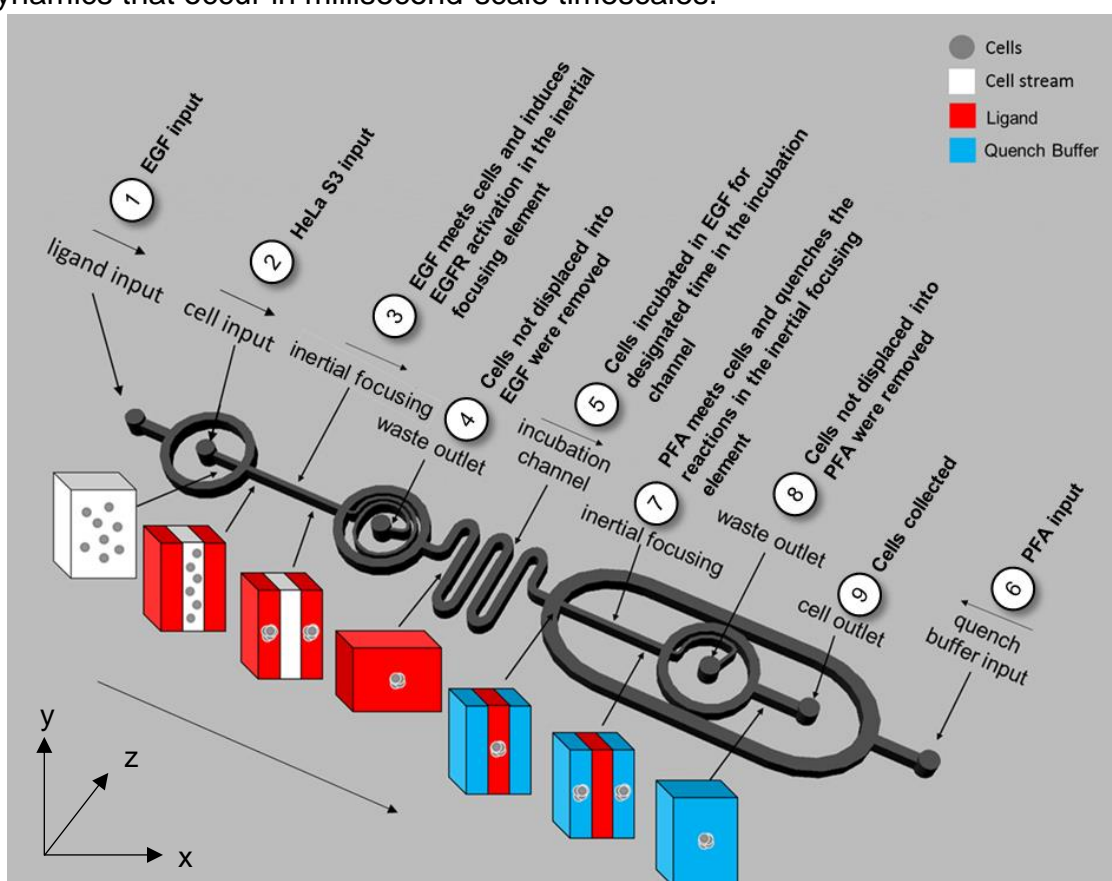


Figure 28. Inertial focusing microfluidic design and concept. EGF and cells will be injected into the device. With hydrodynamic focusing to produce a cell stream flanked by streams of ligand. The cells will be inertially focused, submerged into the EGF and stimulated. Non-focused cells will be removed *via* the first waste outlet. The stimulated cells will flow through the incubation channel. Quench buffer will be added in order to arrest the reaction. The stimulated cells will undergo inertial focusing and be submerged into the quench buffer. Non-focused cells will be removed *via* the second waste outlet.

2.3 Microfluidic device manufacturing

2.3.1 PDMS microfluidic device replication

The microfluidic devices were prepared by replica moulding in poly(dimethylsiloxane) (PDMS, Sylgard 184, Dow Corning). The replica mould was fabricated by Microsystems, GmbH (Germany) using the negative photoresist SU-8 (100), with spin coating to a depth of 85 μm and standard UV photolithography using a chrome-glass mask (JDPhotoTools, UK). The PDMS pre-polymer and platinum curing agent were mixed at a ratio of 10:1 (e.g. 30 g pre-polymer to 3 g curing agent) and degassed in a vacuum chamber until complete removal of air bubbles. PDMS was poured onto the SU-8 microstructures and retained using an 8-mm-high thermo-tolerant Delrin™ frame for curing at 80 °C for ~90 min on a hotplate. The elastomeric PDMS device was removed from the SU-8 wafer and the mould and stored in a clean Petri dish.

2.3.2 Polyurethane master moulds

Thick PDMS devices were prepared from the silicon wafer and taped to the bottom of silicone mould using a double-sided tape with the structures facing upwards. An equal volume polyurethane (Smooth-ON, Oomoo 30™) part A and part B were mixed vigorously for 2 min. The polyurethane mixture was pour onto silicone moulds that contained the PDMS devices. Degassing in a vacuum chamber for 15 min was necessary to remove the air bubbles. The silicon moulds were removed from the vacuum chamber and they were placed on the bench to set (overnight). The next day the polyurethane moulds were placed in an oven (Quincy Lab Inc., USA) (60 °C) for 4-6 h for maximal curing. N.B. Mixture A and B leftover in the 50 mL falcon tube should be disposed however tube cap should be loose (exothermic reaction can lead to explosion).

2.3.3 Device packaging

The PDMS device was punched with a 1 mm diameter biopsy punch (Integra™ Miltex™ Standard Biopsy Punches, USA) generating hourglass-shaped through-holes for plug 'n' play interconnection with the tubing. For encapsulating the

microstructures a glass slide was used. The surfaces of the PDMS microfluidic device and the glass slide were first cleaned: Particulates and fibres were removed using 3M Scotch tape. A 30 s oxygen plasma treatment (0.2 mbar, 70 W, 40 kHz Femto, Diener Electronics, Germany) was used to generate silanol groups on the PDMS and glass surfaces for contact bonding (Figure 29). The surfaces were then gently pressed together for 10 s to achieve a pressure-tolerant bond and baked overnight in a 60 °C oven (Quincy Lab Inc., USA).

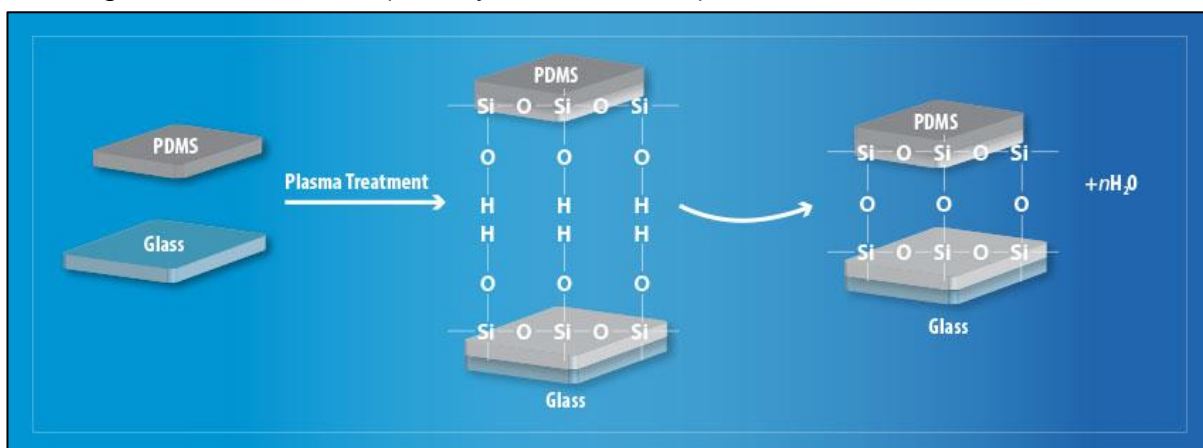


Figure 29. Plasma treatment of the glass and PDMS surfaces allows removal of hydrocarbon groups and exposure of hydrophilic silanol groups (-OH) at the surface of the PDMS layer allowing the formation of strong covalent bonds (Si-O-Si) when brought together with the glass. These covalent bonds form an inseparable seal between the two layers. (From plasmatreatment.co.uk)

2.4 Microfluidic operation

2.4.1 Microfluidic hardware

The microfluidic experimental system is documented in figure 30 A. Syringes (5 mL, Terumo, Japan) and needles (25G 0.5 x 16 mm Agani™ Terumo, Japan) were used to inject the samples (particles or cells) into the PDMS microfluidic system using programmable displacement pumps (Fusion 200, Chemyx Inc, U.S.A.). Fine bore polythene tubing (0.38 mm ID, 1.09 mm OD, Smiths Medical International Ltd) was cut to length, without crushing, using a clean cut tubing (S.C.A.T. Europe, Germany). Forceps (Sigma-Aldrich, UK) were used to safely interface the tubing with the needle and insert the tubing into the inlets and outlets of the PDMS device (Figure 30 B). A high-speed camera (10,000 fps maxima, Phantom, Vision Research, Wayne, New Jersey, U.S.A.) on a custom-built microscope system (see Figure 30 C) was used to image the transport of particles and cells.

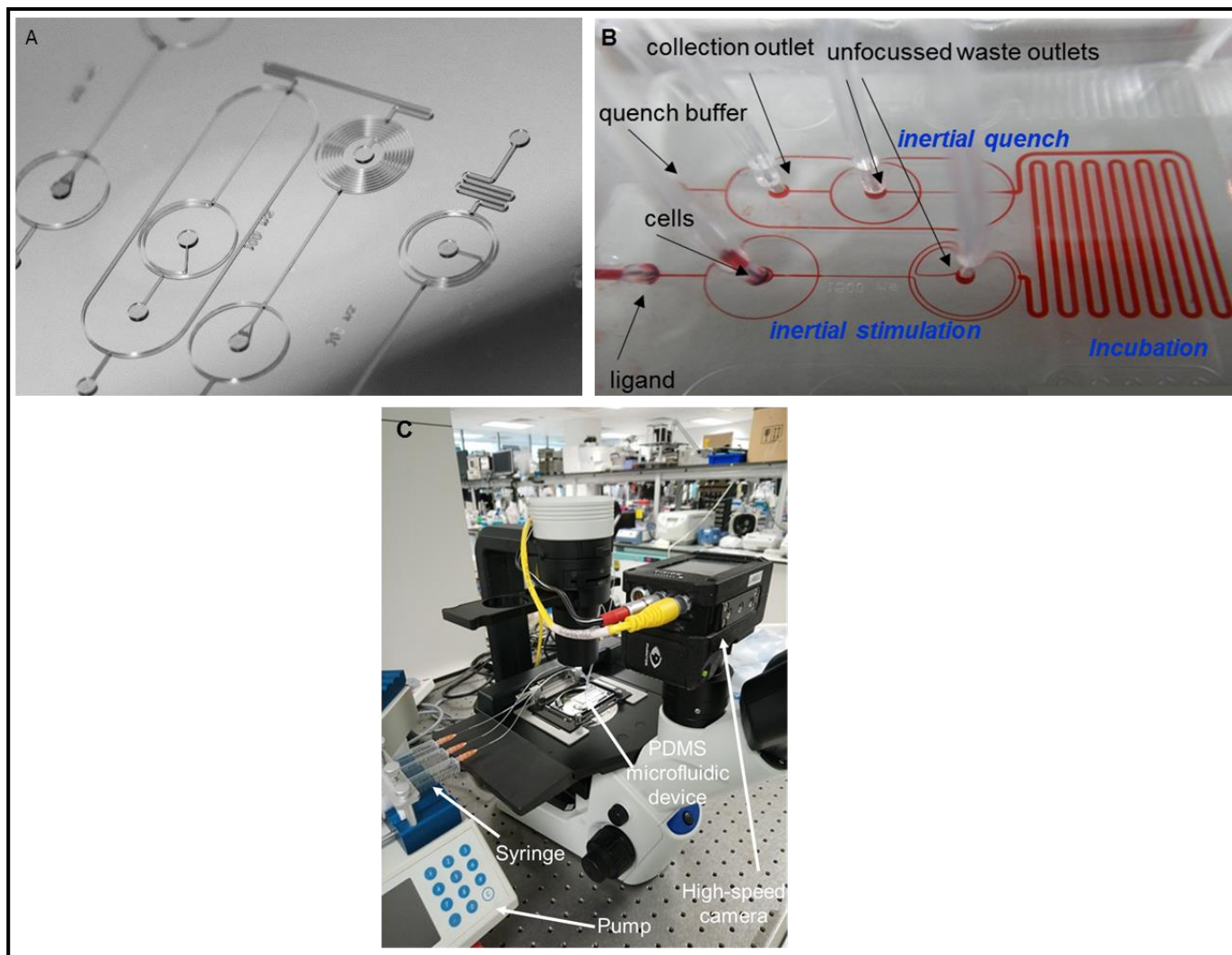


Figure 30. SU-8 wafer with the fluidic circuit structure (A). PDMS microfluidic circuit with its interconnection tubing with visualisation of the microchannels aided with a red dye (B). Microfluidic experimental set up using a high speed camera (up to 10,000 fps) on a custom made rig (C).

2.4.2 Sample preparation (polystyrene particles) and density matching

15 μm -polystyrene particles (Kisker LTD, Germany. 2.5×10^5 particles mL^{-1}) or 15 μm -polystyrene fluorescent particles (Ex/Em 580/605 nm) (Thermo Fisher Scientific, U.S.A.) were suspended in (0.22 μm filtered) 1X Phosphate Buffer Saline (PBS, Fisher Chemicals, UK) containing Tween 20 (0.05%, Sigma-Aldrich, UK) and 30% (v/v) Ficoll-Paque™ Premium (1.073 sterile solution, GE Healthcare, USA) for density matching to avoid sedimentation and the detergent to prevent particle aggregation.

2.4.3 Fluorescence microscopy

The fluorescent particle positions while they were transported in high velocity within the microfluidic circuit were visualised by their fluorescent traces using high exposure (2000 ms) imaging on a fluorescence microscope (Olympus Lifescience IX70 fluorescence microscope). Additional image analysis such as image stacking, measurement of fluorescence intensity was performed using ImageJ. Post processing of videos was performed using the mTrackJ, a plugin of ImageJ to quantify the velocity of each particle.

2.4.4 Quantitative image analysis to identify particle/cell position

The quantification of the videos captured using the high-speed camera (Phantom, Vision Research, Wayne, New Jersey, U.S.A.) for validating the focusing of particles or cells into two equilibrium positions was performed using ImageJ software (version 1.50i, Wayne Rasband, National Institutes of Health, U.S.A.) to convert the video into a stack of images, rotating the image, selecting the area of interest and subsequently obtaining the relative centroid position of particles/cells using the coefficients in Table 6. Table 6 shows how the coefficients were used to calculate the relative centroid position (%).

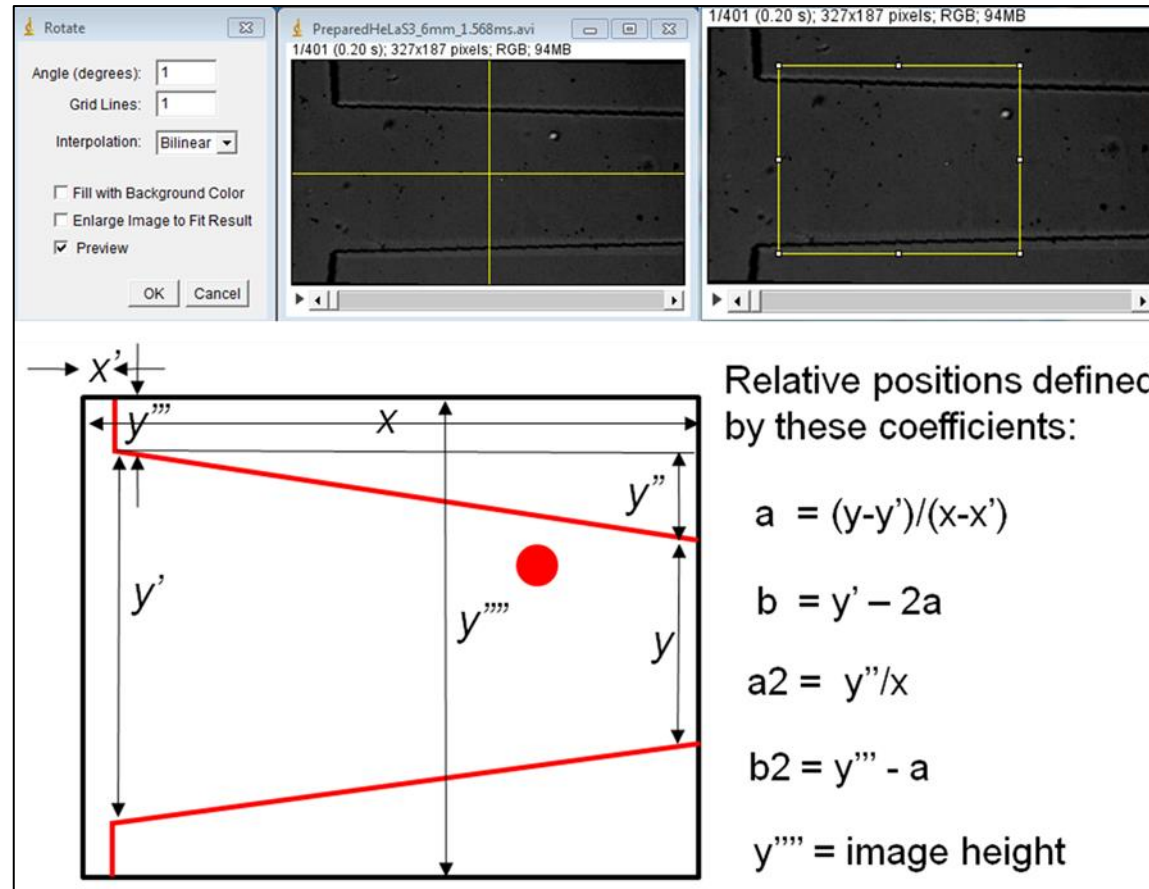


Figure 31. Centroid position of particles/cells was calculated using ImageJ image coordinates and the coefficients. (a: max height over max length of channel area, b: max channel height minus twice ratio (a), a2: The excluded length (far L) over max length, b2: beginning to channel exit over twice the ratio (a).

Table 6. Relative centroid position of HeLa S3 cells within an inertial microfluidic channel. The coefficients (a, b, a2, b2) were essential for further use in the formulas (Position (x) = x*a+b, Height (y) = a2*x+b2) and subsequently the relative centroid position (%).

Coefficients	X	Y	Relative (x) Position(x)=x*a+b	B Height (y)= a2*x+b2	H=y''''-2B Channel width	H/2 ½ channel width	Y-B H into channel	(H/2)-(Y-B) H from center	(%) Position
a= -0.02553	60	51	116.5193	20.48213	108.0357	54.01787	30.51787	23.5	43.50412
b= 118.0511	127	106	114.8088	24.34200	100.3160	50.15800	81.65800	-31.5	-62.80150
a2= 0.05761	80	98	116.0087	21.63433	105.7313	52.86567	76.36567	-23.5	-44.45230
b2= 17.02553	57	75	116.5959	20.30930	108.3814	54.19070	54.69070	-0.5	-0.92267
	169	52	113.7365	26.76162	95.47676	47.73838	25.23838	22.5	47.13189
	167	111	113.7876	26.6464	95.7072	47.8536	84.35360	-36.5	-76.27430
	196	62	113.0472	28.31709	92.36582	46.18291	33.68291	12.5	27.06629
	183	69	113.3791	27.56816	93.86368	46.93184	41.43184	5.5	11.71912
	96	56	115.6002	22.55609	103.8878	51.94391	33.44391	18.5	35.61534
	84	68	115.9066	21.86477	105.2705	52.63523	46.13523	6.5	12.34914
	107	99	115.3194	23.1898	102.6204	51.3102	75.81020	-24.5	-47.74880

2.5 Cell culture

Human epithelial cancer cell line HeLa S3 was used due to expression of epidermal growth factor receptor on the cell membrane and their ability to be cultured in suspension without changes in the normal function of their signalling pathways. HeLa S3 cells were derived from a clone of the HeLa cervical cancer cells and were purchased from ATCC. HeLa S3 cells were cultured in Dulbecco's Modified Eagle Medium (Gibco™, DMEM, high glucose, GlutaMAX™ supplement, U.S.A.) with 10% (v/v) foetal bovine serum (Gibco™, FBS, E.U.-approved, South America origin, U.S.A.) and 1% (v/v) penicillin and streptomycin (Gibco™ Penicillin-Streptomycin (10,000 U/mL, U.S.A.) in a humidified 5% CO₂ incubator. The adherent cells were detached from the flask (75 cm²) by the addition of trypsin (Gibco™, Trypsin-EDTA 0.05%, phenol red, U.S.A.) and harvested at 80% confluency. Trypsin was neutralised by the use of serum containing growth medium. The cell suspension was transferred to a 15 mL falcon tube and centrifuged for 5 min at 1200 rpm, room temperature. The supernatant was discarded and the cell pellet was re-suspended with sterile media. The cell number and viability was detected with the trypan blue exclusion method. For example 50 µL of cells were mixed with 100 µL of trypan blue (Gibco™, Trypan Blue, U.S.A.) and 10 µL were transferred to a haemocytometer for cell counting. The haemocytometer is composed of multiple squares. All the cells were counted (clear and blue) in each large square (1 large square contains 16 small squares) in each corner of the haemocytometer. The blue cells were non-viable and the clear cells were viable. The total number of viable and dead cells was calculated using the following equations.

$$\text{Equation 9. Viable Cell Count (Live cells per millilitre)} = \frac{\text{Number Live Cells Counted}}{\text{Number of large corner Squares counted}} \times \text{Dilution factor (in this example 2)} \times 10,000$$

$$\text{Equation 10. Non-Viable Cell Count (dead cells per millilitre)} = \frac{\text{Number Dead Cells Counted}}{\text{Number of large corner Squares counted}} \times \text{Dilution factor (in this example 2)} \times 10,000$$

$$\text{Equation 11. Percentage Viability} = \frac{\text{Number of Viable Counted}}{\text{Total Number of Cells}} \times 100$$

2.6 Western blot analysis

Western blot analysis was used to quantify the specificity of the antibodies that recognise the total levels of EGFR and phosphorylated tyrosine residues (pY1068 and pY1173) of epidermal growth factor receptor (EGFR). PY20 antibody was also used for detecting phosphotyrosine-containing proteins. Western blotting is used to separate the proteins according to their molecular weight using SDS polyacrylamide gel electrophoresis.

Cells were fractionated by the use of Laemmli sample buffer (0.3125M Tris-HCl pH 6.8, 50% glycerol, 25% 2-mercaptoethanol, 10% SDS, 0.01% bromophenol blue) that contained protease and phosphatase inhibitors (1X Halt™ Protease and Phosphatase inhibitor cocktail, Thermo Scientific™, U.S.A.) in order to prevent protein degradation and dephosphorylation, respectively. This is followed by boiling of the samples at 95 °C for 5 min. The use of the Laemmli sample buffer is essential to reduce the intra- and inter-molecular disulfide bonds (2-mercaptoethanol), denatures the proteins and give an overall negative charge for mobilisation and size separation by mobility retardation principles in a polyacrylamide gel. The samples were loaded into wells in a sodium dodecyl sulphate-polyacrylamide gel electrophoresis (SDS-PAGE, 10% SDS-PAGE (separation gel solution: 30% (w/v) acrylamide, 1.5 M Tris-HCl pH 8.8, dH₂O, 10% (w/v) SDS, 10% APS, TEMED) with a 4% stacking gel (30% (w/v) acrylamide, 0.5 M Tris-HCl pH 6.8, dH₂O, 10% (w/v) SDS, 0.1% APS, TEMED) that is held in the electrophoresis apparatus (Figure 32). The gel concentration (10%) allowed greater resolution of larger / mid-sized proteins based on molecular weight. When voltage is applied along the gel, proteins migrate through it at different speeds dependent on their size. These different rates of advancement (different electrophoretic mobilities) separate into bands within each lane. Protein bands can then be compared to the ladder bands and estimate the protein's molecular weight. The electrophoresis apparatus was filled with 1X running buffer pH 8.3 (25 mM Tris, 190 mM glycine, 0.1% SDS, dH₂O). Electrophoresis proceeds at a constant 100 V up to a 300 mA limit for 90-120 min until the bromophenol blue dye reaches the bottom of the separation gel.

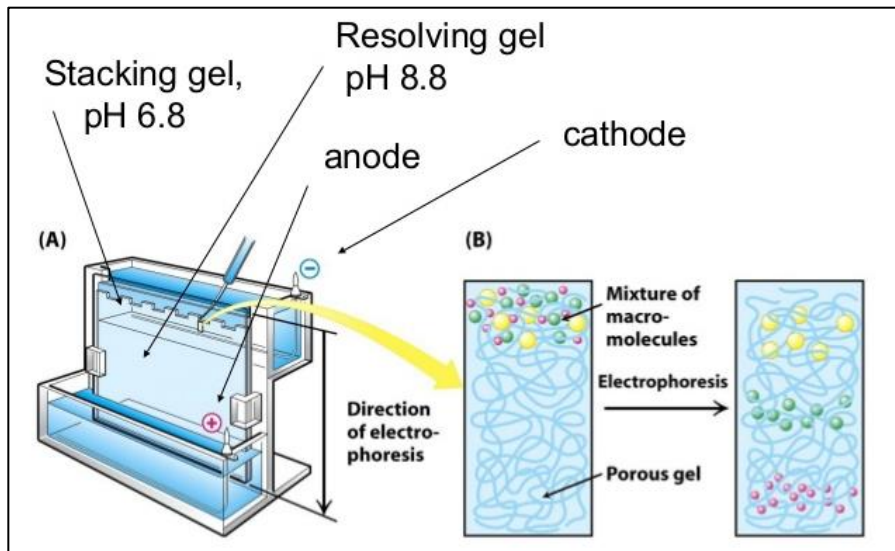


Figure 32. SDS-PAGE gel held in the electrophoresis apparatus where the mixture of macromolecules are separated based on their molecular weight by applying an electric charge. From *Biochemistry, Seventh Edition*, 2012.⁷

The separated proteins on the SDS-PAGE gel were accessible to antibody detection when they were transferred on a membrane made of Hybond P polyvinylidene fluoride (PVDF) membrane (Thermo Fisher Scientific, U.S.A.) which was previously methanol saturated and washed with dH₂O, into a Transblot apparatus (Biorad U.S.A.) that includes a transfer cassette assembly with a sandwich of filter paper layers pre-soaked in 1X transfer buffer (25 mM Tris, 190 mM glycine, 20% methanol, dH₂O, Figure 33). In the transferring method of electroblotting, electric current to pull negatively charged proteins from the gel towards the positively charged anode, and into the PVDF membrane. The proteins are transferred from the gel to the membrane and maintaining their organization.

Air bubbles from the blot sandwich were removed and it was transferred at 90 V for 2 h, to a limit of 350 mA with an internal ice block and a magnetic stirrer placed inside the tank to dissipate the heat. After the transfer, total protein staining (Ponceau S, Sigma-Aldrich U.K.) allowed the total protein that have been transferred to the membrane to be visualized. This allowed to check the uniformity of protein transfer. Blocking of the membrane is a necessary step in order to prevent the interactions between the membrane and the antibody used for the detection of the target protein and prevent non-specific binding. The membrane is placed in a

dilute solution of protein - 3-5% bovine serum albumin (BSA) or non-fat dry milk in tris-buffered saline (TBS). The protein in the solution binds to the areas of the membrane that are not occupied by the transferred proteins. After the blocking step, the antibody will be able to bind only to the available binding site of the target protein during the incubation step. The primary antibodies are generated when a host species or immune cell culture is exposed to the protein of interest. The secondary antibodies recognize and bind to the species specific portion of the primary antibody. Therefore, an anti-mouse secondary antibody will bind mouse-sourced primary antibody. The secondary antibody is commonly linked to biotin or horseradish peroxidase (HRP). Horseradish peroxidase (HRP) is used to detect the target protein by chemiluminescence. The chemiluminescence substrate is cleaved by HRP leading to the production of luminescence (Figure 34). The production of luminescence is proportional to the amount of HRP-conjugated secondary antibody. Therefore, indirectly we can measure the presence of the protein of interest. The luminescence is detected by CCD cameras which capture a digital image of the Western blot.

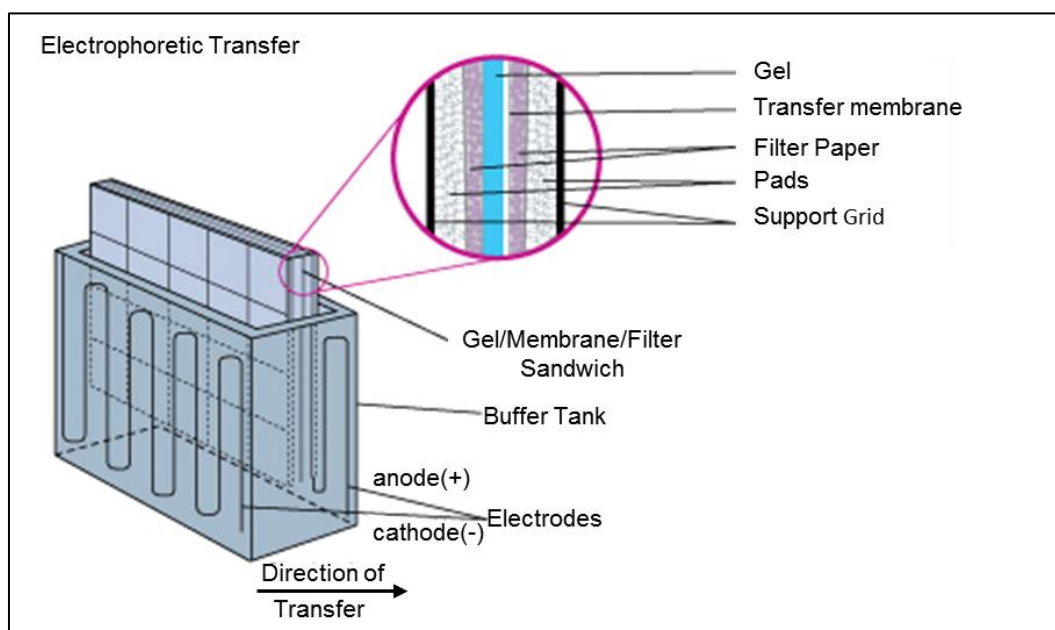


Figure 33. The SDS-PAGE gel is transferred to a Hybond P membrane, which was previously methanol saturated. A gel/membrane/filter sandwich is formed and placed into the buffer tank for transfer at 90 V for 2 h. Adapted from *Biochemistry, Seventh Edition*, 2012.⁷

The antibodies used for immunostaining are listed in the Table 7. Before the antibody incubation, the membrane were incubated in 5% bovine serum albumin (BSA) (Sigma-Aldrich, U.K.) for 1 h to block non-specific binding sites at RT (room temperature). The primary and secondary antibodies were prepared in 5% BSA/TBS-Tween 20 (BSA/TBS (10X TBS pH 7.6, Tris 24.2 g, NaCl 80 g), 0.1% (v/v) Tween 20). The primary antibody was diluted and incubated with the membrane at 4 °C overnight on a shaker in the cold room. The primary antibodies were prepared in a dilution of 1:1000 however, the dilutions for both the primary and secondary antibody need to be determined for each antibody. The membrane was washed with TBS-Tween 20 (TBS/0.1% (v/v) Tween 20, Sigma-Aldrich, U.K.) and incubated with the secondary antibody (HRP-conjugated) for 2 h at RT. Then the membrane was washed with TBS-Tween 20 (TBS/0.1% (v/v) Tween 20) and incubated in enhanced chemiluminescence substrate (ECL, BioRad, U.S.A.) for 5 min at room temperature for the detection of horseradish peroxidase (HRP) activity from antibodies in order to visualise antibody binding.

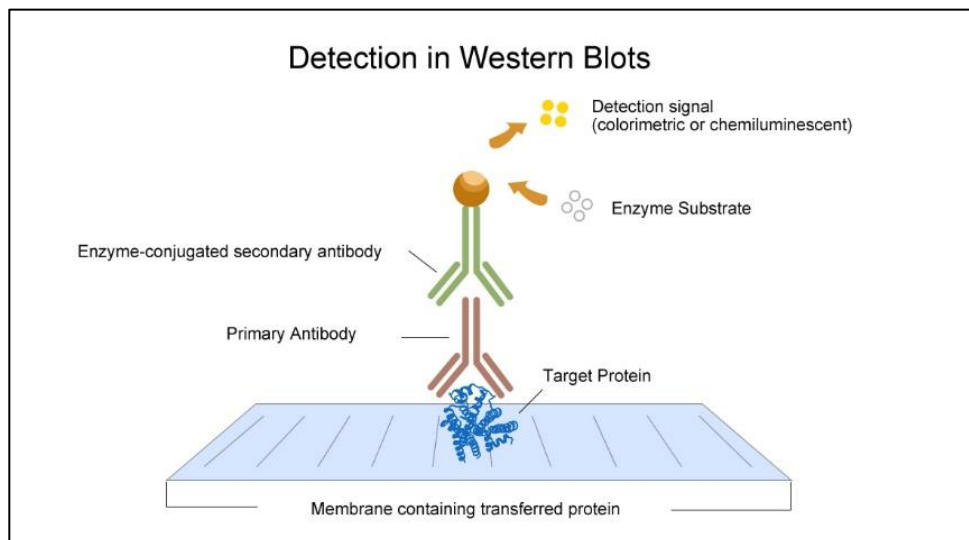


Figure 34. Detection in Western blot analysis. The primary antibody binds to the target protein and secondary antibody binds only to the primary antibody. The detection signal can be either colorimetric or chemiluminescent after the use of an enzyme substrate. Adapted from <https://www.elabscience.com>.

Table 7. Primary and secondary antibody dilutions used in Western blotting analysis				
Antibody	Catalogue Number	Species	Company	Dilution
Anti-phosphotyrosine [PY20]	ab10321	Mouse	Abcam	1:1000
Anti-phospho-EGF receptor (Tyr992)	#2235	Rabbit	Cell signaling	1:1000
Anti-phospho-EGF receptor (Tyr1068) (1H12)	#2236	Mouse	Cell signaling	1:1000
Anti-phospho-EGF receptor (Tyr1173)	Sc12351	Goat	Santa Cruz biotechnology	1:200
Anti-mouse	A9917	Goat	Sigma-Aldrich	1:4000
Anti-rabbit	NA9340V	Donkey	GE Healthcare	1:5000
Anti-goat	Sc2020	Donkey	Santa Cruz biotechnology	1:5000

2.7 Flow cytometry

Flow cell cytometry is a system that is used to sense individual cells in a solution as they move in a focused liquid stream (Figure 35). While the cells flow within the stream, a laser light source is used to scatter light in order to detect the forward and side scattered light from all the cells. Fluorescence is also detected, measured and converted into digitized data. When cells are processed through a flow cytometer, sheath fluid is used to focus hydrodynamically the cells through a nozzle. The cells are then focused to the center of the channel allowing them to pass the laser light one at a time. The sheath fluid is important because it changes the fluid velocity parabola giving rise to higher velocity at the center of the channel. The system operates under laminar flow which prevents the fluid in the central stream to mix with sheath fluid. The detection of the cells after being stained occurs due to the presence of a detector in front of the light beam and measures the forward scatter (FS) and several detectors to the side which are measuring the side scatter (SS). The fluorescence emitted from cells after being stained with specific antibodies conjugated with fluorophores, is detected and measured by the fluorescence detector.

The BD Accuri C6 flow cytometer (BD Biosciences, U.S.A.) was used for multiple experiments such as propidium iodide and study intracellular phosphorylation

staining. This system is equipped with a blue and red laser, two light scatter detectors and four fluorescence detectors with optical filters which are optimized and specific for the detection of Fluorescein Isothiocyanate (FITC), Phycoerythrin (PE), Peridinin-Chlorophyll-Protein PerCP and Allophycocyanin (APC). This system does not require to adjust detector voltages.

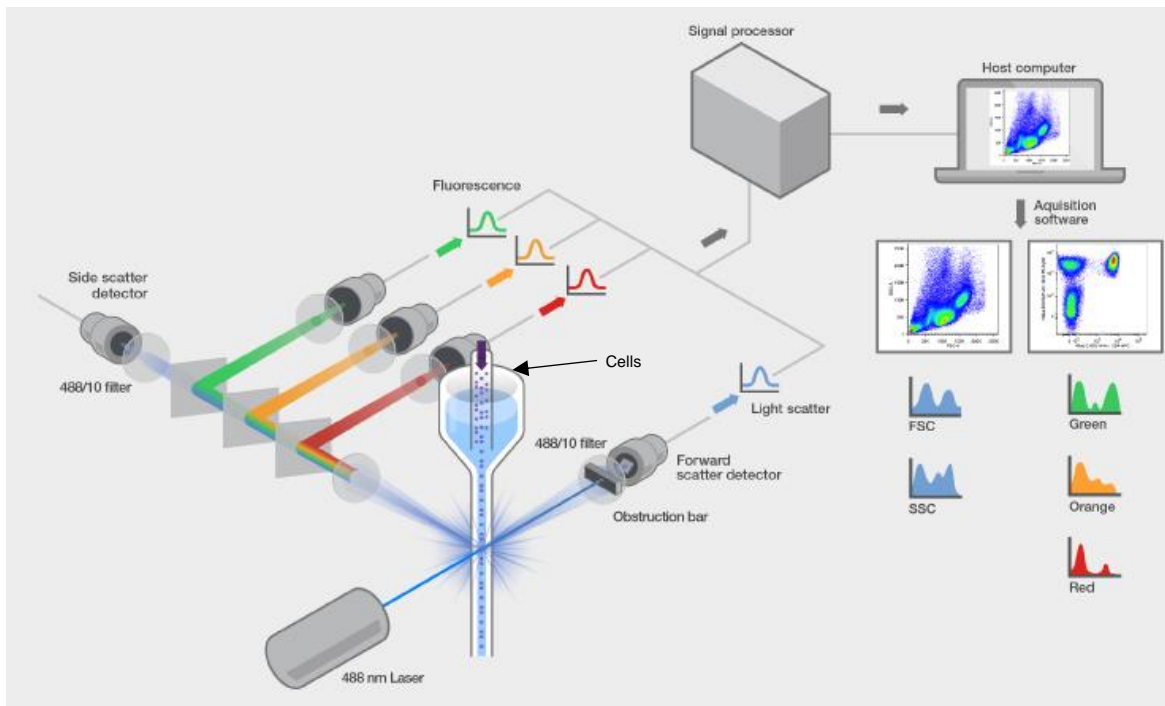


Figure 35. There are 3 main components of a flow cytometer-the fluidics, optics and electronics-that work together to provide a complete system of cell analysis. Adapted from Invitrogen Thermo fisher.

2.8 Gating strategy for cell membrane integrity and cell receptor analysis

The principle of gating has a major role in Flow Cytometry analysis. Gates were placed around the population of HeLa S3 cells that are characterized by common forward scatter, side scatter (Figure 36). For easier identification of the cells, 15 μm particles were run through the flow cytometer in order to be used for easier identification of the HeLa S3 cells because they have similar size (mean $\varnothing = 14.8 \pm 1.3 \mu\text{m}$). The cells size were found to be on the 10^6 side scatter and between 10^6 and 10^7 forward scatter. Investigating the cell membrane integrity was critical in order to confirm that the cells are intact after processing them through the microfluidic device at high velocity. For this purpose, cells were collected after being transported in the microfluidic device. The cells collected from the microfluidic device were stained with propidium iodide and analyzed by flow cytometry. FL3 channel was used to collect/detect the fluorescence of propidium iodide staining of the cells.

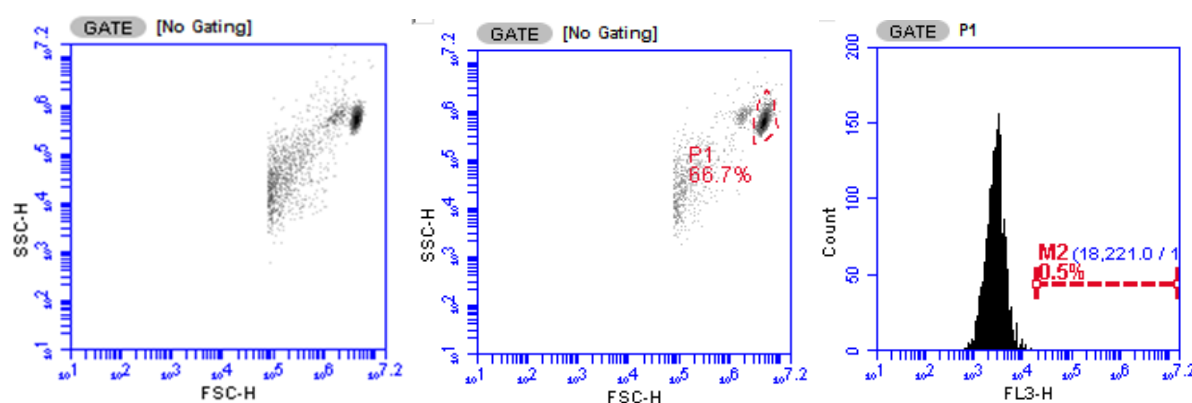


Figure 36. Light scatter plot of HeLa S3 cells (SSC-H/FSC-H). A gate was set to show only the cells (P1). The cells were incubated with propidium iodide (PI). FL3-H channel was used to observe the propidium iodide staining and distinguish alive from dead cells (M2).

2.9 Cell viability assay - Propidium Iodide (PI)

Propidium Iodide is often used to detect dead cells (Figure 37). Propidium Iodide (PI) is an intercalating molecule that normally cannot cross the cell membrane. However, the PI can penetrate the damaged cell membrane and binds to double stranded DNA between base pairs. PI is excited at 488 nm and emits at 617 nm. By using dye exclusion, cells can be distinguished between alive (PI-negative) and dead cells (PI-positive).

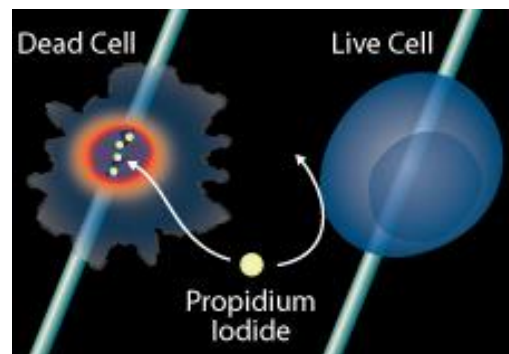


Figure 37. Propidium Iodide (PI) is used to distinguish the dead cells from live cells. Adapted from rndsystems™.

2.10 Cell stimulation, intracellular staining and Flow cytometry

HeLa S3 cells were starved in serum-free medium (DMEM) for 24 h. The cells were collected and counted the next day. Trypan Blue (Sigma-Aldrich, U.K.) was used to quantify the percentage (%) of live-dead cells. 1×10^6 cells mL^{-1} were processed through the microfluidic device where they became stimulated by EGF (100 ng/mL) for a defined time based on the length of the incubation channel and subsequently quenched by 4% paraformaldehyde (PFA). In order to keep the temperature constant at 37 °C, a thermal stage, thermal gel packs and pre-warmed buffers were used. Cells were collected from the cell outlet of the PDMS device after being stimulated with 100 ng/mL (final concentration) of epidermal growth factor (EGF) that caused phosphorylation of the tyrosine residues of the EGF receptor (Figure 38 A). The cells

were fixed using 4% Paraformaldehyde (PFA) to preserve the reaction intermediates (Figure 38 B). A 1x cocktail of protease and phosphatase inhibitors (Halt™ Protease and Phosphatase Inhibitors 100x, Thermo Fisher Scientific, U.S.A.) was used to prevent protein degradation and dephosphorylation by proteases and phosphatases. The cells were centrifuged at 400xg for 10 min. The supernatant was aspirated and the cell pellet was resuspended in 3 mL of 1X PBS/1%BSA and then centrifuged at 400xg for 10 min. The supernatant was aspirated and the cell membrane was permeabilized using 0.2% Tween 20/PBS 1X for 15 min (Figure 39). The cell pellet obtained by centrifugation and the supernatant was aspirated. The cells were incubated for 1 hr with human-EGF Receptor pY1173 antibody (Miltenyi Biotec) which is conjugated with phycoerythrin (PE), human-EGF Receptor pY1068 antibody (Miltenyi Biotec) conjugated with allophycocyanin (APC) and Anti-EGFR antibody conjugated with Fluorescein isothiocyanate (FITC) in the dark at room temperature ~21 °C (Table 8). The protocol was adapted from a published article by Krutzik and Nolan in 2003 where they performed intracellular phospho-protein staining techniques for Flow cytometry.⁹⁵ The Flow cytometry analysis was performed using BD Accuri C6 (BD Biosciences, Franklin Lakes, New Jersey, United States). The cell flows within the flow cytometer and a laser beam and detectors measure the light scattering and fluorescent emission. In addition, flow cytometry gives the ability to the user to select the number of events needed (1 event = 1 cell) and it removes the outliers automatically. The experiments in Chapter 4.4 (experiment 1 - 25, 50, 100 ms and experiment 2 – 25, 50, 75, 100, 250, 500, 750 ms) were performed only once ($n = 1$) except for the three time points 25, 50 and 100 ms ($n = 2$). For each time point, we captured 500 events (a large sample size to lower the margin of error and provide more data to work with) which were recorded by the Flow cytometer. The median fluorescence intensity (M.F.I.) value of each event was plotted and further statistical analysis was performed.

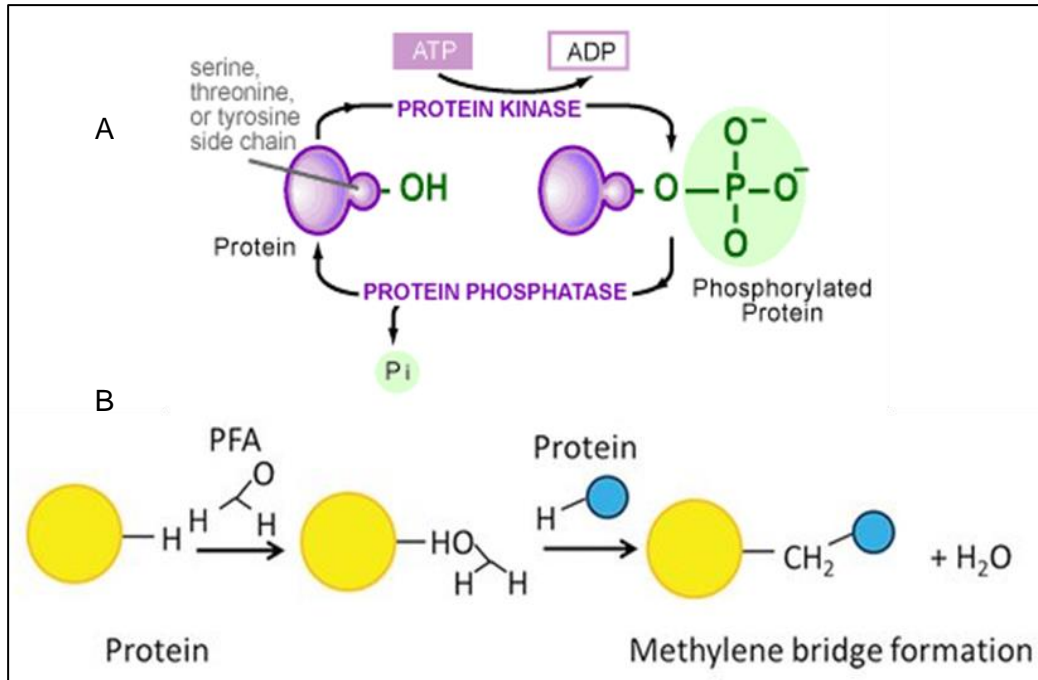


Figure 38. Protein kinase and phosphatase have an impact on the phosphorylation and dephosphorylation of proteins (A), Chemical reactions through which paraformaldehyde (PFA) crosslinks proteins (B). Adapted from Secko, 2003.⁶⁰

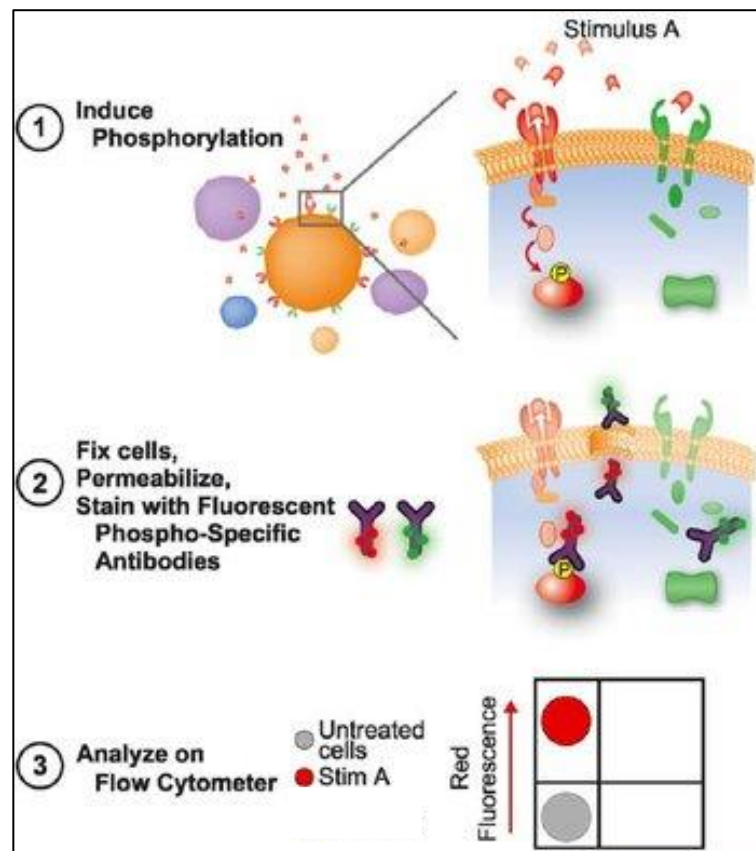


Figure 39. Binding of stimulus A (EGF) to the binding domain of the receptor induced phosphorylation (1), Cells were fixed, permeabilized and stained with phospho-specific primary antibodies (B). Flow cytometry was used to analyse the cells and find the levels of phosphorylation compared to the untreated cells (C). Adapted from Krutzik et al., 2004.⁹⁶

Table 8. Antibody dilutions used for flow cytometry.

Antibody	Catalogue number	Company	Dilution	Conjugation
Anti-phospho-Tyr1173-EGFR	130-110-541	Miltenyi Biotec	1:50	PE
Anti-phospho-Tyr1068-EGFR	130-110-042	Miltenyi Biotec	5:50	APC
Anti-EGFR	10001-MM08-F	Sino Biological	1:50	FITC
Anti-HER2	130-106-696	Miltenyi Biotec	1:50	APC

2.11 Statistical analysis

The median fluorescence intensity (M.F.I.) values of 500 events collected with Flow cytometry for each time point (Chapter 4.4 experiment 1 & 2) were added in GraphPad Prism version 8.0.2. We tested the normality of the data using two different methods. QQ plots and D' Agostino-Pearson normality test were used to determine whether the data obtained with the flow cytometer in experiment 1 (25, 50, 100 ms) and experiment 2 (25, 50, 75, 100, 250, 500, 750 ms) are normally distributed (Gaussian distribution). QQ plot is a probability plot that compares two probability distributions by plotting their quantiles against each other. Prism plots the actual Y values on the horizontal axis, and the predicted Y values (assuming sampling from a Gaussian distribution) on the Y axis. If the data were sampled from a Gaussian distribution, you expect the points to follow a straight line that matches the line of identity. The points in the QQ plot will approximately lie on the line $y = x$. It was found that the data did not follow a straight line. D' Agostino-Pearson normality test was also used. In this test, Prism uses the traditional 0.05 cut-off to answer the question whether the data passed the normality test. If $p \geq 0.05$, the data are normally distributed and if $p \leq 0.05$, the data are not normally distributed. Both normality tests showed that the data are not normally distributed. Therefore, we used One-Way ANOVA non-parametric test for the analysis of our data, Kruskal-Wallis followed by Dunn's *post hoc*. p -values ≥ 0.05 were considered statistically significant. The Kruskal-Wallis test is a nonparametric test that compares three or more unmatched groups. Dunn's multiple comparisons test compares the difference in the sum of ranks between two columns with the expected average difference (based on the number of groups and their sizes).

3. Results – Chip optimization and evaluation

3.1 Microfluidic circuit development and characterisation

According to the inertial focusing principles, inertial focusing occurs when inertial lift forces act on the particle within a microchannel that is no more than 7-fold wider than the cell diameter (HeLa S3 have a diameter \varnothing cell of $14.8 \pm 1.3 \mu\text{m}$) or $\alpha/w \geq 0.2$ (α : particle diameter, w : channel width) in order to achieve precise focusing of particles to two equilibrium positions in a rectangular channel ($h > w$). A volumetric flow ratio of 2:1 produced two ligand stream widths (82% total) and a cell stream (18%), respectively as a consequence of the velocity parabola with higher velocity streams in the channel centre (Figure 40). This means the narrow central stream had an equal volumetric flow rate to each flanking stream.

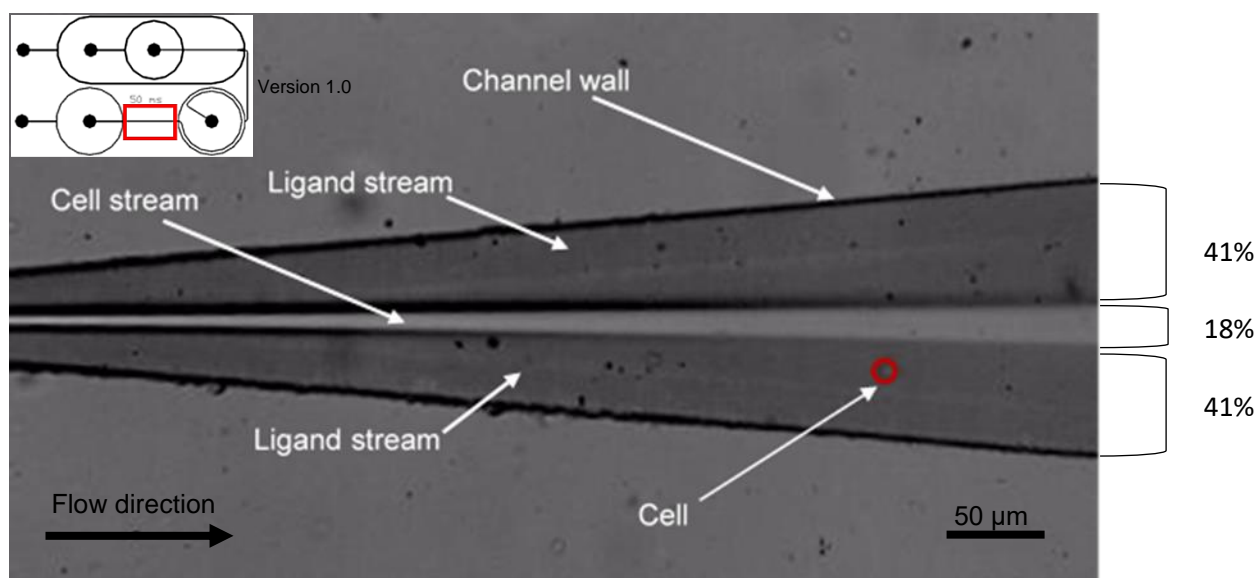


Figure 40. HeLa S3 cells were transported from the cell stream into the ligand streams due to wall and shear lift forces within the $h > w$ microchannel (width: $50 \mu\text{m}$ and height: $85 \mu\text{m}$ version 1.0) and directed cells to equilibrium positions with a volumetric distribution ratio of 2:1 in a microfluidic device version 1.0. (Number of repeats = 3).

3.2 Determination of the optimal dimensions for the inertial focusing element

A series of experiments were performed to determine the optimal length of the inertial microfluidic channel and velocity required in order for the cells to become inertially focused, submerged onto the ligand streams and stimulated. For this

purpose, 15 μm red fluorescent, polystyrene particles were used as models of HeLa S3 cells due to their size and density ($\rho = 1.05 \text{ g/cm}^3$) similarities (Figure 41).

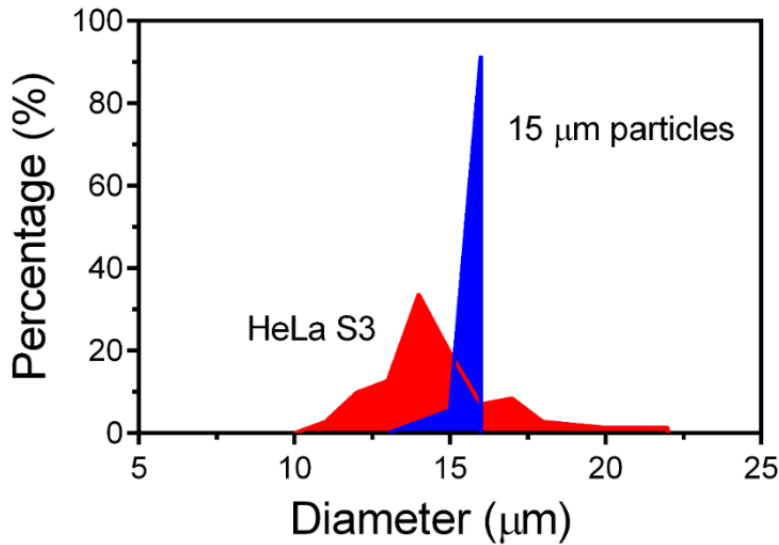


Figure 41. 15 μm -diameter polystyrene particles and HeLa S3 size distribution (mean $\bar{\phi} = 14.8 \pm 1.3 \mu\text{m}$, number of cells = 100).

These experiments were performed in the microfluidic circuit version 1.0 (See Chapter 2.2, Table 2) and were characterized by an inertial microfluidic channel that varied in length (1-8 mm) and with channel dimensions of 50 μm width and 85 μm height. A volumetric flow ratio of 2:1 ('Ligand': 'Cells'), $2.5 \times 10^5 \text{ particles mL}^{-1}$ and a $\bar{u}_{flow} = 1.58 \text{ m/s}$ (\bar{u}_{flow} within the inertial focusing channel) were used to investigate the focusing of the 15 μm polystyrene particles and cells (Figure 42 & 44). The high-speed camera was used to image particle positions. The relative centroid position of the particles within the channel was found using the equations described in Figure 31 in Chapter 2 and ImageJ. It was observed that the particles in a 6 mm focusing length channel were efficiently focused (>95%) and fully displaced from the central stream onto the 'ligand' streams (Figure 42). The maximum switch time for the particles with a transport velocity ($\bar{u} = 1.6 \text{ m/s}$) was 3.75 ms. The -2 mm and 0 mm length described the particle positions as they entered the microfluidic circuit. The particles were laterally hydrodynamically focused by the ligand sheath flow.

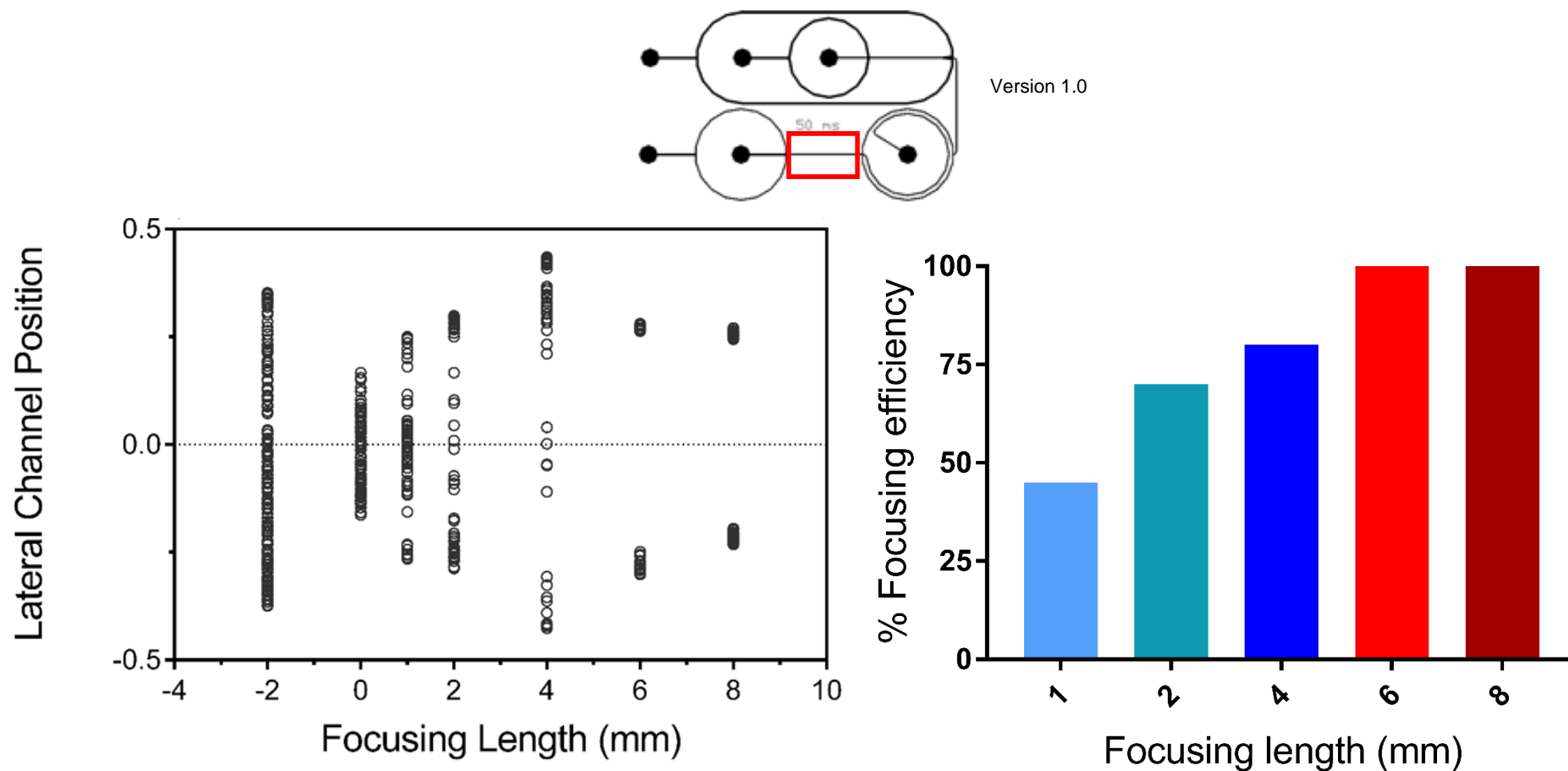


Figure 42. Centroid position of 15 μm polystyrene particles (Count= 100 particles for each device) in microfluidic devices version 1.0 (λ : aspect ratio=1.7, width: 50 μm and height: 85 μm) with inertial focusing channel of different lengths (1-8 mm, area highlighted in red on the microfluidic outline). The shortest and most effective focusing length resulting to the lowest switch time for 15 μm particles is the device with a 6 mm focusing length. (Number of repeats = 1).

In addition, different range of velocities were used to identify the lowest and highest velocity able for rapid focusing of particles to two equilibrium positions in a 6 mm focusing length microfluidic circuit (see Chapter 2.2, Table 2). A statistically rich ($N=1,000-10,000$) particle position analysis to assess the effect of length and velocity on inertial focusing was obtained using $15\ \mu\text{m}$ fluorescent particles (0.5×10^6 particles mL^{-1}) and a fluorescence microscope (20X objective, Figure 43). ImageJ was used for data analysis. It was found that a velocity range between $0.75\ \text{m/s}$ and $1.0\ \text{m/s}$ could be used to achieve focusing of particles to two equilibrium positions with $\tau_{\text{switch}} = 8\ \text{ms}$ and $\tau_{\text{switch}} = 6\ \text{ms}$, respectively (Figure 43). The precise focusing of particles within the microfluidic channel required channel dimensions $<5-7$ particle diameter or $a/w \geq 0.2$.⁹ The particle/cell relative scale to the width was 0.33 ($15/50$). However, the use of a velocity ($1.50\ \text{m/s}$) led to the translation from two to four equilibrium positions (Figure 43). At higher velocities ($2.0\ \text{m/s}$ and $2.5\ \text{m/s}$), the number of particles in the central stream ('cell stream') was higher compared to the 'ligand streams'. This was an indication that the particles were focused into four equilibrium positions at higher velocities and this was predicted by the higher particle's Reynolds number ($Rp > 5$).⁹ These experiments allowed to identify the length of the inertial focusing channel and the velocity required for the efficient establishment of the particles to two equilibrium positions. However, it was necessary to achieve shorter switch times and higher velocities.

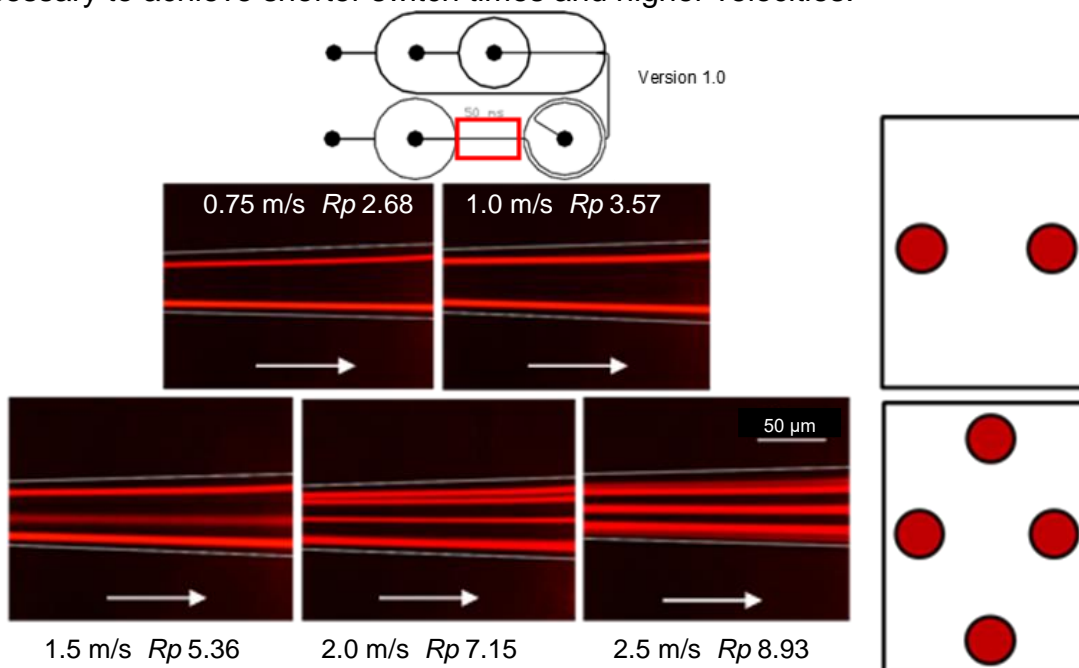


Figure 43. Images of fluorescent polystyrene particles ($15\ \mu\text{m}$, exposure: $2000\ \mu\text{s}$ and concentration: 0.25×10^6) within a $6\ \text{mm}$ length inertial microfluidic channel with λ (aspect ratio= 1.7 , width: $50\ \mu\text{m}$ and height: $85\ \mu\text{m}$, version 1.0) transported using different velocity conditions. (Number of repeats = 3).

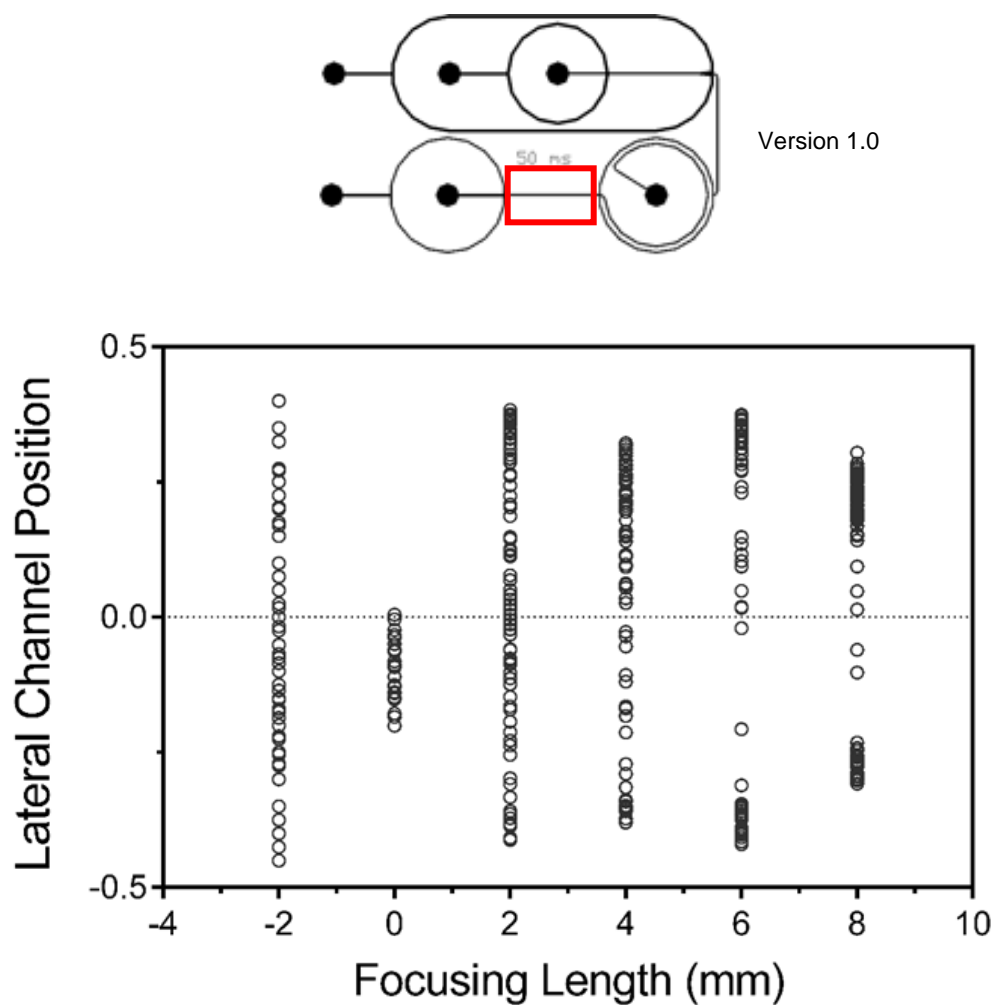


Figure 44. Centroid position of HeLa S3 cells (Count = 100 cells per device) in microfluidic devices (λ : aspect ratio=1.7, width: 50 μm and height: 85 μm , version 1.0) with inertial focusing channel of different lengths (1-8 mm). The shortest and most effective focusing length resulting to the lowest switch time for HeLa S3 cells is the device with a 6 mm focusing length. (Number of repeats = 1).

3.3 Investigating the effect of channel miniaturisation

It was important to optimize the microfluidic device and improve the switch time by increasing the velocity of the particles and on the same time minimize the development of the 4 equilibrium positions. Thus, an alternative miniaturised device was tested to investigate the effect of confinement by increasing the α/w ratio. The new device (version 1.5, see Chapter 2.2, Table 3) had a 4 mm focusing length channel and smaller dimensions (width= 25 μm and height= 50 μm) compared to the microfluidic device version 1.0. A 2:1 volumetric flow ratio with 15 μm fluorescent particle concentrations (0.5×10^6 particles mL^{-1}) and a range of velocities was used (Figure 45).

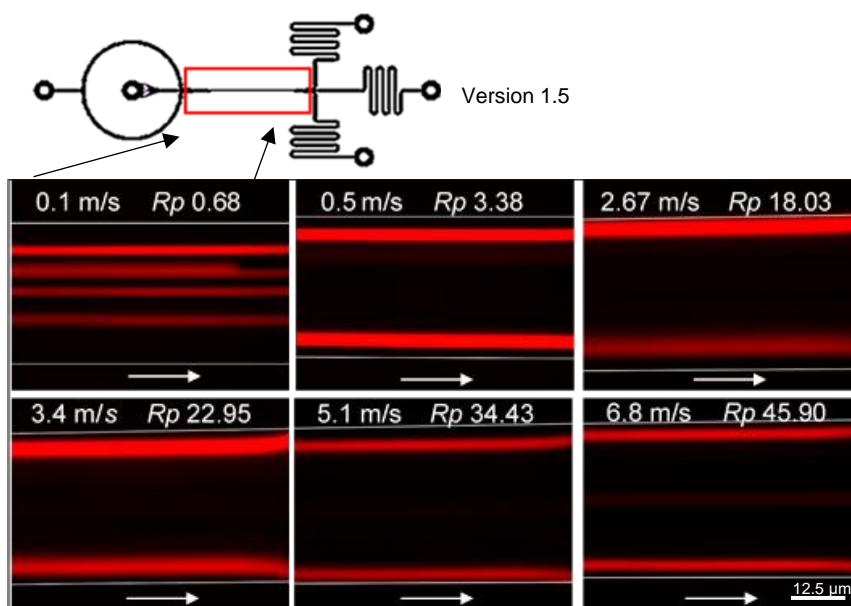


Figure 45. Fluorescent polystyrene particles (15 μm) were transported into a 4 mm inertial microfluidic channel with the following dimensions (λ : aspect ratio=2, width: 25 μm and height: 50 μm , version 1.5). Each velocity and the particles Reynolds number can be found above each image. (Number of repeats = 3).

According to the general background, the particle Reynolds number should be ≥ 1 and no more than 5-7 in order to achieve focusing to two equilibrium positions.⁹ However, the data collected showed that the particles Reynolds number greatly exceeded ($Rp > 45$) the range required for focusing of particles to two equilibrium positions. This observation was important because we were able to transport particles using faster velocities (e.g. 2.67 m/s or 6.8 m/s, Figure 45) thus, the switch time was much shorter (~ 1.5 ms and ~ 0.6 ms, respectively) compared to the previous experiment with the microfluidic device version 1.0 (1 m/s \rightarrow switch time of 6 ms, Figure 42) where the device was operating in $Rp = 2.68$ -8.93. Focusing to two

equilibrium positions was related to the particle Reynolds number but not restricted to the 1-5 range. Possible factors were the particle-channel width ratio and possibly the w/h aspect ratio (here 2.0 compared to 1.7 previously). The effect of the w/h aspect ratio was evaluated by using devices (e.g. $50/25 = 2$ or $65/30 = 2.16$) that exceeded the w/h aspect ratio values of the devices (version 1.0) that had been used. One more factor was the cell size. The larger the cells, the bigger the shear force on them as a consequence of the bigger difference at wall and at channel centre velocities. Evaluating the data, it was found that the miniaturization of the channels allowed shorter switch times of cells due to the higher velocities used and prevented the establishment of four equilibrium positions.

3.4 A new microfluidic circuit to improve focusing and obtain shorter switch times

Based on the collected data, new microfluidic devices (version 2.0) were designed in order to develop an optimal ultra-fast microfluidic device with high cell-processing throughput and even shorter switch times. Each microfluidic device was designed and characterized separately in order to find the optimal conditions for high efficiency of cell focusing. The focusing channel dimensions were $30\ \mu\text{m}$ width and $65\ \mu\text{m}$ height (Figure 46). The dimensions of the focusing channel were decreased compared to the previous microfluidic circuit version 1.0 ($50\ \mu\text{m}$ wide and $85\ \mu\text{m}$ high) and they were designed based on the observations on the microfluidic device version 1.5 (width: $25\ \mu\text{m}$ and height: $50\ \mu\text{m}$, Chapter 3.3, Figure 45) where $15\ \mu\text{m}$ polystyrene particles were focused to two equilibrium positions over $4\ \text{mm}$ in a shorter switch time period ($\sim 0.6\ \text{ms}$) with higher mean flow velocities ($\leq 6.8\ \text{m/s}$). The new designs were used to identify the shortest length possible for focusing of particles ($2.5 \times 10^5\ \text{mL}^{-1}$) to two equilibrium positions in a focusing channel and to develop an optimal circuit. The RV1, RV2 and RV3 devices (Chapter 2.2, table 4) were used for the design of the optimal resistors in Version 2.0.

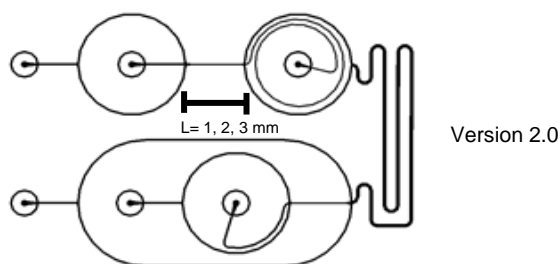


Figure 46. Microfluidic inertial focusing device (width: $30\ \mu\text{m}$, height: $65\ \mu\text{m}$, version 2.0) with various inertial focusing channel lengths in order to identify the shortest length possible for efficient focusing of particles to two equilibrium positions.

The particles were focused to two equilibrium positions when processed with either a mean flow velocity of 2.5 m/s, 3.4 m/s or 4.3 m/s in a 5 mm inertial focusing length channel (Figure 47). These velocities and the length of the focusing channel allowed switch times of 2 ms, 1.5 ms and 1.2 ms, respectively. The particle Reynolds number for each velocity was found to be >13 . According to the general rules of inertial focusing if the particle Reynolds number is above 5, the particles were focused onto 4 equilibrium positions within the microfluidic channel.⁹ However, this was not occurring. Instead, the particles were focused to two equilibrium positions in a high velocity regime. One possible explanation was that the particles pathway to reach the 4 equilibrium positions became restricted due to the confinement and miniaturization of the microfluidic channel. Hence, the particles were not able to reach the 4 equilibrium positions and they remained to 2 equilibrium positions. In addition, the aspect ratio of the channel (w/h) was 2.16 and was higher compared to the literature ($w/h=2$) and the aspect ratio of the channel from the microfluidic circuit version 1.0 ($w/h=1.7$). This was an indication that the focusing of particles was highly sensitive to the aspect ratio. The higher aspect ratio helped because at high velocities the PDMS started to deform, this was difficult to observe but it changed the shape of the channel towards a rounded rectangle, favouring the emergence of the 3rd and 4th equilibrium positions. Particles were also processed with a mean velocity of 4 m/s in a 3 mm focusing length device and they were focused to two lateral equilibrium positions.

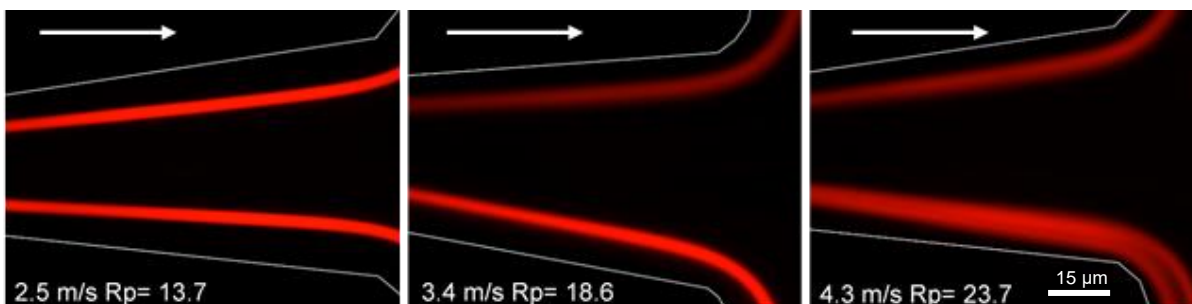
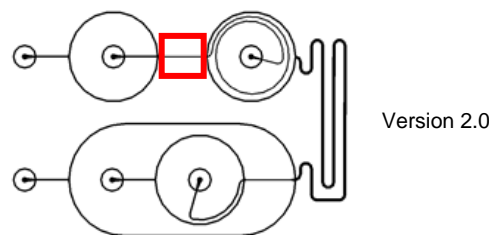


Figure 47. The fluorescent particles (15 μm) were inertially focused to two equilibrium position in a 5 mm length channel (version 2.0) flown with three different velocities. The Rp (particle Reynolds number) was found to be significantly higher compared to the generalised rules of inertial focusing. (Number of repeats = 3).

The findings obtained using fluorescent particles on the microfluidic circuit version 2.0 were promising, the same experimental methodology was used on HeLa S3 cells in order to examine their focusing efficiency using a mean flow velocity of 4 m/s through three identical microfluidic devices (version 2.0, width: 30 μm and height: 65 μm) that only differ by the length of the inertial focusing channel (1 mm, 2 mm and 3mm, Figure 48). It was found that the shortest length required to focus cells to two equilibrium positions was a channel of 2 mm length with switch times of approximately 500 μs . The samples from each outlet (flanks and central) were collected and processed through a flow cytometer in order to find the percentage of cells focussed to the flanking or central outlets. It was found that the focusing efficiency was extremely high (>86%) even in the shortest focusing channel element (1 mm, Figure 48). It was found that the inertial focusing channel with the following dimensions: 30 μm width, 65 μm height and a length of 2 mm allowed high efficiency of focusing to the flanks (high efficiency of focusing to the flanks \rightarrow higher number of cells submerged into the ligand) and short switch times (500 μs).

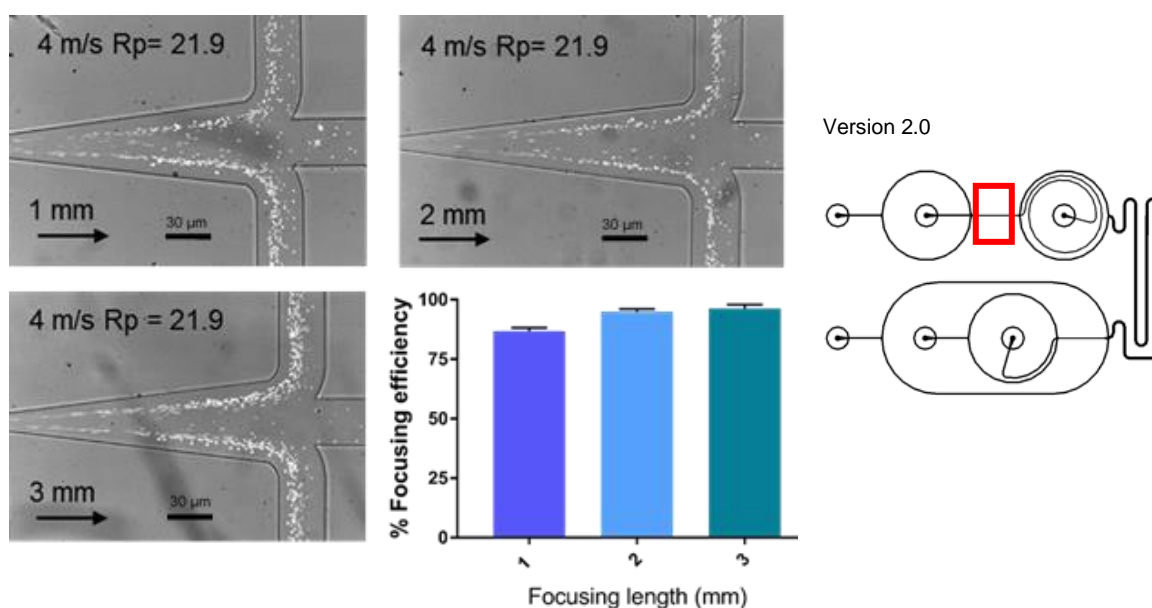


Figure 48. HeLa S3 cells were focused into two equilibrium positions when transported with a mean velocity of 4 m/s. The three different devices (version 2.0) that varied only by the length of their focusing channel (1 mm, 2 mm and 3 mm, respectively) are characterized by high efficiency of focusing (1 mm: Mean focusing efficiency = 86.67% (+SD), 2 mm: Mean focusing efficiency = 95.00% (+SD), 3 mm: Mean focusing efficiency = 96.33% (+SD), $n=3$, cell counts= 10000 cells)). The shortest length required for highly efficient focusing was 2 mm. The particle Reynolds number was 21.9. More than the value of the particle Reynolds number anticipated by general design rules (Di Carlo, 2009). (Number of repeats = 3).

In addition, another important feature examined in the inertial microfluidic element (30 μm width, 65 μm height and a length of 2 mm) was the effect of transport cell velocity on the efficiency of focusing and be able to achieve longer incubation times (1000-2000 ms). Different velocities were used (0.5 m/s, 1 m/s and 2 m/s) on the cells and was found that the minimum mean velocity required to establish the cells to two equilibrium positions on a 2 mm length channel was 1 m/s (Figure 49). Slower transport velocities enabled the use of shorter incubation channels with operation at reduced pressures.

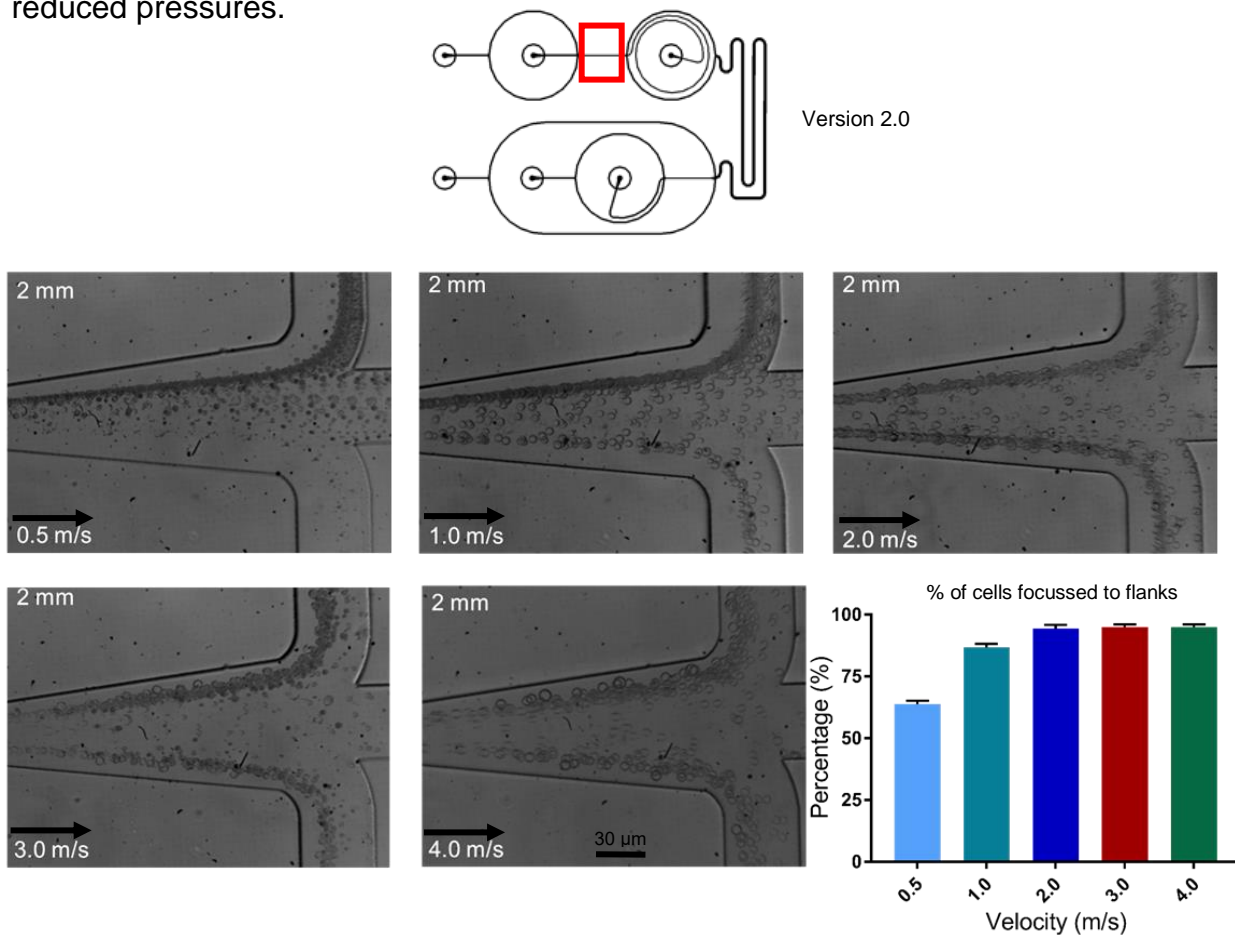


Figure 49. The slowest velocity required for focusing of HeLa S3 cells in a 2 mm length channel device (version 2.0) to two equilibrium positions is 1 m/s. A slower velocity (0.5 m/s) and subsequently the forces within the channel were not efficient enough to establish them to focusing positions. Hence, a high number of cells were not focused and were discarded out of the device. The total cell number processed through the device was $\sim 10,000$ cells. The mean number of cells (%) efficiently focused to the flanks operating with 1, 2, 3, 4 m/s was $>85\%$ (+SD). (Number of repeats = 3).

3.5 Cell viability is not affected by inertial microfluidic transport

The high speed processing of cells within the microfluidic devices raised the question of the cell viability. It was important to know if the cell membrane integrity of the cells was intact. Therefore, HeLa S3 cells were processed through a microfluidic device (Version 1.5, width: 25 μm , height: 50 μm and a focusing channel of 4 mm length). The cells were processed at different velocities and were collected and a cell viability assay was performed using propidium iodide (1 $\mu\text{g}/\text{mL}$) staining. Propidium iodide is impermeable to intact plasma membrane but intercalates with DNA or RNA upon membrane damage and emits a red fluorescent signal. Flow cytometry was used to provide a rapid method to quantify the dead cells from the viable cells. The data obtained during this experiment (Figure 50) revealed that the cells could be processed within the microfluidic device with velocities of 6.8 m/s without being damaged. This validated that high velocities can be used to achieve millisecond cell processing without effecting the integrity of the cell membrane and the capacity for authentic EGFR signal transduction.

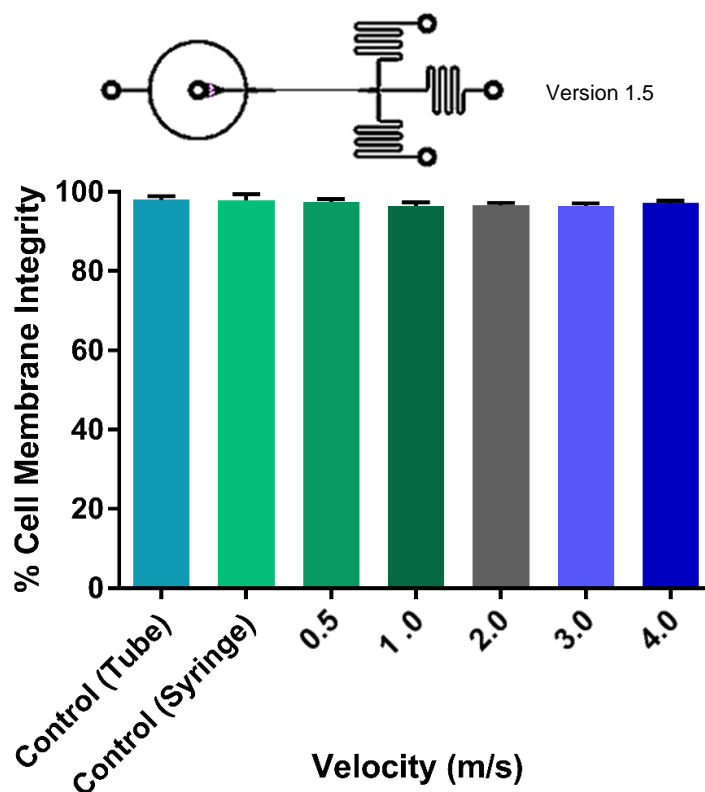


Figure 50. Propidium iodide (PI) staining was performed to assess the viability of HeLa S3 cells in a tube and HeLa S3 cells after being processed with various high velocities within an inertial microfluidic device version 1.5. It was found that the viability of cells was as high (>85% +SD) as the cells in the control sample. Cell count on the Flow Cytometer = 3000 cells. (Number of repeats = 3)

The velocity parabola is known to be 1.5-fold mean velocity at the mid-height/centre and zero at the no-slip boundary. This produces a huge CV (~40-60%). Therefore, the velocity of the transported cells is not uniform and leading to a huge CV. The incubation time of cells is an important factor in the study of receptor activation dynamics. It was important to achieve similar incubation times for cell EGFR with the EGF ligand in order to achieve uniform millisecond cell incubations, reduced background noise and errors in the data. For assessing the incubation channel and its efficiency to cause uniform cell incubation times, rapid incubation experiments were performed. The first experiment was performed using fluorescent polystyrene particles ($2.5 \times 10^5 \text{ mL}^{-1}$) in order to examine if they were focused into a common position within the incubation channel (Dean flow element microfluidic circuit, Chapter 2.2, Table 5) while they were transported with a mean flow velocity, \bar{u} flow of 0.34 m/s to understand the effect of channel aspect ratio of focusing and particle transport velocity. The velocity was slow as a consequence of losing volume at the first resistor and because of the channel width (sub-1.0 aspect ratio). A fluorescence microscope (Olympus Lifescience IX70 fluorescence microscope) and a high exposure time (>1000 ms) were used to record the trajectories of the particles (Figure 51). It was observed that the particles attain two equilibrium positions (resulting from upstream inertial focusing) before they entered the first curvature of the incubation channel. When the particles exited the curvature, they were focused to a common position in the incubation channel (1:3 aspect ratio) with a mean flow velocity of 340 mm/s. This was also observed by Ramachandraiah and colleagues in 2014.⁸⁰ In addition, it was found that the particles remained in a common position at the end of the incubation channel (Figure 52). The common position of the particles was an indication of possible uniform velocity and subsequently, uniform incubation time. The collected data allowed a better understanding of the importance of channel ratio and curvature to attain uniform velocity and uniform incubation times.

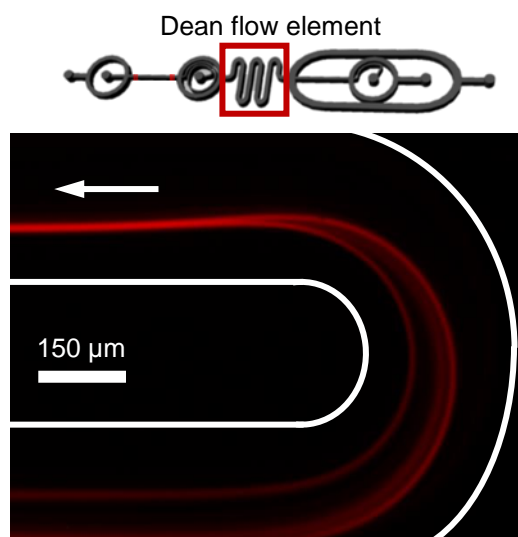


Figure 51. The particles entered the curvature at two equilibrium positions in a Dean flow element device (chapter 2.2, table 5). They were established to a common equilibrium position nearly instantaneous when they left the channel curvature. The channel width was $250\ \mu\text{m}$ (1:3 aspect ratio) and the radius of the curvature was $250\ \mu\text{m}$. (Number of repeats = 3).

Further validation of the uniform incubation times and the important role of the curvatures was also revealed (Figure 52). The quantified particle velocity showed that the velocity of particles was <5 times less compared to the initial \bar{u} flow as a consequence of widening the channel to $250\ \mu\text{m}$ (Figure 52). In addition, it was clear that the particles in a mean flow velocity of $340\ \text{mm/s}$ within the incubation channel (high velocity) were localised to a common position compared to the particles transported with a medium ($34\ \text{mm/s}$) or slow velocity ($2.6\ \text{mm/s}$), respectively. Transport at the same velocity ($340\ \text{mm/s}$) was an indication that the particles were focused to the same vertical position, therefore resulting in a uniform incubation time. Furthermore, the curves were a component of the incubation channel that had a major impact on the focusing of particles to a common position due to the influence of the Dean forces subsequently leading to focusing of particles to a common lateral position exiting the curvatures. Confirmation of this assumption was done by validating the collected data using mTrackJ. It was found that the particles transported with a velocity of $340\ \text{mm/s}$ were vertically focused at the channel lateral midline and they had uniform velocities ($\text{CV} = 1.2\%$). On the other hand, the unfocused particles in slower velocities varied significantly ($\text{CV} = 8.5\%$ and $\text{CV} = 37.2\%$, respectively). These measurements were documented in Figure 52.

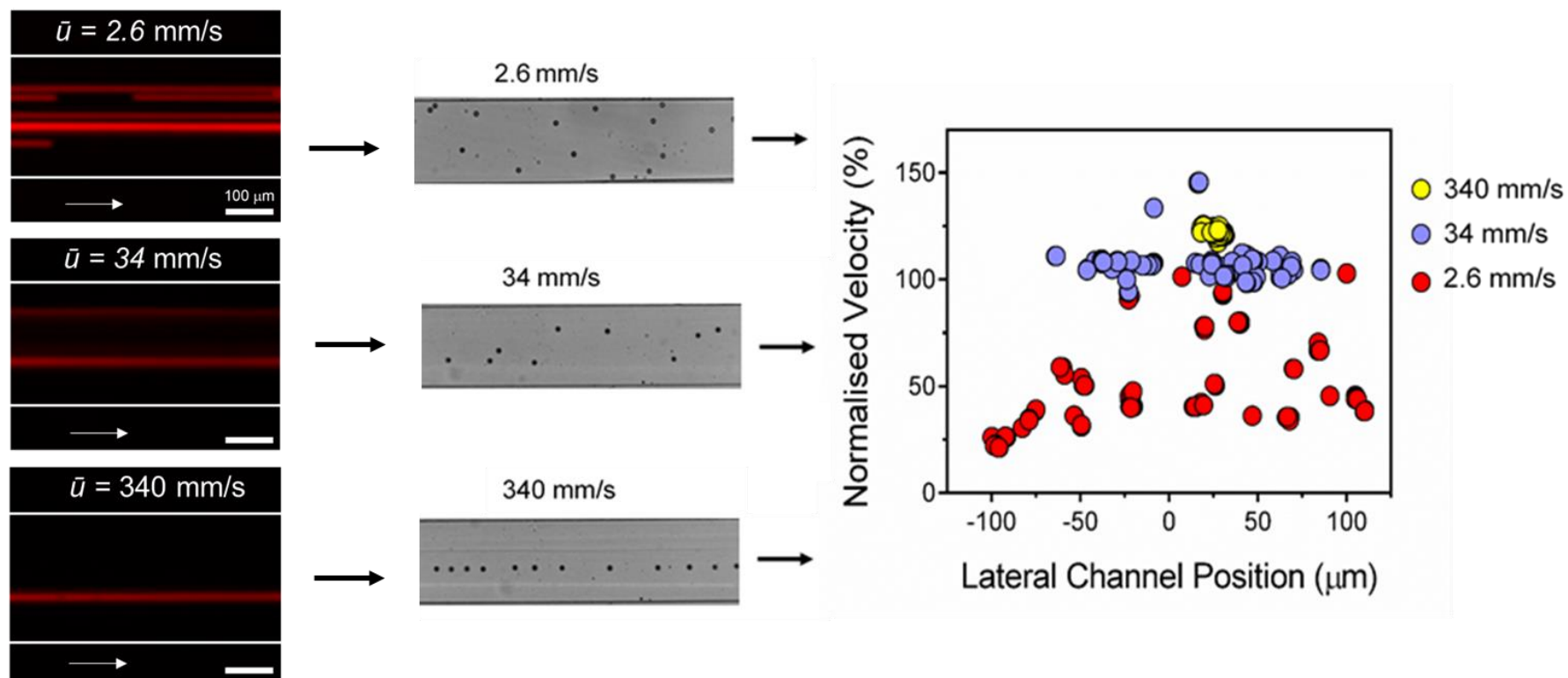


Figure 52. The fluorescent particles with a \bar{u}_{flow} of 340 mm/s remained in a common position at the end of the incubation channel. This indicated a possible uniform velocity and a uniform incubation time. If the particles are transported with a slower mean flow velocity (e.g. 34 mm/s) upstream inertial focusing is possible, as Dean-coupled inertial focusing is absent. At still lower velocities (2.6 mm/s) they were found in random positions. Therefore, there was no uniform velocity and uniform incubation time. Low velocity transport produced random positions with highly varied velocity distributions (CV= 37.2%), whereas high velocity transport focused the particles to provide uniform velocities (CV= 1.2%) and therefore, uniform incubation times. (Number of repeats = 3).

3.7 The aspect ratio of the incubation channel influences incubation time control

The incubation of cells within the incubation channel is one of the most important factors for time control. Dean flow can be effectively used to control the incubation times. However, Dean flow can be influenced by several factors such as the aspect ratio of the incubation channel (Figure 53) or the velocity influences Dean-coupled inertial focusing to attain uniform incubation times.⁸¹ Particles and HeLa S3 cells were processed with the same velocity in devices that had different aspect ratio incubation channels (Figure 54 & 55). It was found that particles within the incubation channels with an aspect ratio of 1:1 ($w=60\ \mu\text{m}$), 1:2 ($w=120\ \mu\text{m}$), and 1:3 ($w=180\ \mu\text{m}$) were aligned to a common position. In addition, the cells were characterized by a low velocity coefficient of variation (3.3%, 0.7% and 1.3%, respectively, Figure 54 & 55) suitable for reproducible incubation times. In addition, the channel with 1:4 aspect ratio had the highest velocity CV (5%) compared to all the other channels. This is indicating that the channel should not have an aspect ratio of 1:4 because lower CV's can be achieved with the other aspect ratio channels.

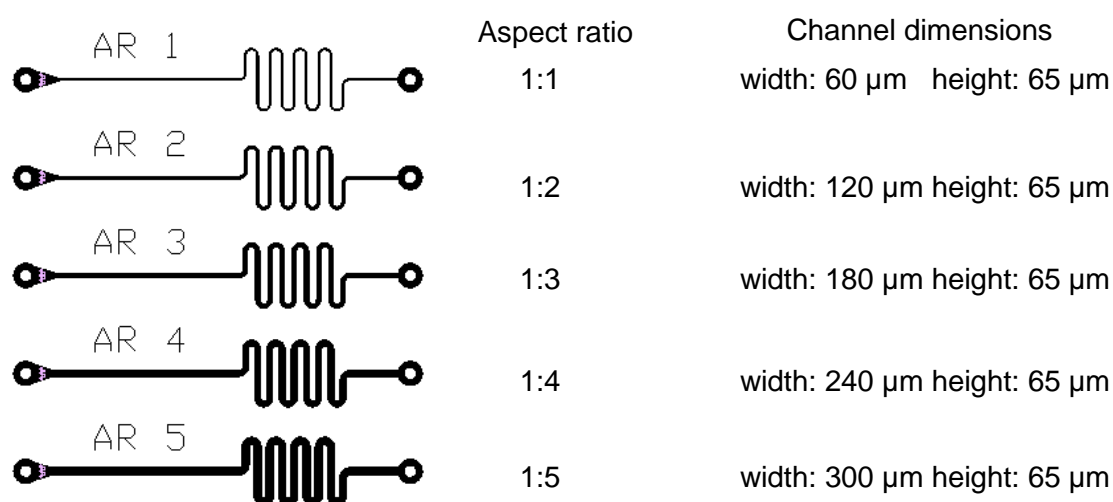


Figure 53. Incubation channel elements used to identify the optimal channel dimensions and aspect ratios to achieve reproducible incubation time control.

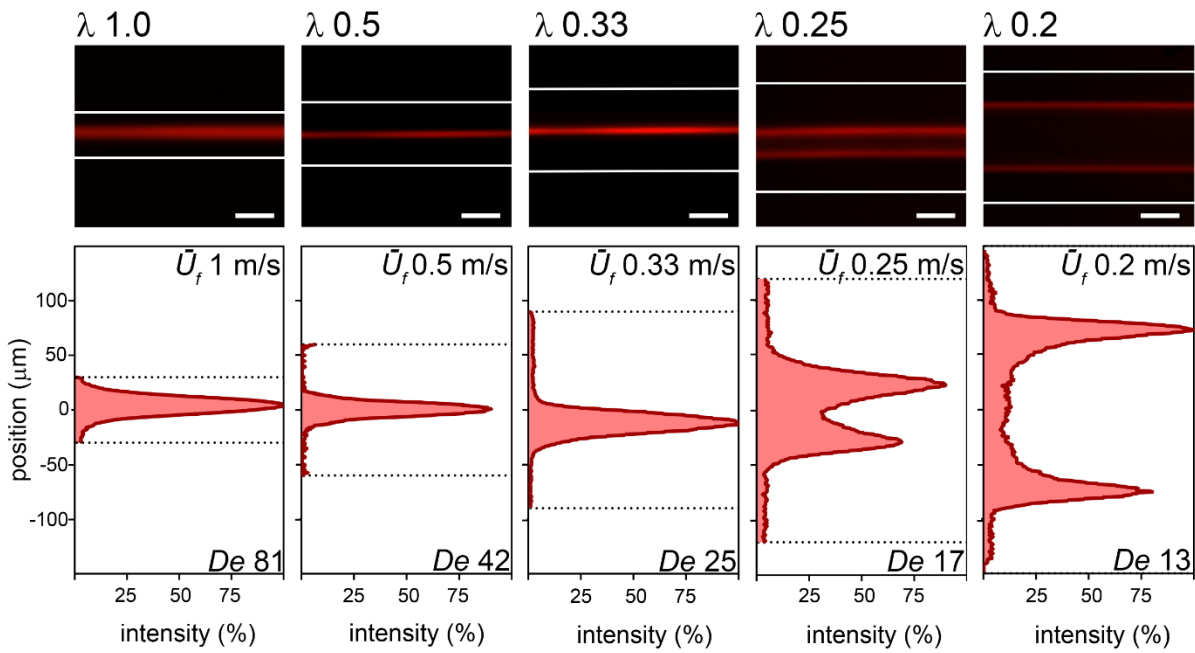


Figure 54. 15 μm fluorescent particles were aligned to a common position when they were transported within an incubation channel of the following aspect ratios: 1.0, 0.5 and 0.33. This indicated common velocity hence, common incubation time. Incubation channels with an aspect ratio of 0.25 and 0.2 were focused to two, mirrored positions. An aspect ratio of 0.2 provided reproducible, low velocity incubations. (Number of repeats = 3).

Flow rate ($\mu\text{L}/\text{min}$)	λ	Mean flow velocity (m/s)	Mean particle velocity (m/s)	CV (%)
231.5	1.0	1.0	1.47	3.3
231.5	0.50	0.50	0.76	0.7
231.5	0.33	0.33	0.45	1.3
231.5	0.25	0.25	0.3	5
231.5	0.20	0.20	0.24	3.7

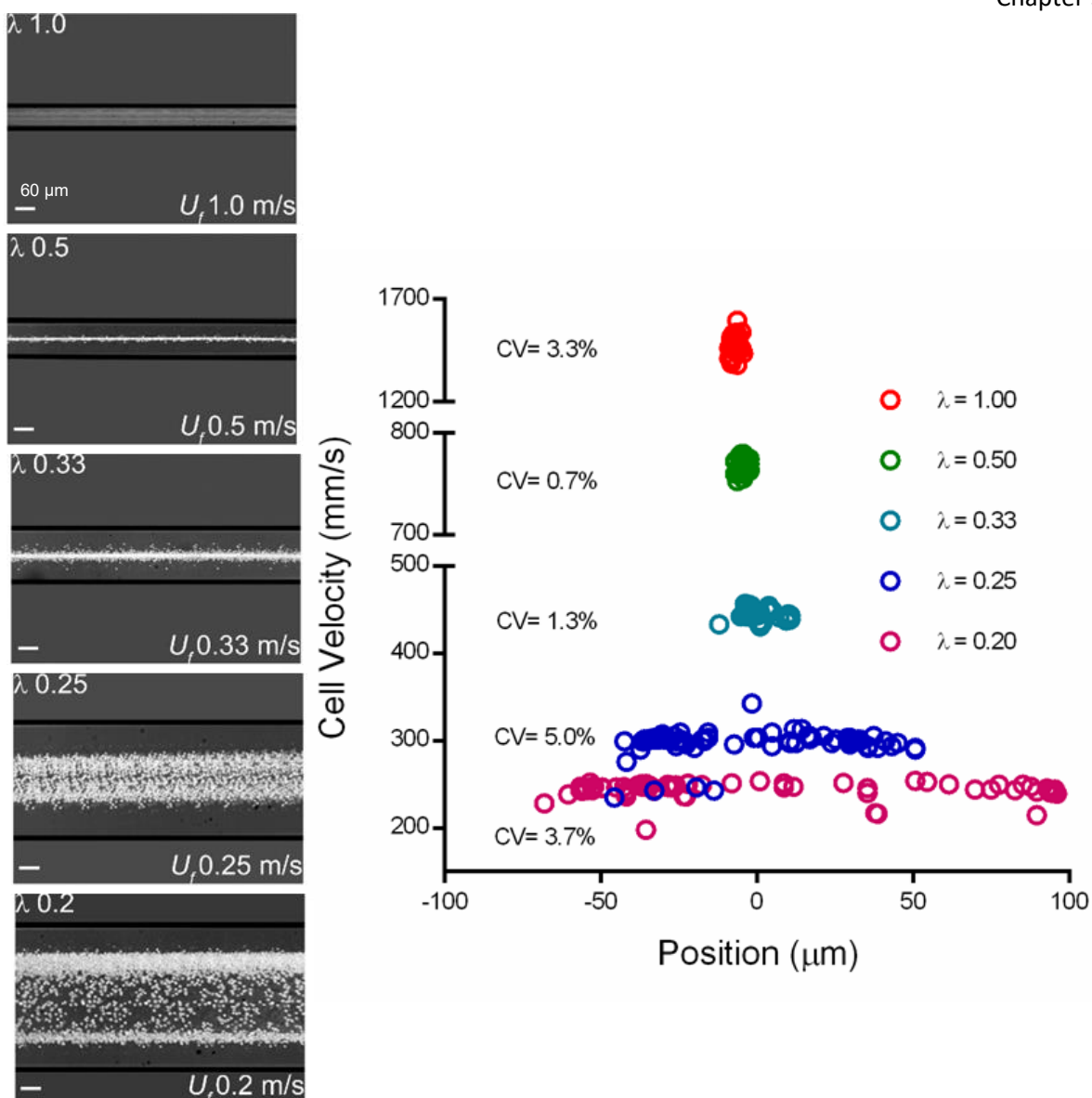


Figure 55. Low velocity transport and a channel ($\lambda = 0.25$) produced random positions with highly varied velocity (CV = 5%), whereas high velocity and an aspect ratio channel ($\lambda = 0.5$) focused the particles to provide uniform velocities (CV = 0.7%) and therefore uniform incubation times. Dean forces act and affect particles to reach equilibrium positions when they are transported within curved channel geometries. The magnitude of these secondary flows due to two counter rotating vortices at the bottom and top halves of the channel are velocity dependent. The position and velocity of 500 cells from each aspect ratio device was found using mtrackJ. (Number of repeats = 1).

3.8 Velocity and positional evolution before and after each curvature of the incubation channel

The evolution of the velocity and position of cells before and after each curvature of the incubation channels was further investigated in order to understand their influence on the incubation control (Figure 56). In an incubation channel with an aspect ratio (λ) of 1, cells were getting focused after $2\frac{1}{4}$ rotations. The coefficient variation (CV) of velocity was 3.7% and got gradually lower after few more rotations and the CV dropped to 2.7% (end point, Figure 57). An incubation channel with an aspect ratio of 0.5 allowed quicker alignment of cells to a single position. This was translated into uniform velocity and therefore, uniform incubation time. The cells required only a $1\frac{3}{4}$ rotation to achieve focusing to a single position with a coefficient variation of velocity 1.2% (Figure 57). At the end point of the channel the CV dropped to 0.9% (Figure 57). The cells in the incubation channel with an aspect ratio of 0.33 required $1\frac{3}{4}$ rotations in order to achieve uniform velocity with a CV= 2.7% (Figure 58). The CV looked relatively steady (<3%) before and after the following channel curvatures. At the end point, the CV dropped to 2.7% (Figure 58). Cells transported in an incubation channel with an aspect ratio 0.25 had a CV= 3.8% after $1\frac{3}{4}$ rotations (Figure 58). It is worth to mention that the coefficient variation of velocity remained steady (~4%) before and after each curvature of the incubation channel (Figure 58). In addition, cells transported in an incubation channel with an aspect ratio 0.20 had a coefficient variation of velocity 3.6% after $\frac{3}{4}$ rotations (Figure 59). When the cells reached the end point of the channel the coefficient variation of velocity dropped only marginally to 3.0% (Figure 59). This experiment was vital because it unravelled new information on the position and transport velocity of cells before and after the influence of a series of curved architecture elements in the microfluidic channels (Figure 60). This provided better understanding of this effect and was used for better incubation control of cells within the microfluidic devices.

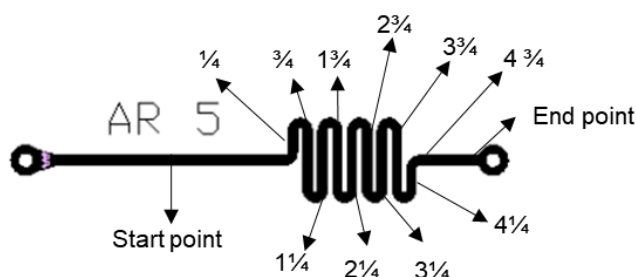


Figure 56. Incubation channel element with each curvature fraction labelled on the appropriate area.

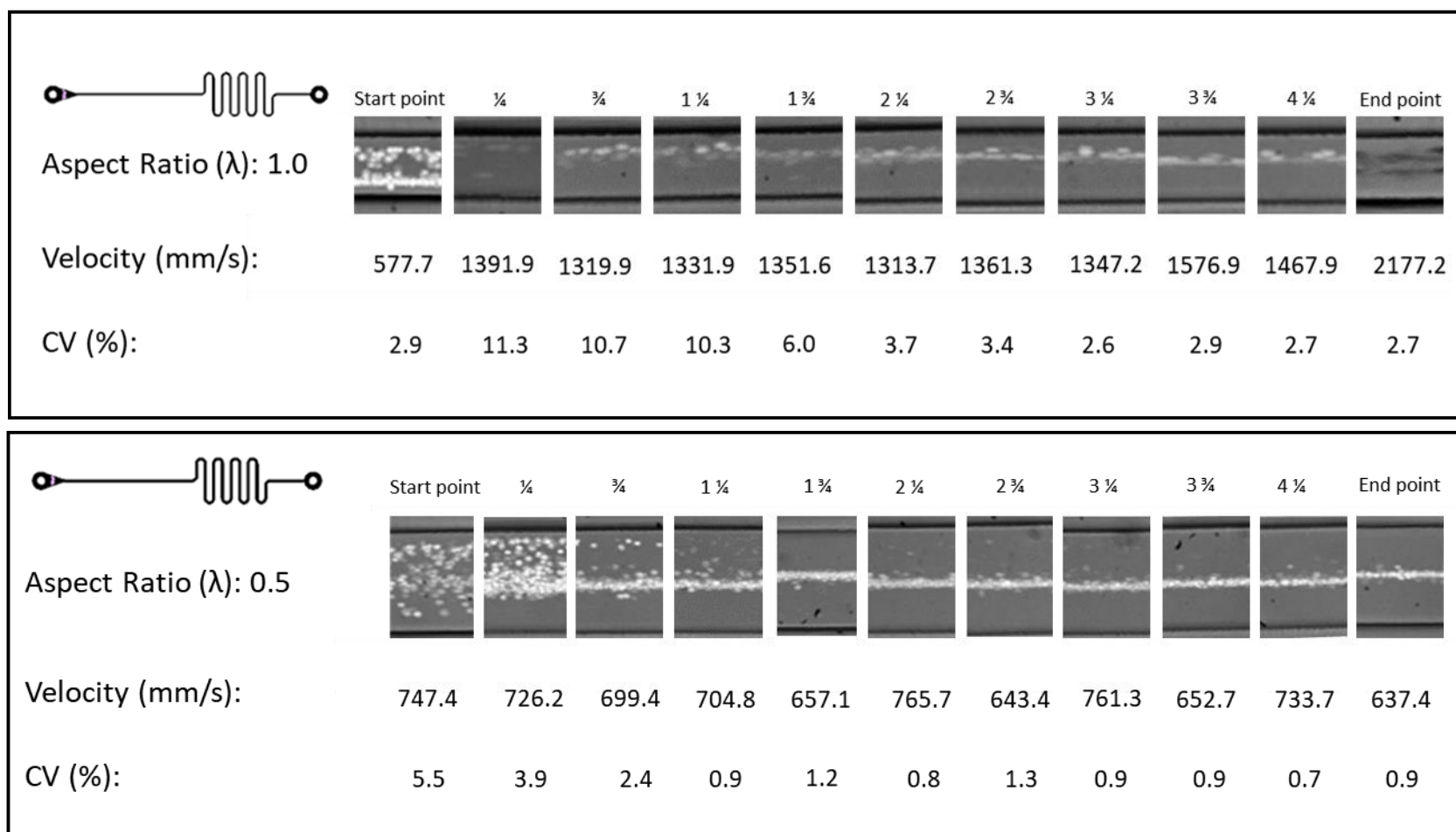


Figure 57. Positional and mean velocity evolution of cells before and after each curvature of the incubation channel. The incubation channels with an aspect ratio 1.0 and 0.5 improved cell transport to a single position. This was translated onto uniform velocity (low coefficient variation of velocity, 2.7% and 0.9%, respectively) and uniform incubation time (Cell number = 100 per video, Number of repeats = 1).

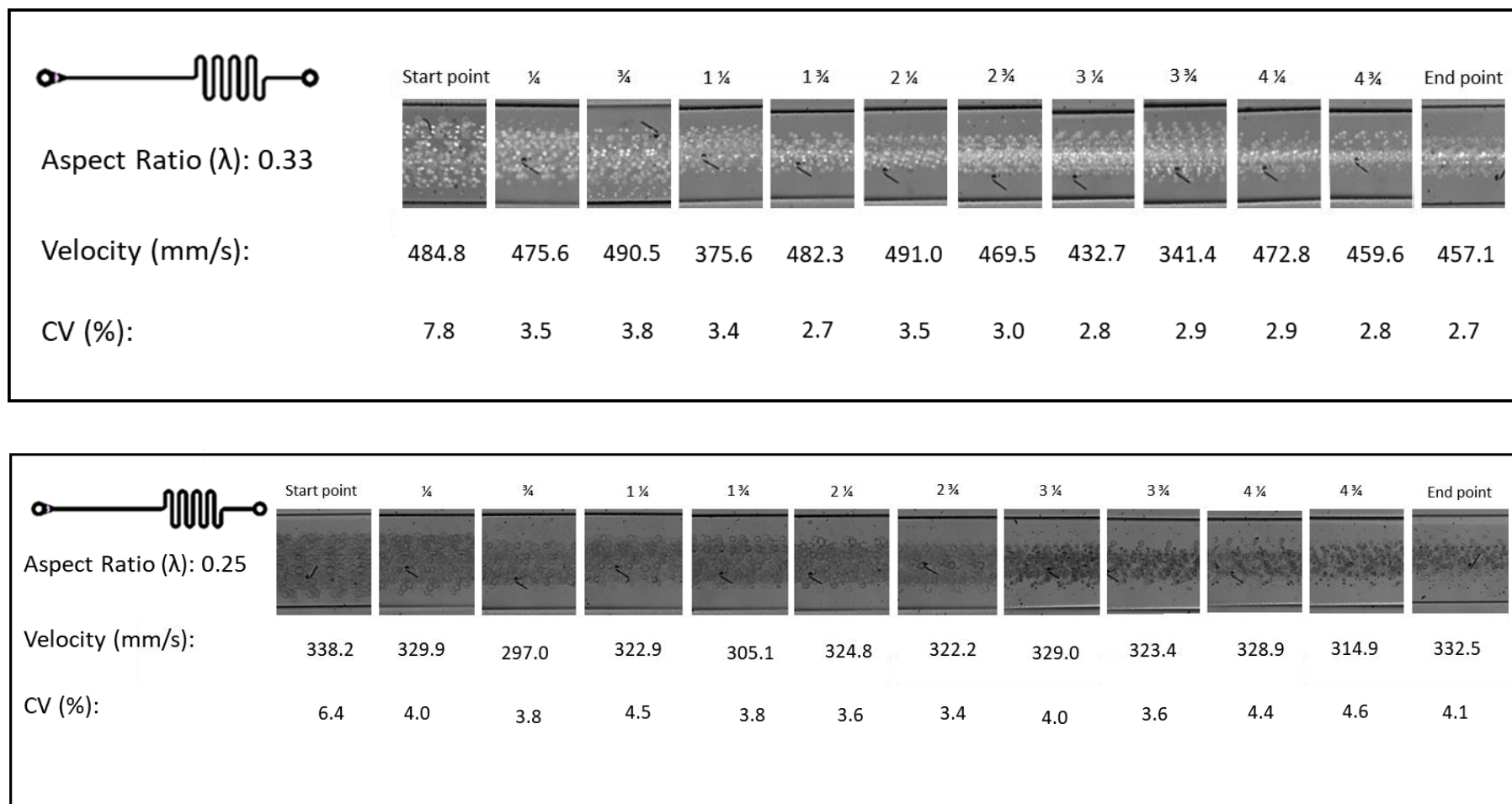


Figure 58. Cell position, mean cell velocity and coefficient variation (CV) before and after each curvature of the incubation channel. The incubation channels with an aspect ratio 0.33 and 0.25 had a coefficient variation of velocity 2.7% and 4.1%, respectively at the end point of the channel (Cell number = 100 per video, Number of repeats =1).

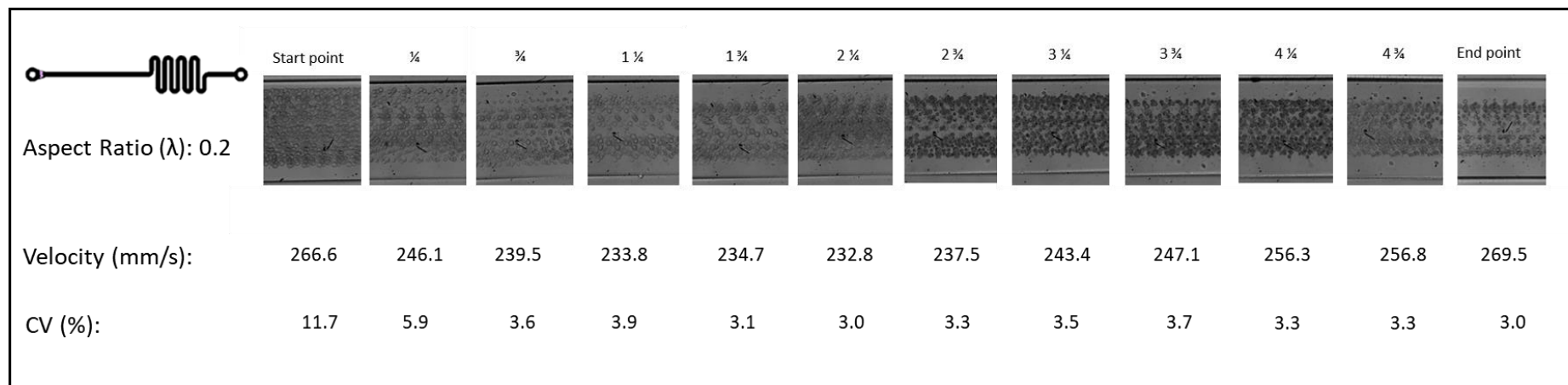


Figure 59. Cell position, mean cell velocity and coefficient variation (CV) before and after each curvature of the incubation channel. The incubation channel with an aspect ratio 0.2 had a coefficient variation of velocity 3.0 % at the end point of the channel (Cell number = 100 per video, Number of repeats =1).

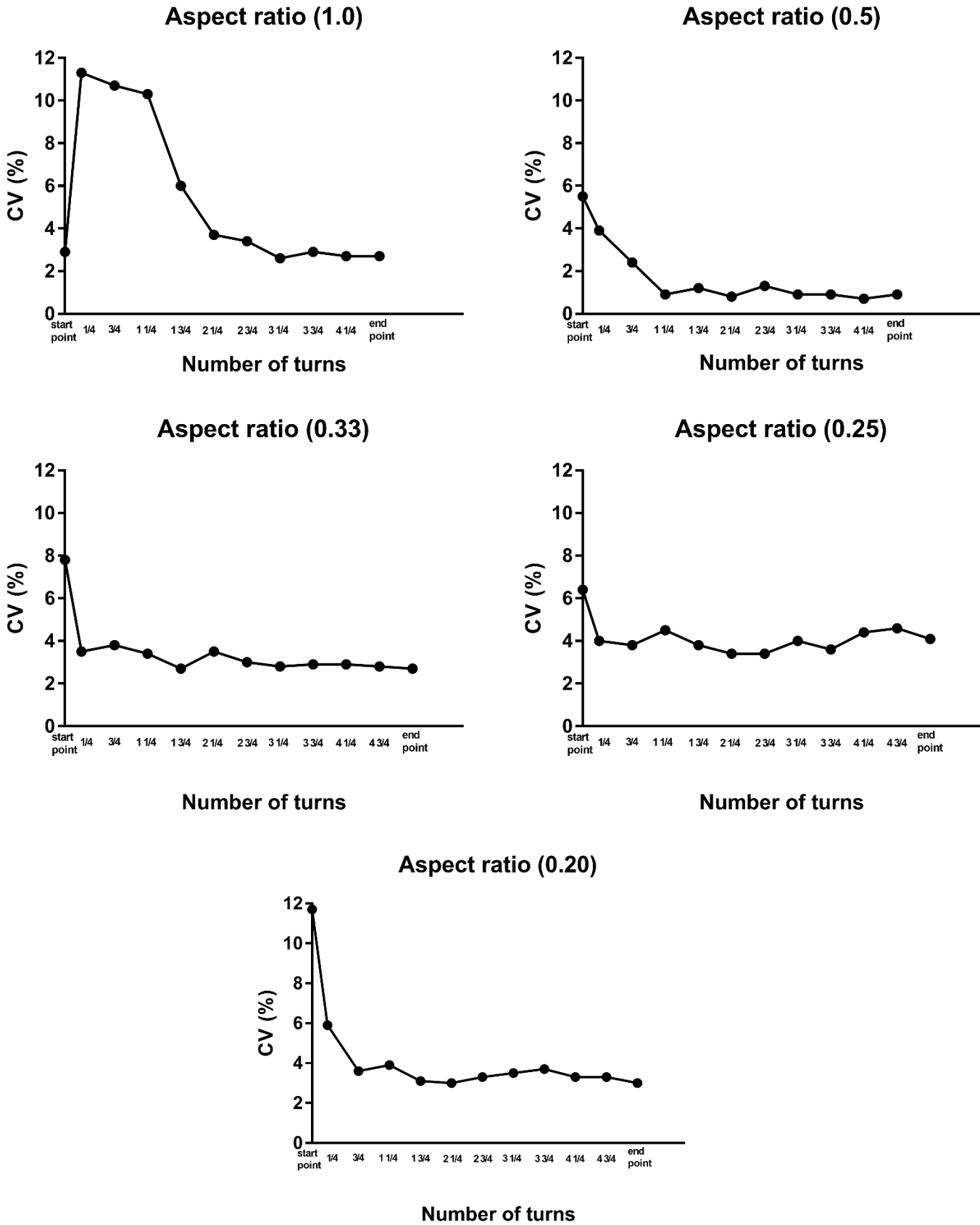


Figure 60. Plots show the coefficient variation of velocity in the areas before and after each curve (curve fractions) of the incubation channels that differ in aspect ratio.

The use of this effect allowed uniform incubation time control due to the uniform velocity of the cells. In the laminar flow regime characterized by high Reynolds number (Re) the inertial focusing rises because of a shear-gradient lift force due to the parabolic velocity profile combined with the wall-effect lift force that leads to focusing of particles to equilibrium positions (Figure 61 I).

The lift forces (F_L) are affected by the channel geometry and their effectiveness of transporting the particles is influenced by the fluid flow rate and the particle size.

The Dean secondary flow becomes stronger when the aspect ratio of the microfluidic channel becomes smaller. Dean flow gives rise to a drag force (F_D) on the particles. If the drag force is weaker compared to the lift forces, it will not affect the particle motion, however if the drag force is stronger than the lift forces it will cause particles to get trapped into the Dean vortices and they will rotate constantly (Figure 61 II).⁸²

It should be mentioned that the Dean flow after the curvatures becomes minimal and allows the lift forces to rise. These forces stop the continuous particle circulation (Figure 61 III) and it confines them in one single position in the channel (Figure 61 IV). This phenomenon was used as an advantage to achieve incubation control on the cells when they were focused to a single position in the incubation channel with uniform velocities ($CV \leq 3.7\%$) and therefore, to achieve uniform incubation times.

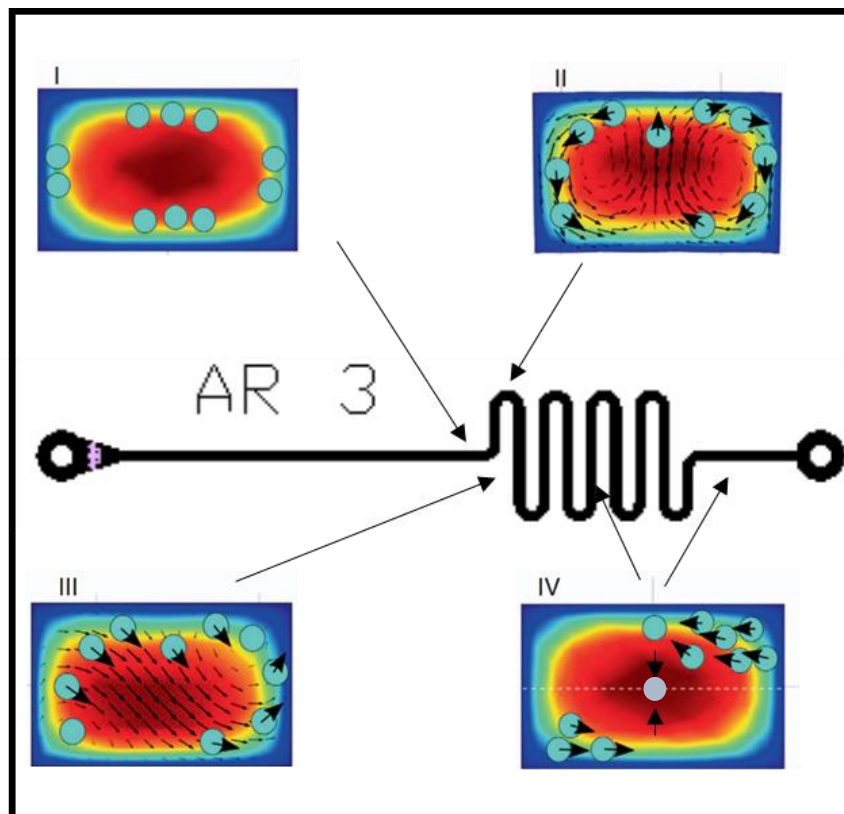


Figure 61. Evolution of the focusing positions of cells in a serpentine channel. The lift and shear-gradient forces due to the wall effect and the parabolic velocity profile, respectively transport the cells to the equilibrium positions of the channel (I). In a curved channel the drag force is stronger and transports the cells into Dean vortices where they rotate constantly (II). At the end of the curved channel the Dean force becomes weaker compared to the inertial forces and the cells stop rotating in the Dean vortices (III) and move onto one single position in the channel (IV). Adapted from Paiè *et al.*, 2017.⁸²

3.9 Validating microfluidic resistors for removing non-focussed cells

As mentioned in Chapter 2.1.3, the design of the fluidic resistors was one of the most important parts of the microfluidic circuit design. The fluidic resistors were based on serial and parallel flow (Kirchhoff's law) principles (Figure 62). Three different devices were designed based on different circuit interpretations in order to identify the correct one for use to achieve equal volume distribution from each outlet (Figure 62). The system was designed with 3 equal inputs enabling use of only a single parallel syringe pump. To ensure upstream and downstream inertial focusing for translation into ligand (EGF) and subsequently into quench buffer they had optimal (*i.e.* the same) switch conditions. There were 3 outputs (2 waste – not focussed cells – and one for double focussed cells, *i.e.* cells correctly switched into the ligand stream, incubated and correctly switched into the quench buffer stream). Data were reported as volumetric distributions normalised to unity. Perfect systems delivered equal outputs.

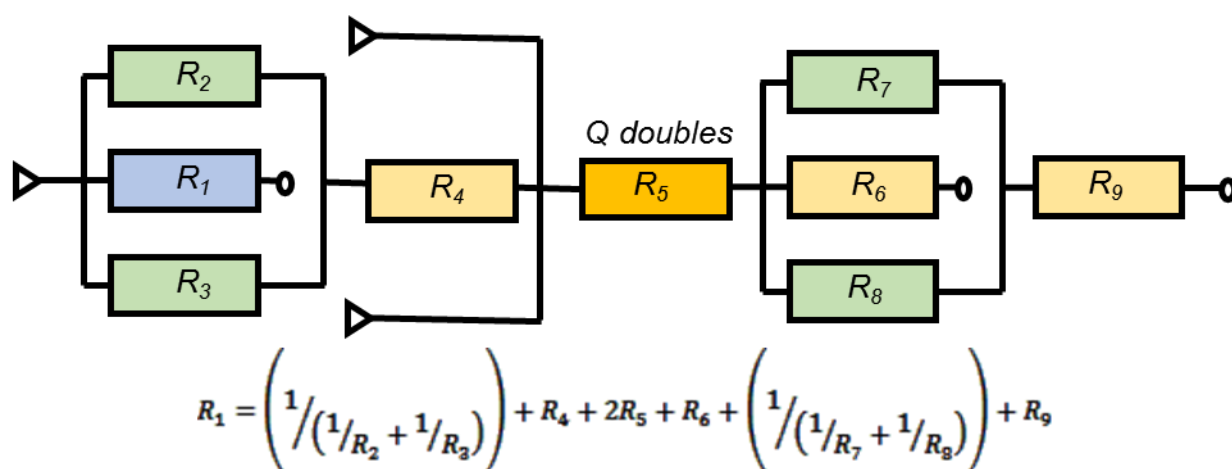


Figure 62. RV3 circuit resistor model provided near perfect flow bifurcation at the two rings of the structures. The flow rate doubles ($2R_5$) by the addition of the quench buffer. The parallel components (Kirchhoff) ($R_7 + R_8$) of the second ring structure were summed with the equal resistance cell outlet path (R_6).

The only difference between the three devices aside from the different aspect ratio and length incubation channels was the length of the spiral in the 1st outlet. A quick way to characterise the resistors was to flow water through the microfluidic circuit and check the volumetric distribution from each outlet. It was found that there was no equal volume distribution from the outlets of devices RV1 and RV2 (Figure 64). Device RV3 provided near perfect flow bifurcation at the two ring structures (Figure 64). The accurate, RV3 resistor model was characterized by flow rate (and therefore pressure) doubling by the addition of the quench buffer, as well as summing the parallel (Kirchhoff) components of the second ring structure with the equal resistance cell outlet path (see Chapter 2.1.3, Hydraulic resistance).

In addition, cells were transported within the device RV3, the samples from each outlet were collected and then processed through a flow cytometer to find the number of cells from each outlet. It was found that 2,388 cells (13%) were removed from the 1st outlet and 2,556 cells (14%) out of the 2nd outlet. The number of cells collected from the cell collection outlet was 13,113 cells (73%). This is an indication that 73% of the cells can be precisely stimulated and quenched within the microfluidic circuit.

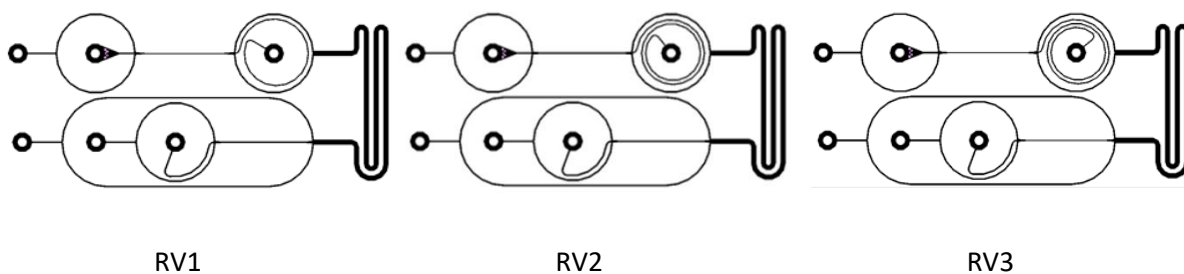


Figure 63. Outline of the microfluidic circuits (RV1, RV2, RV3) used for validating the microfluidic resistors by measuring the volumetric distributions from each outlet.

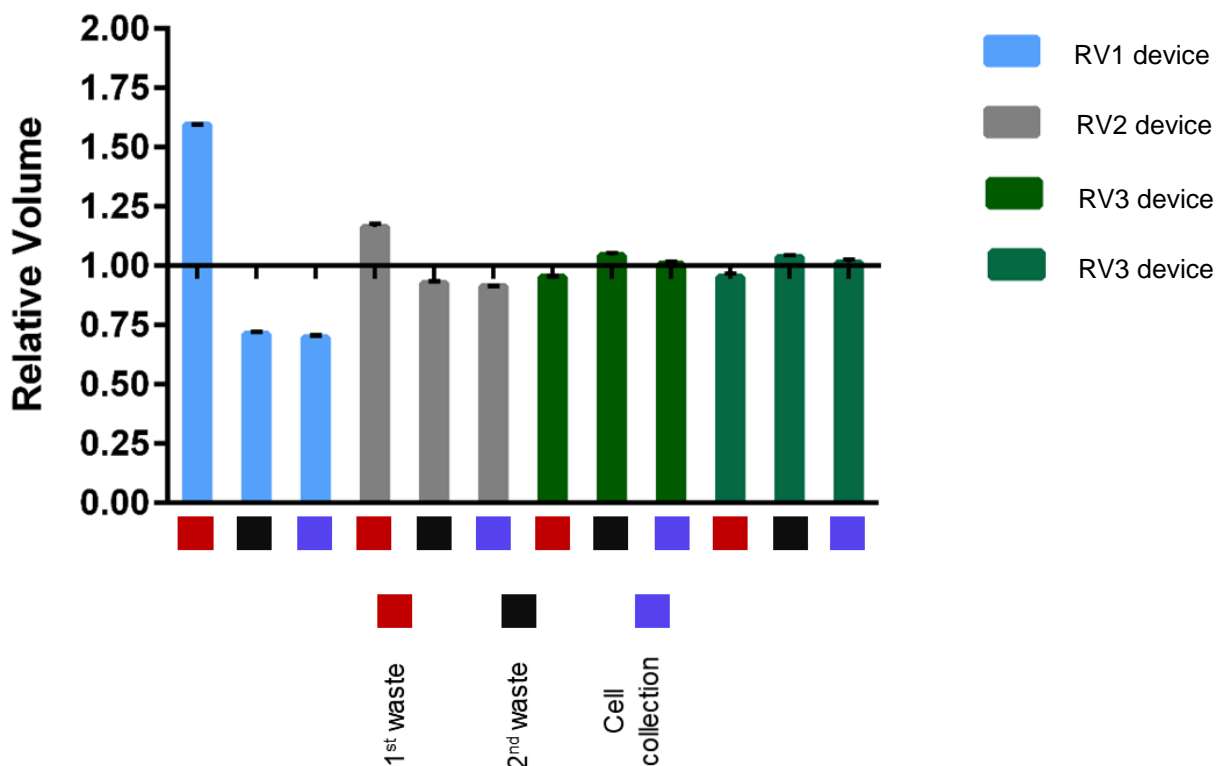


Figure 64. The relative volumetric distributions from the three outlets ($n=3$) of the three different devices was examined by measuring their mass (triplicates + SEM) and it was found that the optimal device (equal volume distribution from each outlet) was device V3 that was confirmed using a repeat experiment. (Number of repeats = 1 except RV3 device which it was run twice).

Based on the relative volumetric distribution data from the three different designs the RV3 resistor (Figure 64) was used in the design of the ‘time machine’ microfluidic devices version 2.0 (25 - 2000 ms). The 25 ms microfluidic device was designed to use an inertial focusing velocity of 4.0 m/s with a switch time of 0.5 ms. Subsequently, the ring velocity was 0.5 m/s with a ring time of 12.56 ms. In addition, the aspect ratio (λ) of the incubation channel was 1.0 and therefore, the incubation velocity was 1.47 m/s so the device was designed to have a length of 17.6 mm (Table 10). The 50, 75 and 100 ms microfluidic devices were designed in order to have the following characteristics: inertial focusing velocity of 4.0 m/s allowing a switch time of 0.5 ms with a ring velocity of 0.5 m/s and ring time of 12.56 ms. In addition, the incubation channel aspect ratio (λ) was 0.5 with an incubation velocity of 0.76 m/s. Based on these conditions the length of the devices (50, 75 and 100 ms) was 28.1, 47.1 and 66.1 mm, respectively (Table 10). The 250 ms microfluidic device had an inertial focusing velocity of 4.0 m/s with a switch time of 0.5 ms. The

ring velocity and the ring time was 0.5 m/s and 12.56 ms, respectively. The incubation channel aspect ratio (λ) was 0.2 with an incubation velocity of 0.24 m/s. The device was designed to have a length of 56.9 mm (Table 10). For the 500 and 750 ms microfluidic devices had an inertial focusing velocity of 1.0 m/s with a switch time of 2.0 ms. The ring velocity was 0.125 m/s with a ring time of 50.2 ms. The incubation channel was designed to have an aspect ratio (λ) of 0.2. The incubation velocity was 0.078 m/s. Therefore, the devices (500 and 750 ms) had a length of 34.9 and 54.4 mm, respectively (Table 10). The 1000, 1500 and 2000 ms were designed in order to use an inertial focusing velocity of 0.5 m/s with a switch time of 4.0 ms. The ring velocity was 0.0625 m/s with a ring time of 100.5 ms. The incubation channel was designed with an aspect ratio (λ) of 0.2 and an incubation velocity of 0.039 m/s. Subsequently, the devices were designed with a length of 34.9, 54.4 and 73.9 mm (Table 10). These numbers are tabulated below in table 10:

Table 10. Information on the velocity, switch time, aspect ratio and length of each microfluidic device. Longer cell incubation times require slower inertial focusing velocity.

Incubation Time (ms)	IF velocity (m/s)	Switch time (ms)	Ring velocity (m/s – $\lambda 1$)	Ring time (ms)	Incubation Channel λ	Incubation velocity (m/s)	Length (mm)
25	4.0	0.5	0.5	12.56	1	1.47 (1 $\frac{1}{4}$)	17.6
50	4.0	0.5	0.5	12.56	0.5	0.76 (1 $\frac{1}{4}$)	28.1
75	4.0	0.5	0.5	12.56	0.5	0.76 (1 $\frac{1}{4}$)	47.1
100	4.0	0.5	0.5	12.56	0.5	0.76 (1 $\frac{1}{4}$)	66.1
250	4.0	0.5	0.5	12.56	0.2	0.24 (2 $\frac{1}{4}$)	56.9
500	1.0	2.0	0.125	50.2	0.2	0.078 (2 $\frac{1}{4}$)	34.9
750	1.0	2.0	0.125	50.2	0.2	0.078 (2 $\frac{1}{4}$)	54.4
1000	0.5	4.0	0.0625	100.5	0.2	0.039 (2 $\frac{1}{4}$)	34.9
1500	0.5	4.0	0.0625	100.5	0.2	0.039 (2 $\frac{1}{4}$)	54.4
2000	0.5	4.0	0.0625	100.5	0.2	0.039 (2 $\frac{1}{4}$)	73.9

The newly designed microfluidic devices were validated by measuring the relative volumetric distribution from the three outlets (N=3) from three different devices of the same time point (e.g. 25 ms microfluidic device). The collected data (Figure 65 & 66) showed that the relative volumetric distributions from the 25 ms devices (N=3) were reproducible allowing incubation times (A time: 25 ms, B time: 29 ms, C time: 26 ms) (Figure 65). The incubation times obtained from the 50 ms device were the following: 46 ms, 47 ms and 36 ms (Figure 65). The 75 ms device incubation devices were: 68 ms, 73 ms and 76 ms (Figure 65). The 100 ms device allowed incubation times of 84 ms, 88 ms and 64 ms (Figure 65). The 250 ms devices were slower by 71 ms, 85 ms and 87 ms with incubation times of 321 ms, 337 ms and 335 ms (Figure 65). This device had a fundamental design error but it was used as the times are reproducible (~330 ms). The 500 ms devices allowed incubation times of 443 ms, 394 ms and 485 ms, respectively (Figure 65). The 750 ms devices allowed incubation times of 774 ms, 1347 ms and 650 ms (Figure 66). The incubation time (1347 ms) exceeded a lot the expected incubation time (~750 ms). This was due to contaminants (fibre and particulates) at the entrance of the channel that led to the first waste outlet. The 1000 ms devices were precise as they provided incubation times of ~1000 ms (1075 ms, 1068 ms and 1087 ms) (Figure 66). The 1500 ms and 2000 ms devices gave the following incubation times (1353 ms, 1426 ms, 1180 ms and 1873 ms, 1657 ms, 1601 ms, respectively, Figure 66). Some of the devices were not as precisely enough however, they were used for the experiments. The analytical equations (Chapter 2.1.3, Equation 7 & 8) were only an approximation therefore, it might be the source of the error observed. Generally, punch misplacement and contaminants such as fibres, particulates affect the relative volumetric distribution because they disrupt the resistors and the fluid flow. These have an impact on incubation velocity and the incubation time (Table 11).

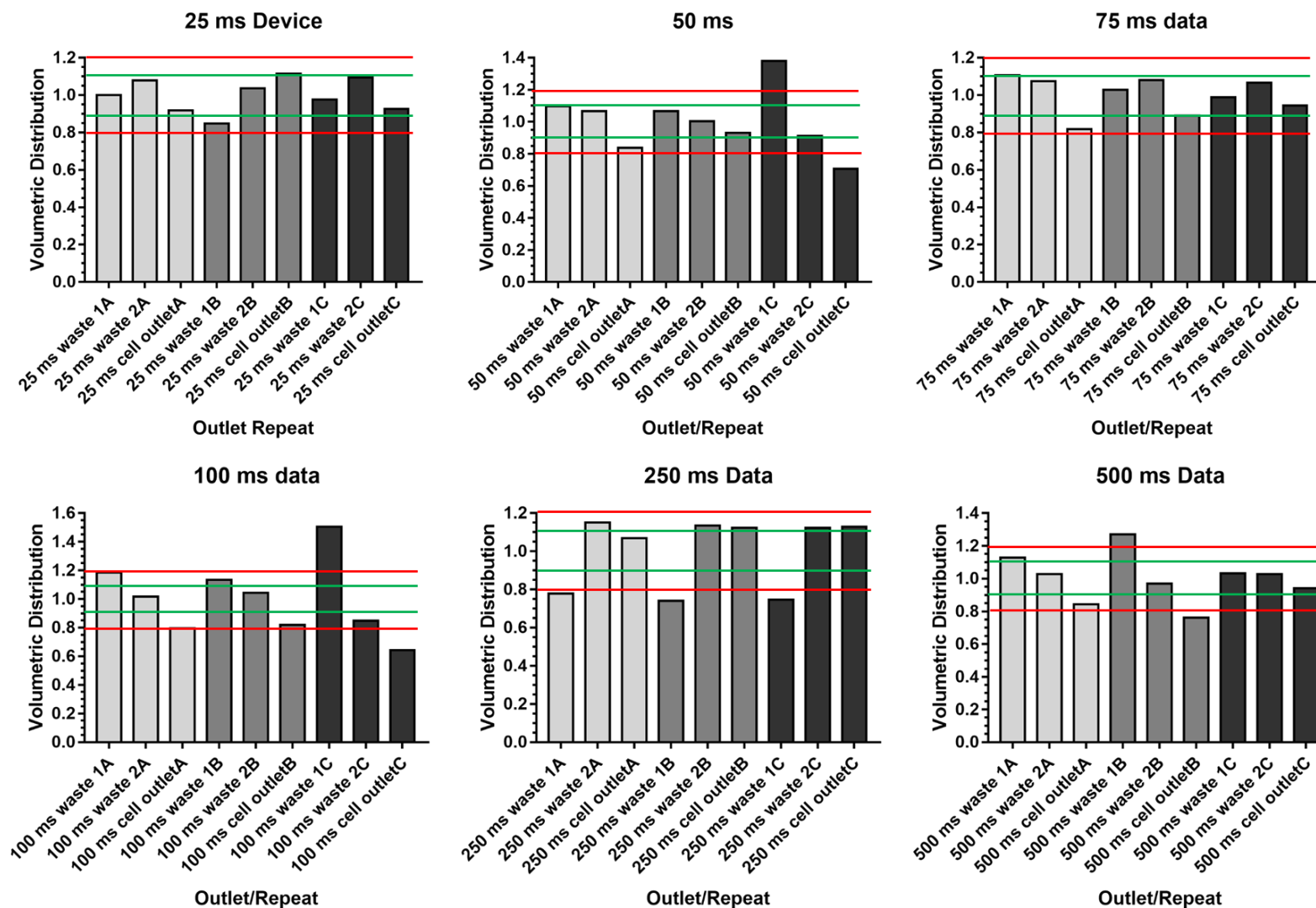


Figure 65. Relative volumetric distribution of the 25-500 ms devices ($N=3$) from each outlet. In general, the devices were operating within the limits (volumetric distribution) and the incubation times were reproducible. Some of the devices exceeded the expected times (incubation times were either shorter or longer) either due to punch misplacement or contaminants fibres or particulates. The red lines were used to indicate threshold for non-acceptable and green for $\pm 10\%$ performance (*i.e.* very good).

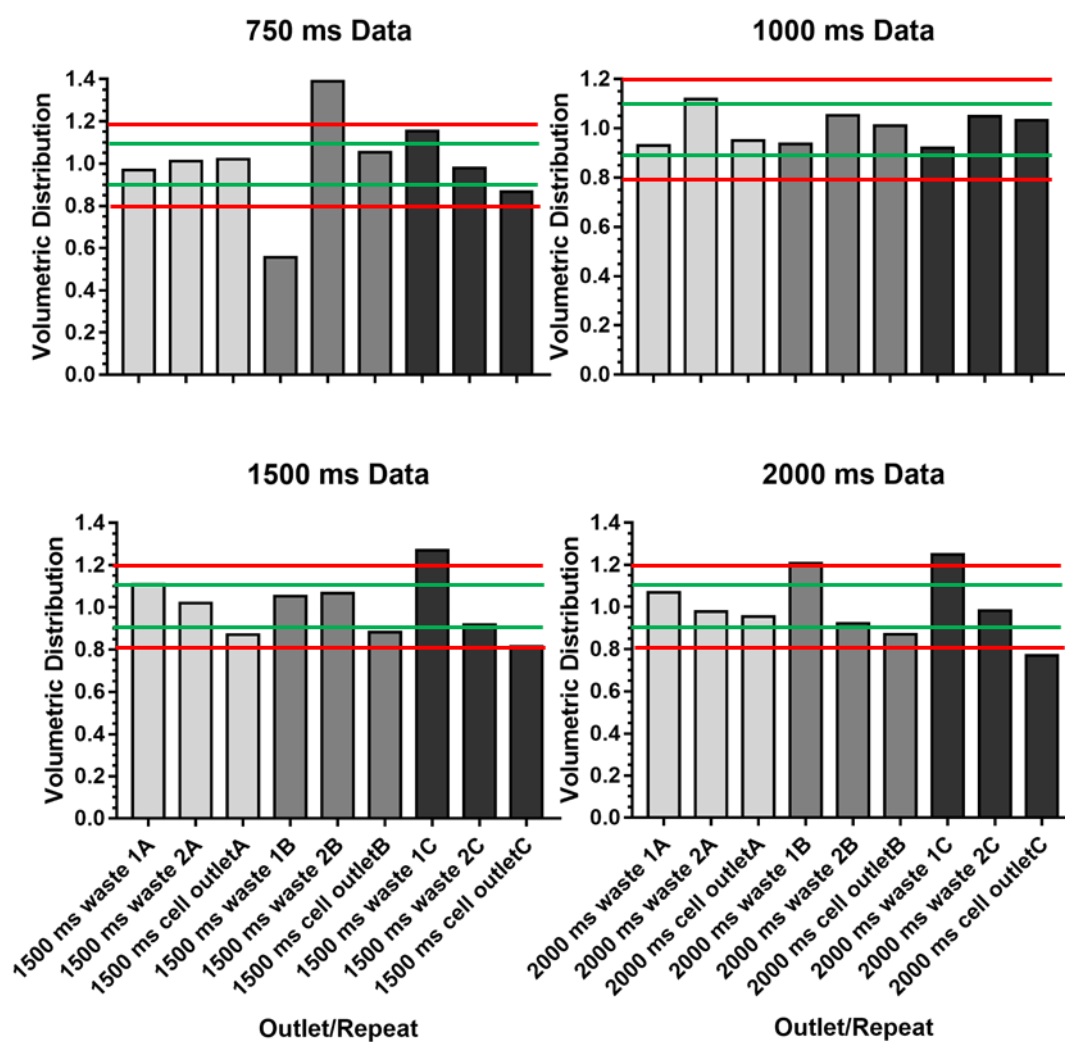


Figure 66. Relative volumetric distribution of the 750- 2000 ms devices ($N=3$) from each outlet. In general, the devices were operating within the limits (volumetric distribution) and the incubation times were reproducible. Some of the devices exceeded the parameters either due to punch misplacement or contaminants fibres or particulates. These devices were designed for an inertial focusing velocity input of 1 m/s for the 750 ms and 0.5 m/s for the 1000-2000 ms. The red lines were used to indicate threshold for non-acceptable and green for $\pm 10\%$ performance (*i.e.* very good).

Table 11. Incubation times obtained from three different microfluidic devices of each timepoint (25 ms-2000 ms). Red coloured text indicates the obtained incubation times which are >20% the above or below the timepoint of the device.

Incubation Times (ms)	Device A	Device B	Device C
25	25 ms	29 ms	26 ms
50	46 ms	47 ms	36 ms
75	68 ms	73 ms	76 ms
100	84 ms	88 ms	66 ms
250	321 ms	337 ms	335 ms
500	443 ms	394 ms	485 ms
750	774 ms	1347 ms	650 ms
1000	1,075 ms	1,068 ms	1,087 ms
1500	1,353 ms	1,426 ms	1,180 ms
2000	1,873 ms	1,657 ms	1,601 ms

3.10 Methanol based fixation causes air pocket formation and clogging of the microfluidic device

After the development of the complete circuit it was important to examine the behaviour of the cells, ligand and fixative in the microscale. Intracellular staining of phosphorylated tyrosine residues on the epidermal growth factor receptors involves cell membrane fixation to preserve the phosphorylation state of the proteins and allows cell permeabilization. Therefore, the use of Perm III, a methanol-based (methanol 83%) buffer was important. However, the use of pre-chilled methanol-based fixative in the device was not ideal because the area where the fixative flows led to clogging of the device. The most likely reason was the difference in temperature between the fixative ($-20\text{ }^{\circ}\text{C}$) and the cell buffer (room temperature) which led to the formation of air bubble due to the exothermic reaction that occurred and subsequently, the cells got trapped in the air pockets formed (Figure 67). The sudden warming was faster at these scales and caused dissolution of air from the methanol-based buffer. In addition, the clogging of the channel caused flow redirection and a larger volume was removed from the 1st waste outlet and therefore, higher number of cells. This was observed from the obtained volumetric distribution data (Figure 68).

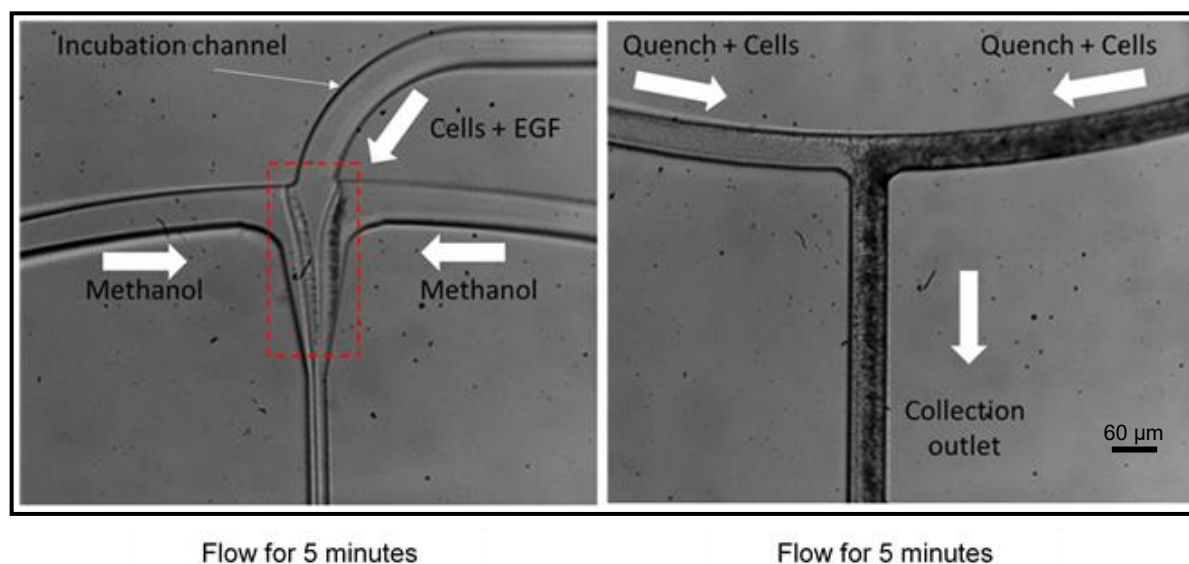


Figure 67. An immediate rise of the temperature (exothermic reaction) due to the mixing of a methanol-based fixative and cell buffer led to the formation of air pockets and clogging of the microfluidic device.

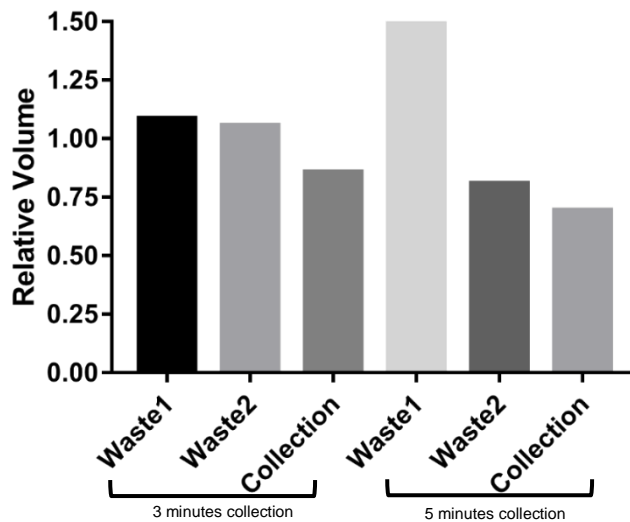


Figure 68. The volume from the waste outlets and the collection outlet was collected for 3 and 5 min. Stimulating cells and fixing them using the methanol based fixative for 3 min in the microfluidic device worked fine. However, using the device for 5 min showed that a higher volume was removed from the waste 1 compared to the other two outlets (waste 2 and cell collection.) (Number of repeats= 1).

The use of methanol (room temperature) decreased the air bubble accumulation but the problem persisted after 20 min of continuous flow as the microfluidic device clogged (Figure 69).

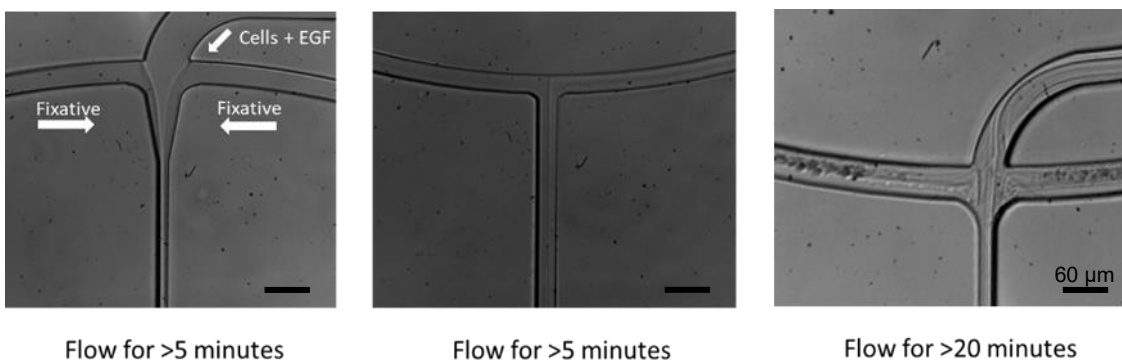


Figure 69. Room temperature methanol improved the device run time for >5 min however, 20 min of continuous flow caused clogging of the device. (Number of repeats = 1).

Therefore, it was decided to use 4% Paraformaldehyde (PFA) for on-chip cell fixation. It was clearly shown that the cells were transported in the inertial focusing and cell collection channels and the relative volumetric distribution from waste 1, waste 2 and cell collection outlet between 5 min and 30 min of continuous flow

showed that no significant changes occurred (Figure 70). Paraformaldehyde (4%) can be used at room temperature for cell quenching without any complications.

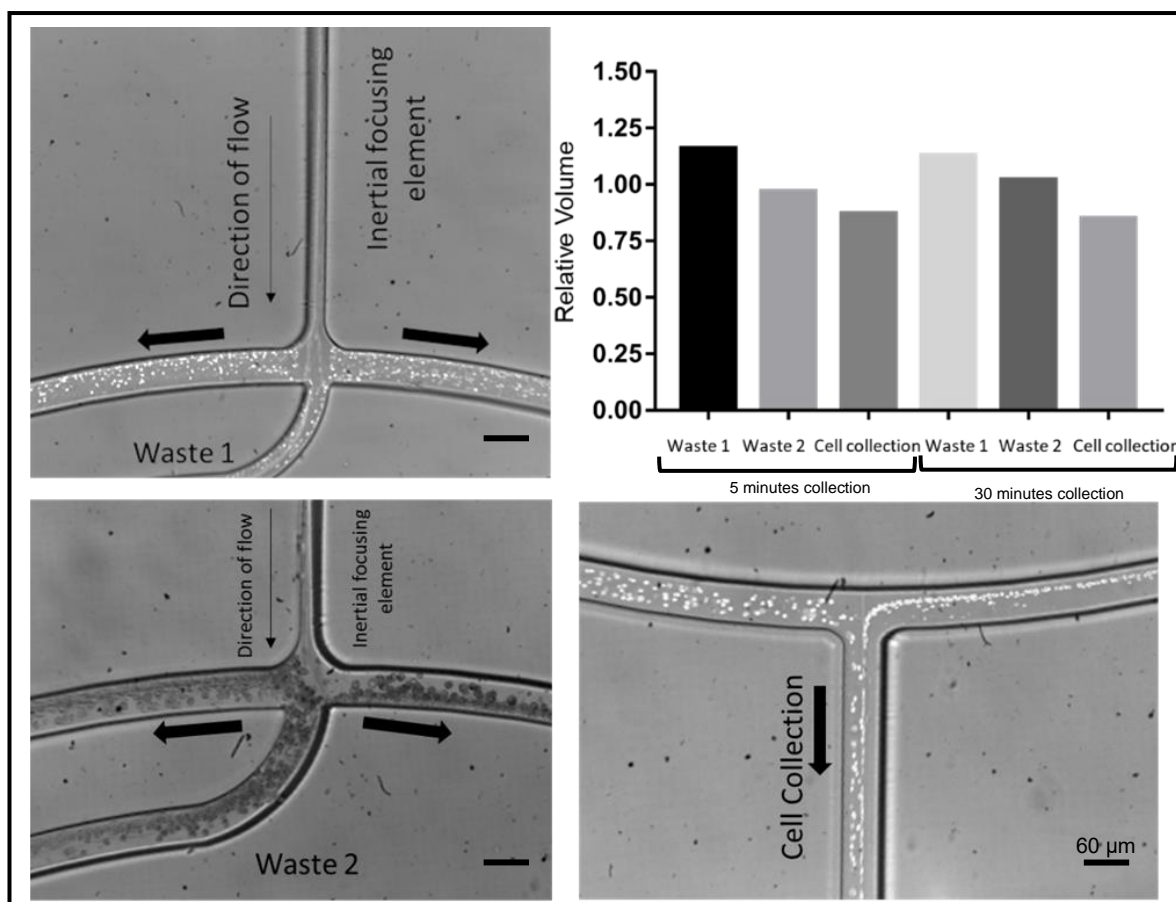


Figure 70. The use of room temperature paraformaldehyde (4%) allowed continuous flow for 5 min without clogging of the channel. The microfluidic device was still operational even with a 30 min continuous flow of cells. The relative volume from each outlet for the 5 min and 30 min of continuous flow showed no significant changes. This is an indication that the use of room temperature PFA (4%) did not clog the microfluidic device and it can be used for cell quenching. (Number of repeats = 1).

The implementation of different microfluidic elements allowed the development of a microfluidic device that can be used to achieve millisecond time points in order to investigate EGFR phosphorylation dynamics. To the best of our knowledge, this is the fastest single cell switching technology in existence and has great potential for studying EGFR activation dynamics as well as a host of other rapid cell surface processes. The next chapter (Chapter 4), includes a description of the challenges that have been encountered during the biological part of the project and the acquisition of the data.

4. Results on phosphorylation studies

4.1 Validation of antibodies by Western blot analysis

After the design, development and optimization of the microfluidic device the next step was to validate the specificity and sensitivity of the antibodies planned to be used with flow cytometry to temporally resolve the sequence of the phosphorylation events of the tyrosine residues found on the c-terminal tail of EGFR and also quantify the phosphorylation level of Y1068 and Y1173 using different concentrations of the ligand (EGF). Western blot analysis was chosen to be used as an alternative method for semi-quantification. A pilot experiment was performed following the Western blot methodology (Section 2.6). For this purpose, HeLa S3 cells were starved for 24 h in serum-free DMEM in order to synchronize them to the G1 phase of the cell cycle (Section 2.10). The cells were stimulated using the following EGF concentrations; 0 ng/mL, 1.5 ng/mL, 15 ng/mL and 150 ng/mL for 1 min and 2 min, respectively in order to quantify the level of phosphorylation of the Y1068 and Y1173 tyrosine residues. In addition, cells stimulated with different concentrations of EGF for 3 min were collected 45 min post-stimulation in order to examine the dephosphorylation rate of EGFR as an indication of receptor internalisation and recycling at this later time point. This experiment showed that stimulation of cells with a concentration as low as 1.5 ng/mL for 1 min was sufficient to cause phosphorylation of Y1068 and Y1173 (Figure 71A, 71B). The Western blot images (Figure 71A, 71B) showed that the phosphorylated tyrosine residues Y1068 and Y1173 can be semi-quantitatively detected using the primary antibodies and the overall Western blot protocol (Chapter 2.6). The PY20 antibody was used as a control as it is able to detect the global phosphorylation levels of tyrosine residues that occur in cells and allowing analysis of multiple downstream interaction partners following EGF stimulation (Figure 71C). Evaluating the results, it was confirmed that the antibodies were specific and sensitive and the different concentrations of the ligand (EGF) used in the experiment allowed to identify the concentration of the ligand needed to reach saturation levels of phosphorylation. These findings were of a significant value, thus, they were used to optimize our methodologies and accomplish the aims of the project.

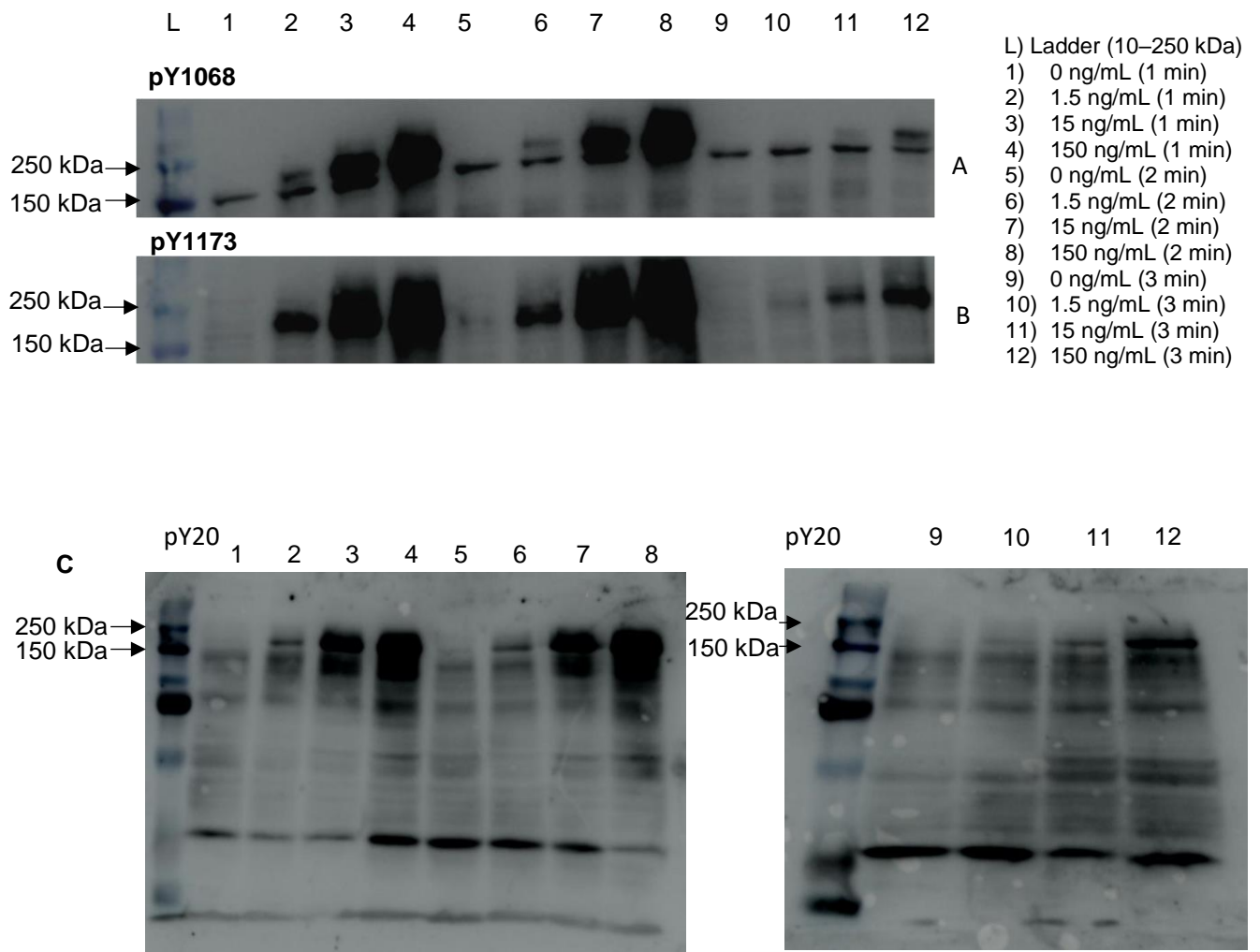


Figure 71. HeLa S3 cells were cultured in serum-free medium for 24 h and left untreated (Controls-lanes 1, 5 and 9) and treated with 1.5 ng/mL (lanes 2, 6 and 10), 15 ng/mL (lanes 3, 7 and 11) and 150 ng/mL (lanes 4, 8 and 12) before Western blot analysis for the EGFR tyrosine phosphorylation (A) pEGFR/pY1068, (B) pEGFR/pY1173) and (C) pY20 (total tyrosine phosphorylation). (Number of repeats =1).

The next experiment aimed to confirm if paraformaldehyde (PFA) fixed cells can be used in Western blot analysis after being treated with 1X sample buffer. This was essential because the cells collected from the microfluidic device need to be fixed in order to be able to study the phosphorylation of EGFR in sub second timescales. Therefore, HeLa S3 cells were cultured in DMEM (10% FBS, 1% Penicillin/Streptomycin) and then in serum-free media for 24 h. Adherent cells were stimulated with 100 ng/mL of EGF and collected using 1X sample buffer containing 1X protease and phosphatase inhibitors to prevent protein and phosphorylation degradation. In addition, negative controls (without EGF treatment) were collected for Western blot analysis. Western blot analysis of the collected samples clearly showed that 100 ng/mL of EGF is more than enough to stimulate the cells for 1 min and induce phosphorylation of the EGFR receptor (Y1173 and Y1068, Figure 72). The use of PY20 antibody (recognizes phosphotyrosine and phospho-tyrosine proteins) confirmed phosphorylation even after the PFA fixation (Figure 73). It should be mentioned that PFA fixation prior to the treatment with the sample buffer (1x) had better preservation of the phosphorylation states of tyrosine residues and this was observed by the bands that appear above 250 kDa (Figure 73).

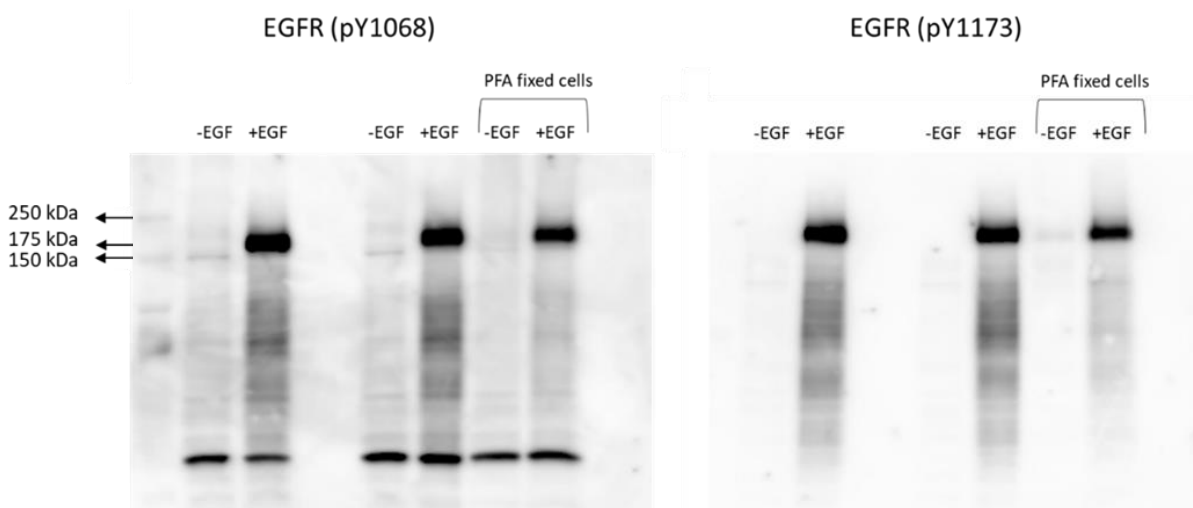


Figure 72. HeLa S3 cells were cultured in serum-free medium for 24 h and left untreated (-EGF) and with epidermal growth factor (+EGF). The treatment with 100 ng/mL of EGF for 1 min induced phosphorylation of pY1068 and pY1173 at the expected molecular weight (175 kDa). (Number of repeats =1).

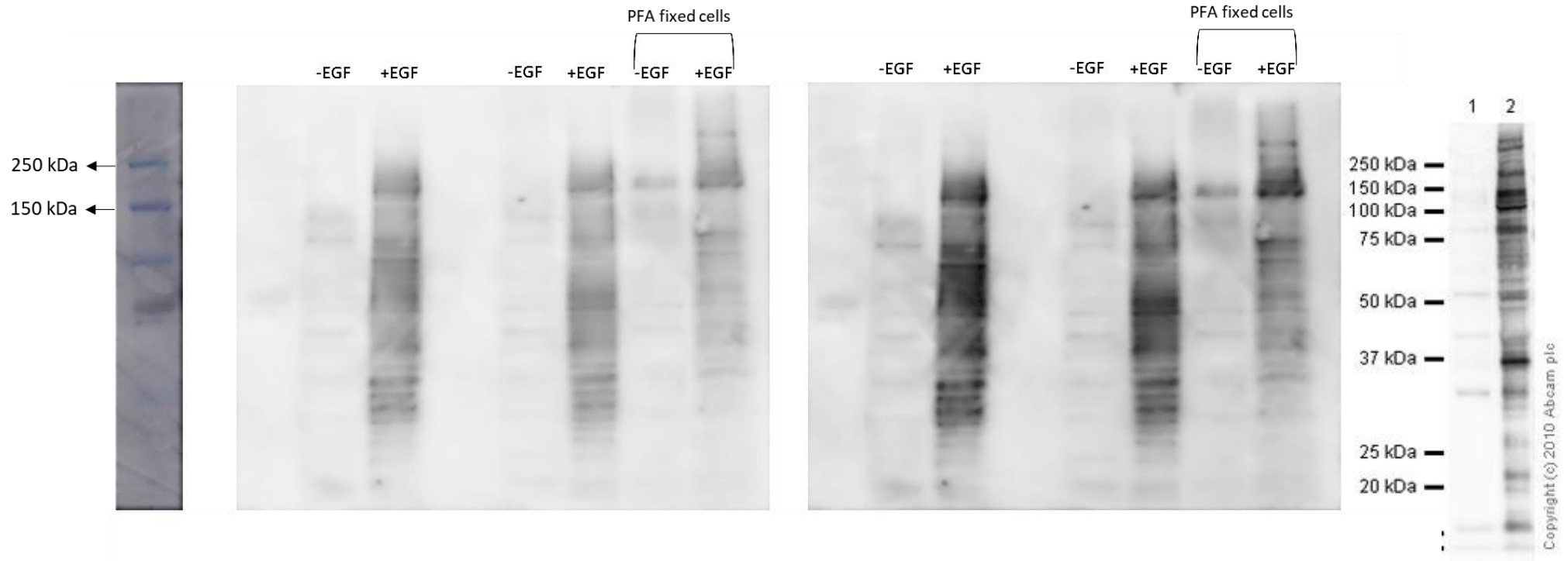


Figure 73. HeLa S3 cells were cultured in serum-free medium for 24 h and left untreated (-EGF) and with epidermal growth factor (+EGF). The treatment with 100 ng/mL of EGF for 1 min induced phosphorylation of proteins. PY20 mouse anti-phosphotyrosine antibody was used to recognize phosphotyrosine and phosphotyrosine-containing proteins. (Number of repeats = 1).

The findings from the previous experiments led to the optimization of the methodology for the Western blot analysis using PFA fixed cells. The next step was to collect cells from the microfluidic devices and perform Western blot analysis. In addition, cells in suspension and cells in adherent state were also stimulated with the ligand in order to verify whether the phosphorylation of cells differs according to their state (suspension or adherent). The same methodology (Chapter 2.6) was used to stimulate the cells (100 ng/mL of EGF) and negative controls (-EGF) were collected from the microfluidic devices (100 ms and 250 ms) and treated with sample buffer (1x) in order to be quantified with Western blot analysis. The signal of pY1068 from cells stimulated for 100 ms (+EGF) was not detectable with Western blot (Figure 74). On the other hand, the cells (+EGF) from the 250 ms device gave a low signal after the incubation with the pY1068 antibody. The staining with PY20 antibody (recognizes phospho-tyrosine and phospho-tyrosine proteins) which normally gave a high signal in the previous experiments with cells stimulate off the microfluidic chip, in this case gave a low signal from the cells stimulated with 100 ng/ml of EGF for 250 ms (Figure 75 & 76) but the cells stimulated off chip with 100 ng/mL for 1 s were characterized by increased phosphorylation levels of pY1068 and phospho-tyrosines (Figure 74 & 75). Furthermore, it should be mentioned that no difference was observed in the phosphorylation of cells when they were either in suspension or adherent state. Evaluating the obtained data, Western blot analysis was not ideal because of the weak/low signal. The low number of cells collected (200,000 cells compared to 1 million cells not microfluidically processed used for Western blot analysis) from the microfluidic devices and subsequently the low number of protein was the reason for this weak signal. However, the findings were of a great importance because they justified the need for using highly sensitive flow cytometric analysis.

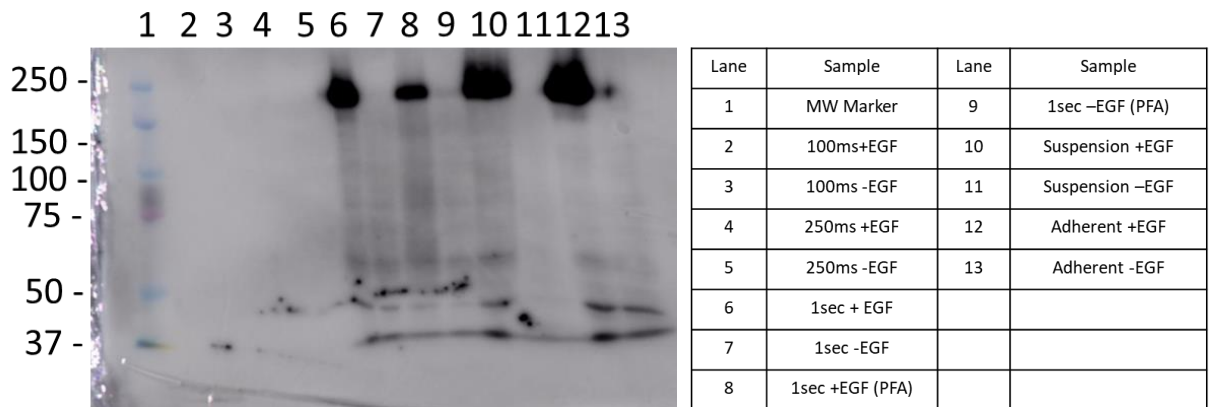


Figure 74. Western blot analysis of samples collected from HeLa S3 cells cultured in serum free media was performed. It was found that the protein concentration of the cells collected from the 100 ms and 250 ms devices was not sufficient thus, pY1068 was not observed. From the positive controls (1 second +EGF, 1 second +EGF + PFA, cells in suspension and adherent cells) protein bands were visible at the expected molecular weight (175kDa). (Number of repeats=1).

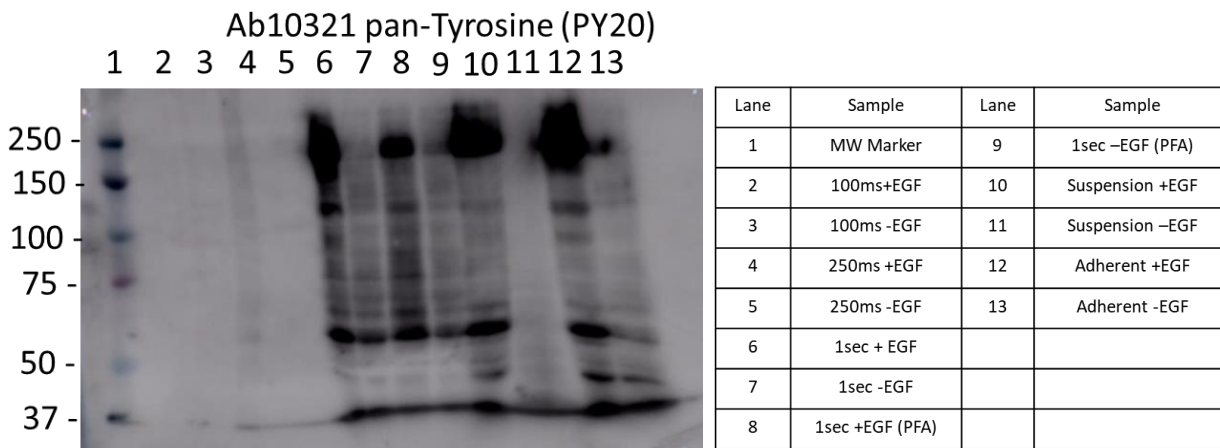


Figure 75. Western blot analysis of samples collected from HeLa S3 cells cultured in serum free media was performed. It was found that the protein concentration of the cells collected from the 100 ms and 250 ms devices was not sufficient thus, PY20 was not observed. From the positive controls (1 second +EGF, 1 s +EGF + PFA, cells in suspension and adherent cells) protein bands were visible at the right molecular weight (175kDa). (Number of repeats = 1).

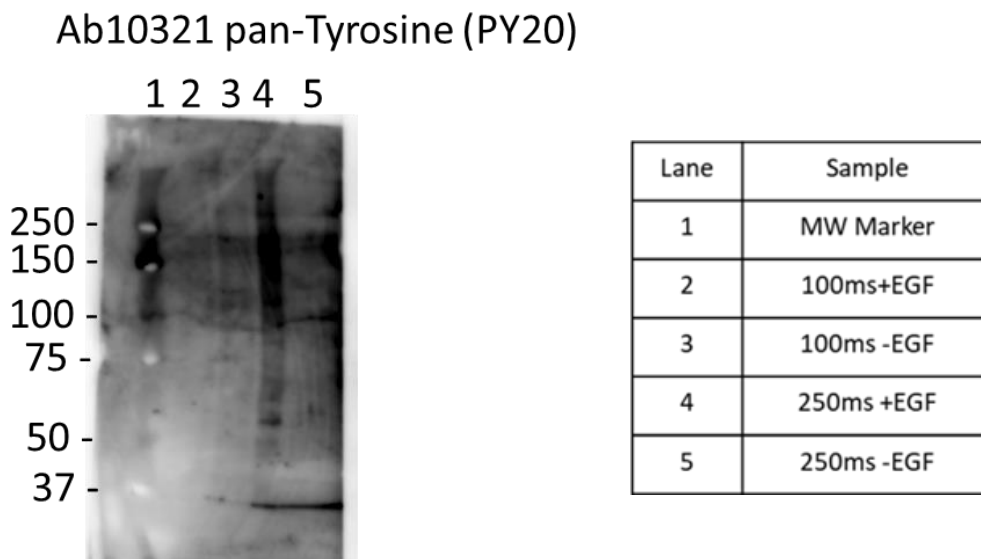
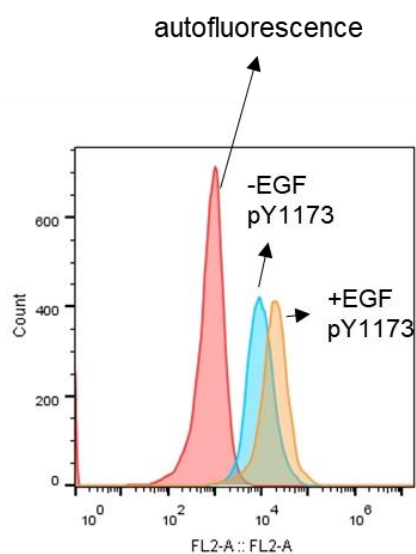


Figure 76. Western blot analysis of samples from 100 ms (+EGF) and 250 ms (+EGF) and their negative controls were collected from the microfluidic devices. It seems that there was a low concentration of protein due to the low number of cells. The cells from the 250 ms device gave a stronger signal compared to the other samples. These indicated a higher protein concentration in the sample however, the signal was not clear enough to visualise. (Number of repeats = 1).

4.2 Establishing a flow cytometry methodology for measuring EGFR phosphorylated tyrosine residues

A methodology for off-line analysis using flow cytometry was essential to rapidly derive statistically relevant data sets from single cells and also to multiplex the assay to correct for receptor density and to correlate multiple phosphorylated tyrosine analytes. For this purpose, in a pilot experiment, HeLa S3 cells were cultured in serum-free media, stimulated with EGF (100 ng/mL) for 1 min and then the cells were fixed and permeabilized. Intracellular staining was performed using a primary antibody conjugated with PE recognizing the phosphorylated Y1173 of EGFR (FACS methodology, Section 2.10). The samples were processed through an Accuri flow cytometer. Figure 77 shows that the stimulated cells had a significant positive signal (orange) for phosphorylated Y1173. On the other hand, the non-stimulated cells (control, blue) showed a negative signal as expected (Figure 77).



100 ng/mL EGF
1 minute stimulation

Figure 77. HeLa S3 cells were cultured in serum free DMEM media and stimulated with 100 ng/ml of EGF. The background levels of pY1173 phosphorylation were also measured (cells without EGF treatment). (Number of repeats =1).

After the initial experiment which showed increased EGFR phosphorylation, confirmatory experiments were performed. Thus, serum starved HeLa S3 cells were stimulated with 100 ng/ml of EGF for 10 s, 1 min and 5 min. Also negative control and auto-fluorescence data were collected. However, it was found that the median fluorescence intensity of the negative control was 12700 and the cells stimulated with 100 ng/ml of EGF for 10 s, 1 min and 5 min were 14,087, 14,128 and 14,822, respectively (Figure 78). In addition, one more experiment was performed in order to explain why there was no significant increase in the levels of phosphorylation after the stimulation with EGF (Figure 78). According to the literature, 100 ng/mL of EGF, is more than enough to obtain a significant increase in the phosphorylation levels of EGFR. It was found that the MFI of the serum starve HeLa S3 cells stimulated with 100 ng/ml of EGF and the MFI of the negative control (HeLa S3 without EGF) did not have much difference (2739 A.U. difference, Figure 78).

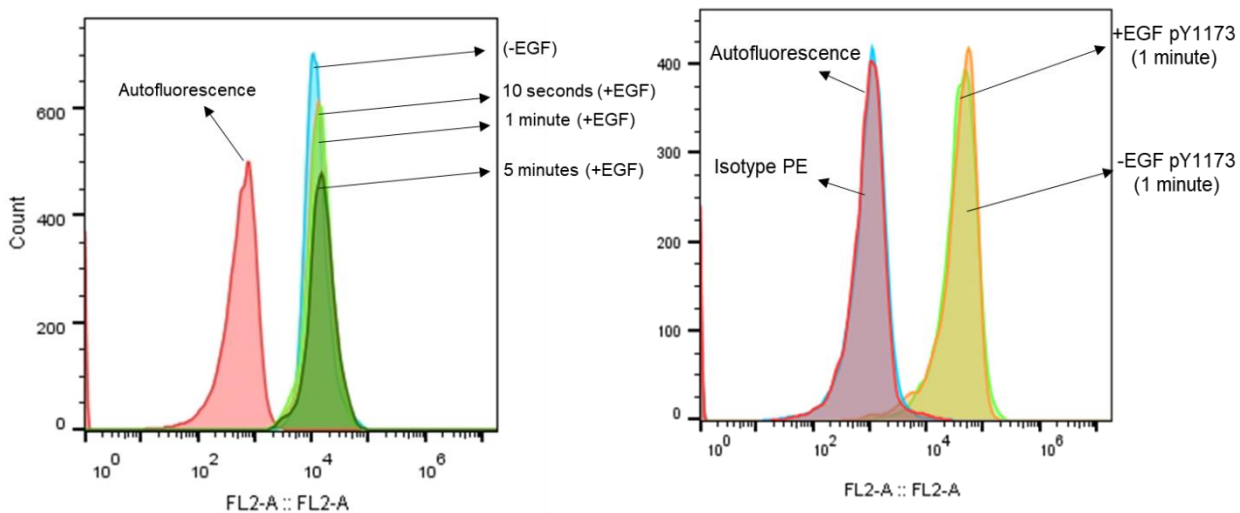


Figure 78. HeLa S3 cells were cultured in serum free DMEM and they were stimulated with 100 ng/ml for 3 different time points (10 sec, 1 min and 5 min). Cells were also collected to measure the auto-fluorescence and the background levels of phosphorylation (cells without EGF). It was found that there was no significant increase in the phosphorylation levels of pY1173 after the stimulation of cells with 100 ng/ml of EGF compared to the non-treated cells. HeLa S3 cells cultured in serum free DMEM and stimulated with 100 ng/ml for 1 min showed similar behaviour. (Number of repeats = 1).

Further investigation was required to identify the causes of this issue. Thus, the EGF aliquots and the EGF stock had to be checked. For this purpose, HeLa S3 cells (serum starved) were stimulated with 100ng/mL of EGF from the aliquots for 1 min. A negative control (-EGF) and autofluorescence control were also collected. It was found that the phosphorylation levels of pY1173 of the negative control and of the stimulated cells were overlapping (Figure 79). In addition, cells were also stimulated with 100 ng/mL of EGF from the EGF stock and it was found that there was no significant change in the phosphorylation levels of pY1173 compared to the non-stimulated cells (Figure 79). These observations led to the realization that the ligand (lyophilized powder) was not prepared in the right way and especially without keeping in mind the ligand adsorption. In the literature, it was found that adsorption of ligands to glass and plastic surfaces may affect the phosphorylation levels due to reduction of the ligands in an unpredictable way. A study by Jørgensen and colleagues in 1999 showed that EGF prepared in PBS (1x) and stored in polyethylene test tubes showed a significant adsorption to the test tubes.⁸³ After 20 min the EGF concentration was measured by ELISA and it was found to be reduced by 15-39%. After overnight storage at 4 °C the concentration was reduced even further (0-11%). On the other hand, EGF prepared in PBS (1x) with the presence of 0.1% human albumin as a carrier protein solved the adsorption issue in the test tubes made of polyethylene and polystyrene.

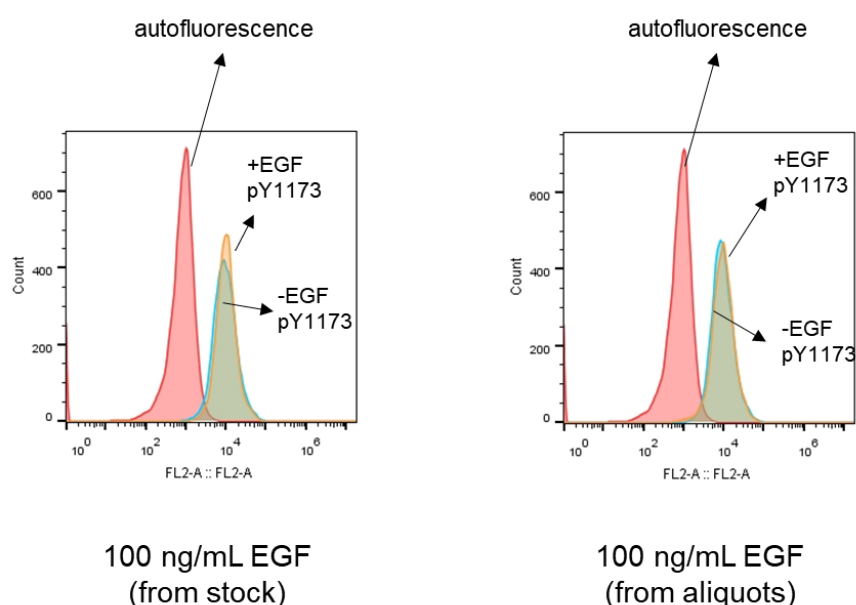


Figure 79. HeLa S3 cells were cultured in serum free media. They were stimulated with 100 ng/ml of EGF. The EGF used for this experiment was from the EGF stock and from the EGF aliquots. It was found that there was no significant increase in the phosphorylation levels of pY1173 EGFR after the stimulation of cells from either the stock or the aliquots. (Number of repeats = 1).

After considering ligand adsorption, a new stock of EGF was prepared from its lyophilized form. Bovine serum albumin (BSA) was used to prevent the EGF adsorption onto the polyethylene Eppendorf tubes in order to avoid the same phenomenon that was observed in the previous experiments. The effect of the new EGF stock on EGFR was tested on serum free HeLa S3 cells. It was found that the cells treated with the new stock of EGF had a 3-fold increase compared to the serum free HeLa S3 without EGF treatment (background phosphorylation levels). An additional experiment was performed using the new stock of EGF. Different concentrations of EGF were used to stimulate serum free cells at 21 °C and 37 °C and observed the phosphorylation changes that occurred due to EGF concentration and temperature. The stimulation of cells with 10 ng/mL, 25 ng/ml or 50 ng/ml of EGF caused a ~1.2-fold increase in the phosphorylation of pY1173 compared to the background levels (Figure 81). 100 ng/ml, 250 ng/ml, 500 ng/ml and 1000 ng/ml caused ~1.5-fold increase in the phosphorylation of pY1173 at room temperature (Figure 80).

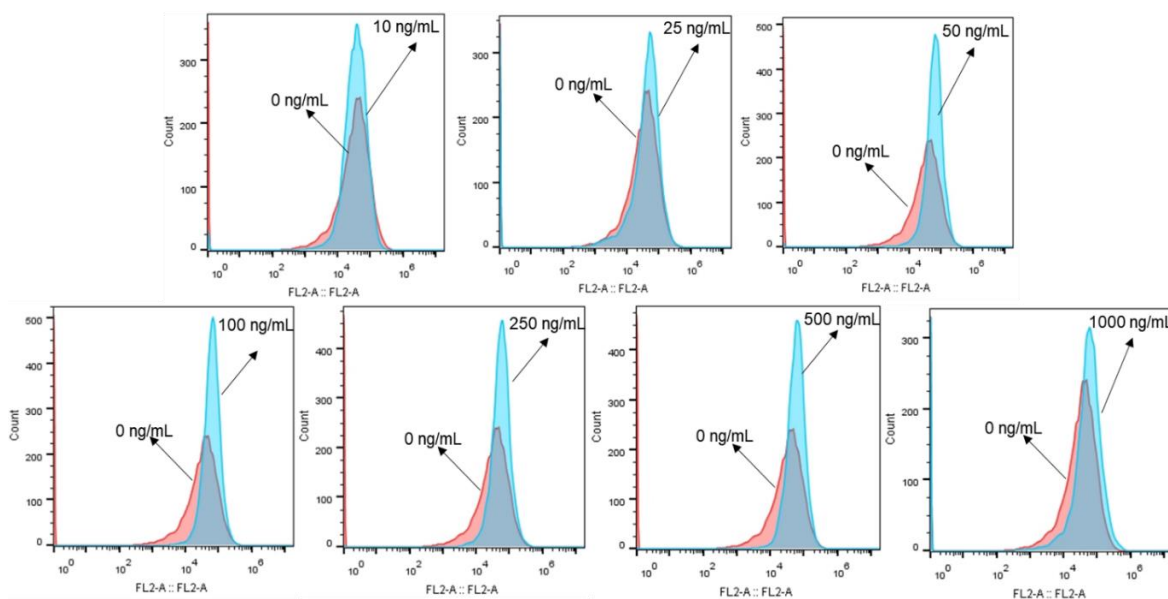


Figure 80. HeLa S3 cells were cultured in serum free media and stimulated with different concentrations of EGF at room temperature. 10 ng/mL, 25 ng/ml or 50 ng/ml of EGF caused a ~1.2-fold increase in the phosphorylation of pY1173 compared to the background levels. 100 ng/ml, 250 ng/ml, 500 ng/ml and 1000 ng/ml caused ~1.5-fold increase in the phosphorylation of pY1173. (Number of repeats = 1).

The HeLa S3 cells stimulated with 10 ng/ml and 25 ng/ml of EGF at 37 °C showed a 2-fold and 2.3-fold increase of phosphorylation of pY1173, respectively. 50 ng/ml and 100 ng/ml caused a 3.2-fold increase of pY1173. 250, 500, and 1000 ng/ml caused a ~3-fold increase of pY1173 (Figure 81). These observations showed clearly that the phosphorylation levels were significantly increased at 37 °C compared to the reactions that occur at room temperature (Figure 82). This occurs due to the fact that high temperature makes cell membrane more fluid compared to the low temperature that causes the fatty acid tails of the phospholipids to become more rigid and decreasing the overall fluidity of the membrane.⁸⁴ It should be mentioned that the concentration of EGF is sufficient to saturate the EGF receptor.

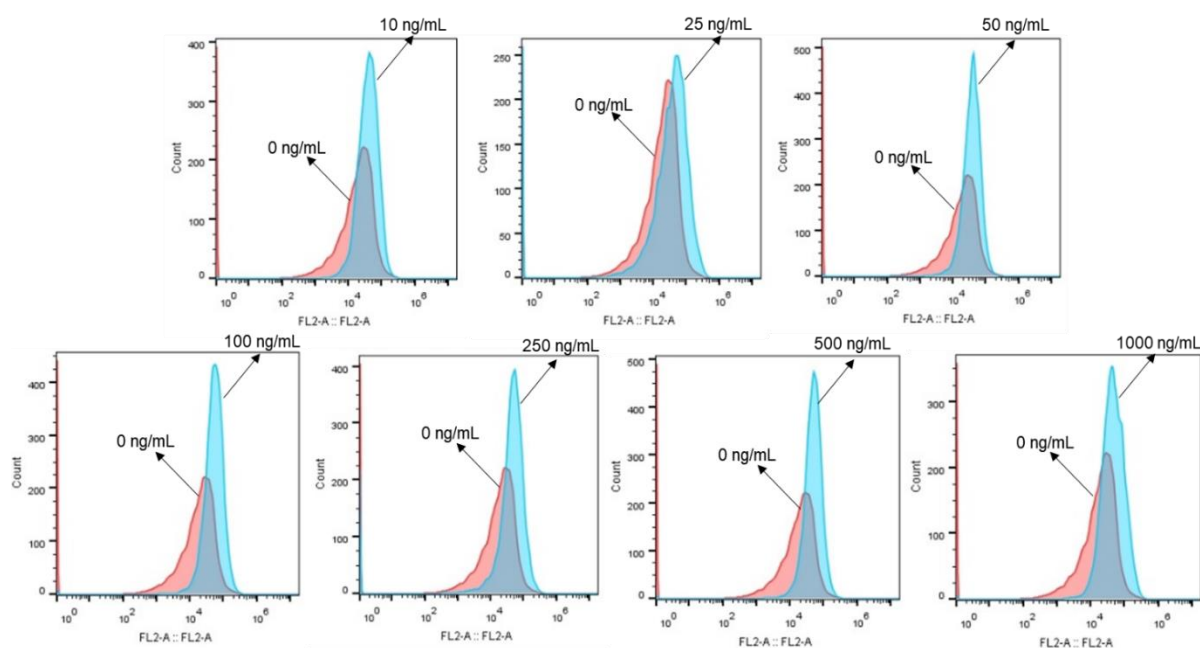


Figure 81. HeLa S3 cells were cultured in serum free media and stimulated with different concentrations of EGF at 37 °C. 10 ng/mL and 25ng/ml of EGF caused a 2-fold and .3-fold increase of pY1173 phosphorylation. 50 ng/ml and 100 ng/ml of EGF caused a 3.2-fold increase in the phosphorylation of pY1173 compared to the background levels. 250 ng/ml, 500 ng/ml and 1000 ng/ml caused ~3-fold increase in the phosphorylation of pY1173. (Number of repeats =1).

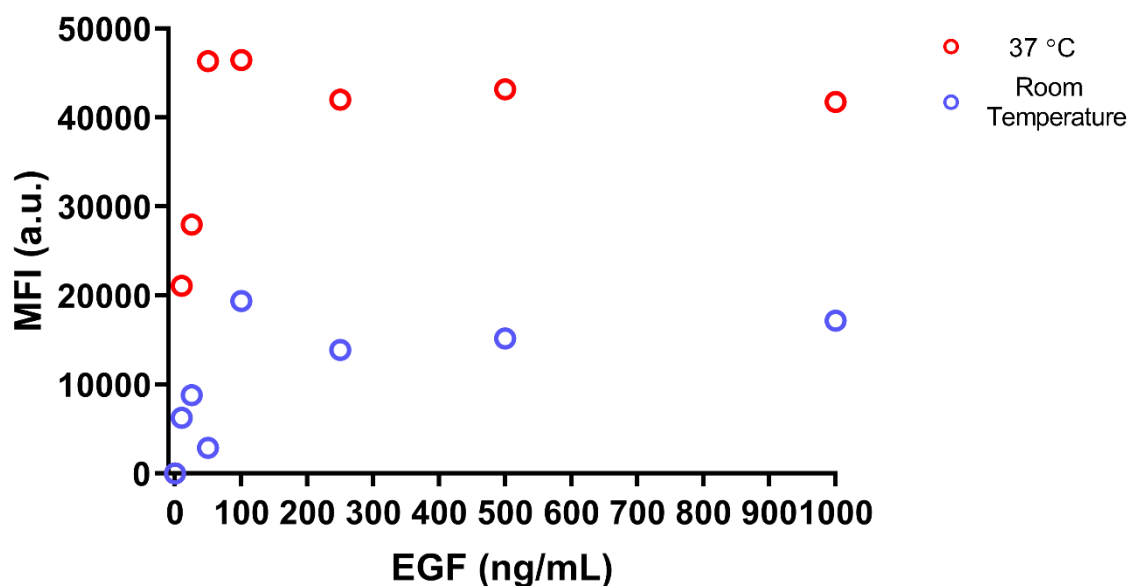


Figure 82. Median fluorescence intensity (MFI) of the phosphorylation levels of pY1173 EGFR responding to different EGF concentrations (10-100 ng/ml) in two different temperature conditions (room temperature and 37 °C). Results are expressed as the average median fluorescence intensity (MFI) values from the analysis of 10,000 cells with flow cytometry for each EGF concentration. The cells stimulated with different concentrations of EGF at 37 °C show higher levels of phosphorylation of pY1173 compared to the cells stimulated at room temperature. (Number of repeats =1).

The data obtained from this experiment clearly showed that the stimulation of cells should be performed at 37 °C due to the higher levels of phosphorylation compared to room temperature (Figure 82). However, it was not feasible to operate and maintain the reactions at 37 °C within the microfluidic devices due to the lack of the temperature control. The thermal stage of the microscope (Olympus Lifescience IX70 fluorescence microscope) was great for maintaining 37 °C. However, the use of thermal packs to maintain a 37 °C on the syringes that contained the EGF and the cells were not ideal. The temperature instability caused formation of air bubbles within the microfluidic channels, indicating that while the stage was at 37 °C the microfluidic device was at a lower temperature resulting in degassing. Therefore, the next experiments were performed at room temperature to avoid any issues with air pocket formation due to inability to stabilize the temperature at 37 °C.

4.3 Investigating EGFR phosphorylation levels in the sub-second time window

The knowledge obtained during this project was used to develop, optimize and finalize the methodology (Section 2.10) in order to accomplish the main goals of our research: a) confirm that the use of microfluidic device is capable to stimulate and preserve the phosphorylation levels of EGFR and b) study the sequence of the phosphorylation events that occur in the milliseconds time window. For this purpose, HeLa S3 cells were stimulated with EGF (100 ng/mL) and rapidly quenched within the microfluidic devices to arrest phosphorylation and preserve reaction intermediates. Three different devices were used in order to study three different time points (25, 50 and 100 ms). The collected cells were permeabilized and stained with three different primary antibodies conjugated with fluorophores (EGFR-FITC, pY1173-PE and pY1068-APC). Flow cell cytometry was used for high throughput multiplex analysis to collect data in a short time. It was found that 100 ng/mL of EGF stimulated the EGFR and caused a relative increase of the phosphorylation of Y1173 for the following time points: 25, 50 and 100 ms (Figure 83). Negative control was also collected in order to compare the baseline phosphorylation levels of the non-stimulated cells with the stimulated cells (Figure 83). The data were of a great significance because it was the first time to achieve and preserve sub second phosphorylation for three different time points.

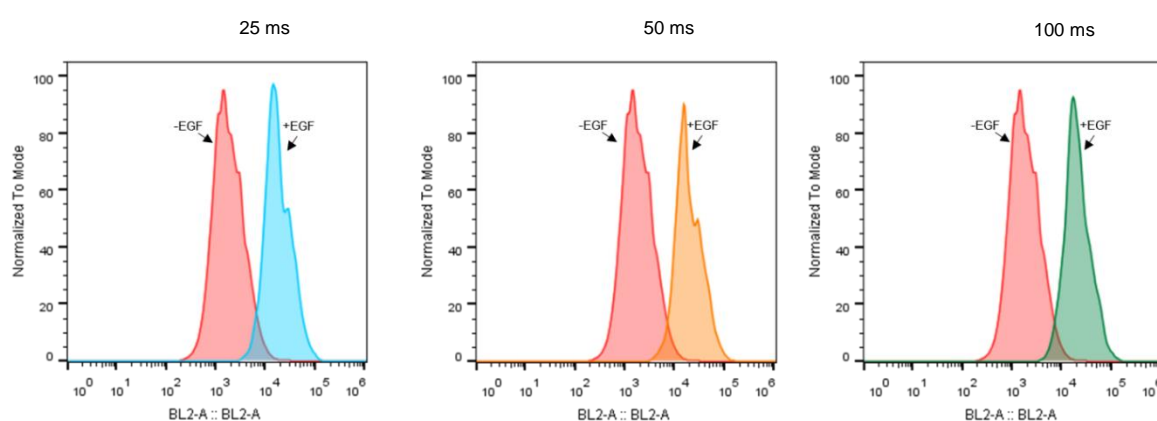


Figure 83. FACS histograms were characterizing the phosphorylation levels of pY1173 in HeLa S3 cells. A relative increase of phosphorylation levels at Y1173 when the cells were stimulated with 100 ng/mL of EGF for 25, 50 and 100 ms within the microfluidic devices compared to the non-stimulated cells (baseline phosphorylation) was indicated by the shift. (Number of repeats = 1).

It was found that there was a difference between the baseline phosphorylation of the cells (negative control) collected from the microfluidic device compared to the cells stimulated with the EGF for the designated time (25, 50, 100 ms) (Figure 84). The baseline phosphorylation had an M.F.I. of 2,269 (A.U.) The M.F.I. values of the pY1173 from the stimulated cells were ~ 10 times higher.

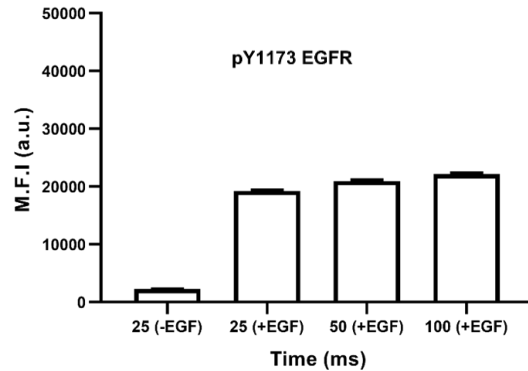


Figure 84. Median fluorescence intensity of total phosphorylation of pY1173 (includes the baseline phosphorylation) at 25 (-EGF), 25, 50 and 100 ms in the presents of EGF. Error bars indicate SEM. (Collected cells per time point = 500, number of repeats =1).

The data were corrected for the baseline phosphorylation and was observed that Y1173 was phosphorylated after being stimulated and incubated for 25 ms (Figure 85). At 50 ms, Y1173 remained phosphorylated. The phosphorylation levels of Y1173 were gradually increased at 100 ms and there was a significant difference compared to the phosphorylation at 25 ms ($p=0.0111$) and 50 ms ($p=0.0024$, Figure 85). It was confirmed that the microfluidic devices can be used to achieve and preserve sub-second phosphorylation of EGFR.

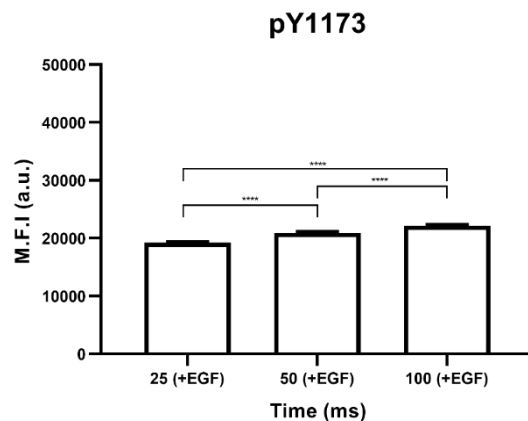


Figure 85. Median fluorescence intensity of total phosphorylation of pY1173 (baseline phosphorylation subtracted) at 25, 50 and 100 ms. It was found that the phosphorylation levels of pY1173 at 25, 50 and 100 ms were gradually increasing and there was a significant difference between. **** significant ($p<0.0001$). Error bars indicate SEM. (Collected cells per time point = 500, number of repeats =1).

In the following experiment, the phosphorylation of pY1173 (including the baseline phosphorylation at 25 ms) was examined at seven different time points (25, 50, 75, 100, 250, 500, 750 ms, Figure 86). The cells transported in a 25 ms device without EGF had a baseline phosphorylation MFI 2206 A.U. The cells stimulated with EGF within the microfluidic device were characterized by increased phosphorylation levels at the Y1173. This was indicated by the histogram shifting (Figure 86).

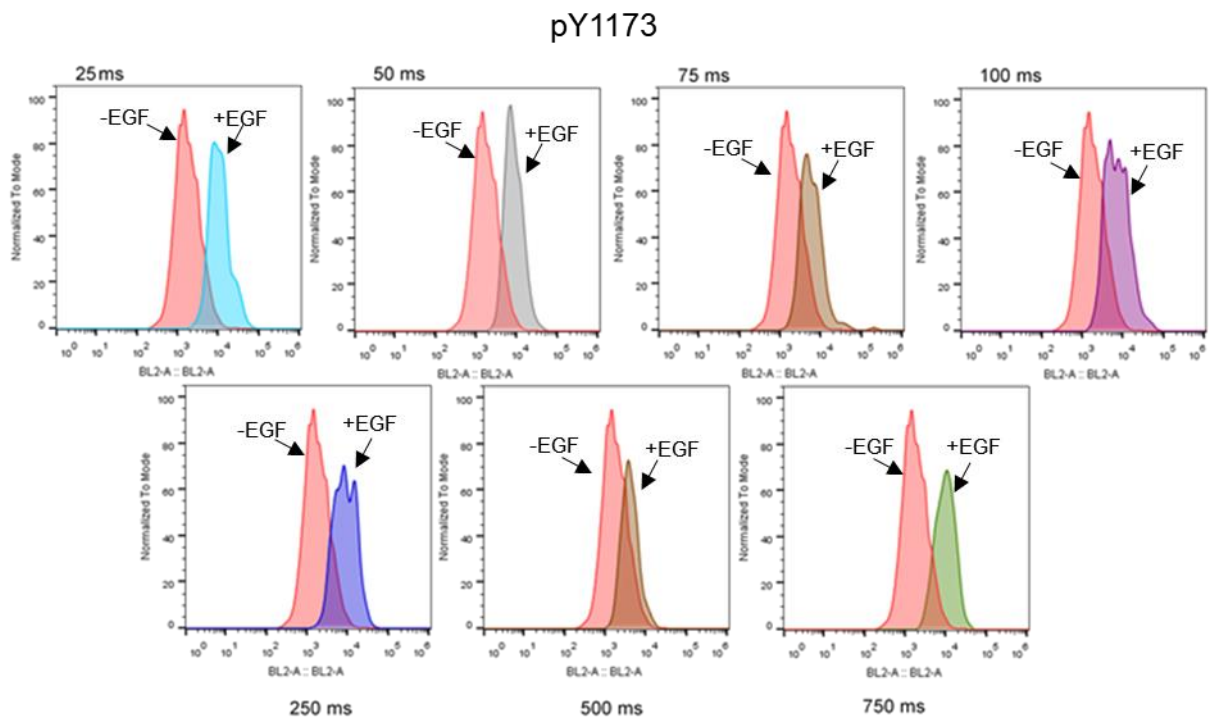


Figure 86. FACS histograms represented the phosphorylation levels of pY1173 in HeLa S3 cells. A relative increase of phosphorylation levels at Y1173 was observed on cells that were stimulated with 100 ng/mL of EGF for the seven different time points within the microfluidic devices compared to the non-stimulated cells (baseline phosphorylation). This was indicated by the histogram shifting. (Number of repeats = 1).

The baseline phosphorylation was subtracted from the primary data in order to find the phosphorylation that was increased due to EGF stimulation (Figure 87).

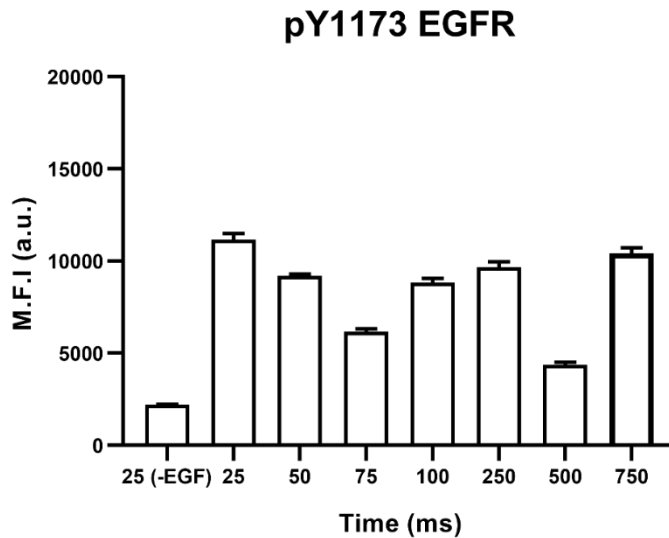


Figure 87. Median fluorescence intensity of total phosphorylation of pY1173 (includes baseline phosphorylation) at 7 different time points (25, 50, 75, 100, 250, 500 and 750 ms) was obtained using flow cell cytometry. Error bars indicate SEM. (Collected cells per time point = 500, number of repeats = 1).

It was found that there was a significant decrease ($p=0.0001$) between the phosphorylation levels at 50 ms compared to 25 ms. At the 75 ms the phosphorylation dropped by ~2-fold and there was a significant difference compared to the two previous time points (Figure 88). At 100 ms, the phosphorylation levels increased by 1093 a.u. compared to the levels at 75 ms ($p=0.0001$, Figure 88) but were lower in comparison with the levels at 25 ms and 50 ms (Figure 88). At 250 ms, the phosphorylation levels have been increased compared to the 100 ms ($p=0.0001$). The phosphorylation levels of pY1173 at 500 ms were characterized by a 3-fold decrease compared to the levels of the 250 ms ($p=0.0001$). The last time point (750 ms) showed that the phosphorylation of pY1173 was increased significantly compared to the 500 ms ($p<0.0001$). One-way ANOVA Kruskal-Wallis test (multiple comparisons) was performed for the statistical analysis of the collected data.

Expanding the time window (seven time points) provided more information on the phosphorylation events. It was found that the phosphorylation at 75 ms was significantly decreased and gradually increased at 100 ms and 250 ms. At 500 ms the phosphorylation of pY1173 was characterized by a sharp drop reaching the lowest levels compared to all the other time points (Figure 88). Surprisingly, the data obtained showed an identical pattern of phosphorylation with Ya Yu's data where the sharp dephosphorylation occurred at 500 ms.¹³

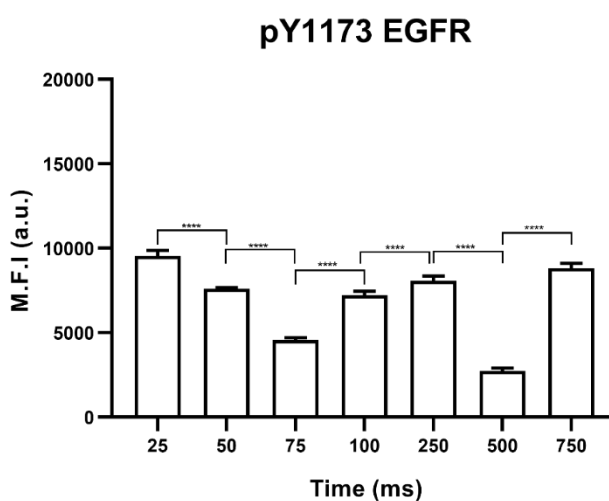


Figure 88. Median fluorescence intensity of EGF stimulated phosphorylation (baseline phosphorylation subtracted) of pY1173 at 7 different time points (25, 50, 75, 100, 250, 500 and 750 ms) obtained by using flow cell cytometry. It was found that there significant difference between the levels of phosphorylated pY1173 at 25 and 50 ms (decrease). At 75 ms the phosphorylation levels of pY1173 dropped compared to the levels at 50 ms. At 100 ms and 250 ms the levels of pY1173 gradually increased significantly. At 500 ms, there was a significant decrease (reached lowest level) at the levels of phosphorylated pY1173 compared to the previous time point. The levels of pY1173 increased at 750 ms. **** significant ($p < 0.0001$). Error bars indicate SEM. (Collected cells per time point = 500, number of repeats = 1).

In addition, the phosphorylation of EGFR pY1068 was also examined at 25 (-EGF), 25 50 and 100 ms after stimulation of cells with the ligand using flow cell cytometry (Figure 89). The negative control (red colour histogram) presented the baseline phosphorylation (Figure 89). The cells stimulated with the ligand were characterized by increased levels of phosphorylated Y1068. The median fluorescence intensity of pY1068 of the cells from each time point were plotted in a column chart for visualization purposes (Figure 90).

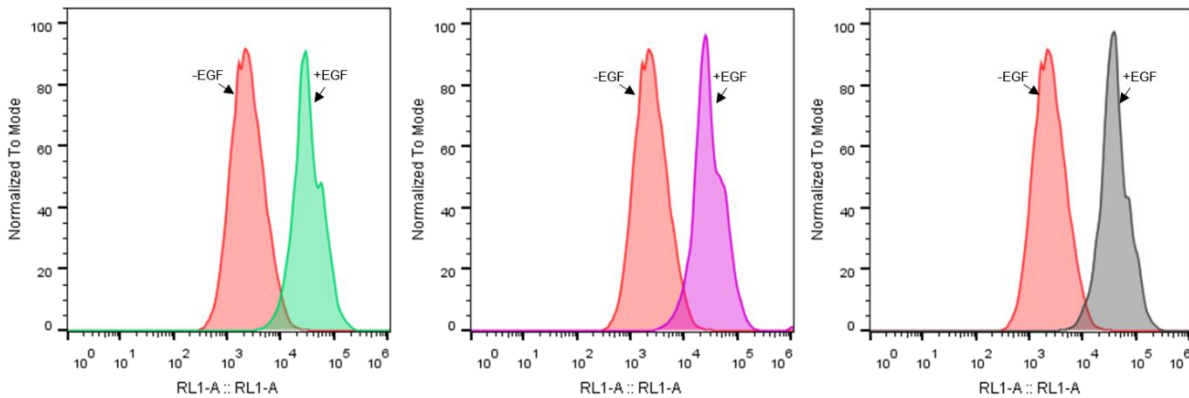


Figure 89. FACS was used to measure the fluorescence intensity of pY1068 at 25, 50 and 100 ms compared to its baseline phosphorylation (red coloured histogram). The phosphorylation levels are increased due to the stimulation with the ligand (histograms shifted to the right of the negative control). (Collected cells per time point = 500, number of repeats =1).

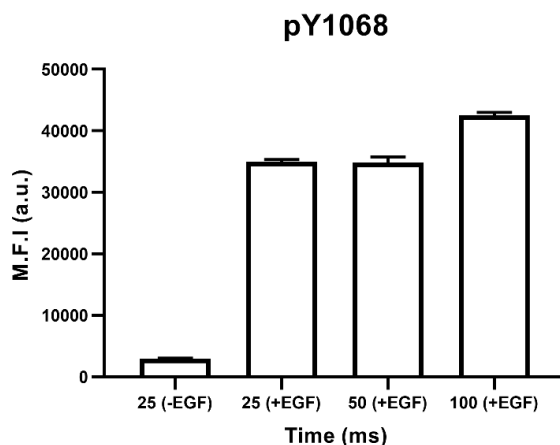


Figure 90. Median fluorescence intensity of pY1068 at 25, 50 and 100 ms compared to the baseline phosphorylation. Error bars indicate SEM, (Collected cells per time point = 500, number of repeats =1).

The data were corrected to baseline phosphorylation and it was found that the EGF induced phosphorylation was significantly different between the following time points (25, 50 and 100 ms, Figure 91).

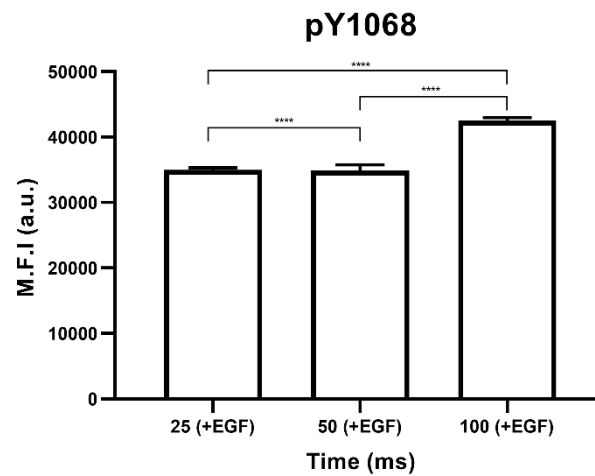


Figure 91. Median fluorescence intensity of EGF stimulated phosphorylation (baseline phosphorylation subtracted) of pY1068 at 25, 50 and 100 ms. It was found that there is significant difference between the phosphorylation levels of pY1068 at the three different time points ($p < 0.0001$). **** significant ($p < 0.0001$). Error bars indicate SEM. (Collected cells per time point = 500, number of repeats = 1).

In a second experiment, cells were stimulated with the ligand (+EGF) for the designated time points (25, 50, 75, 100, 250, 500 and 750 ms). FACS was used to determine the difference between the baseline phosphorylation of the cells (-EGF) transported in a 25 ms device and the cells stimulated with EGF (Figure 92).

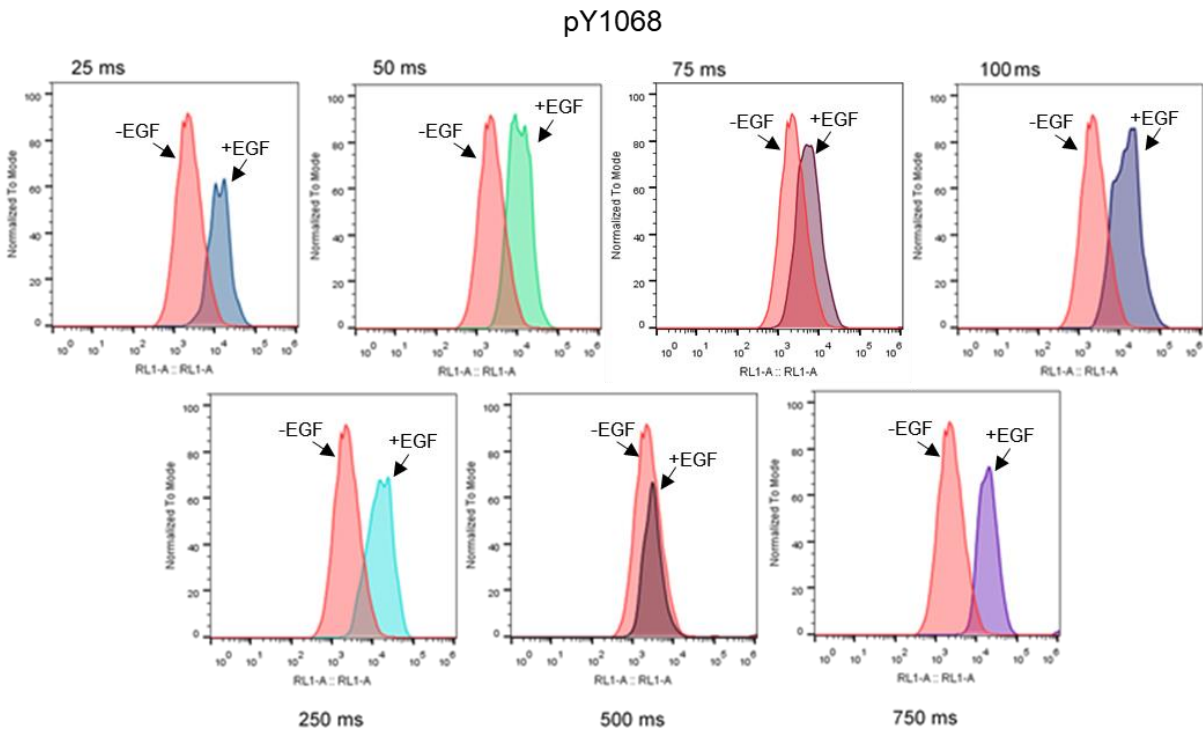


Figure 92. FACS was used to measure the phosphorylation levels of pY1068 in HeLa S3 cells. A relative increase of phosphorylation levels at Y1068 was observed on the cells which were stimulated with 100 ng/mL of EGF for seven different time points within the microfluidic devices compared to the non-stimulated cells (baseline phosphorylation). (Number of repeats = 1).

The median fluorescence intensity of pY1068 from each time point was plotted in a column chart for visualization purposes (Figure 93).

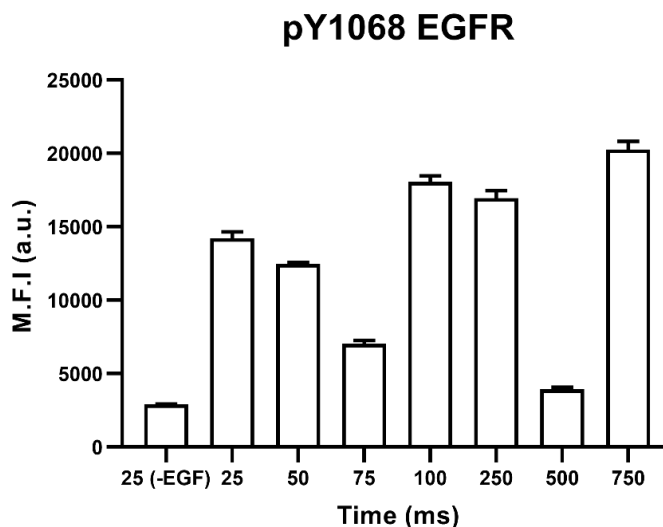


Figure 93. Median fluorescence intensity of pY1068 at 25, 50, 75, 100, 250, 500 and 750 ms. The MFI indicates the total levels of phosphorylation (baseline and EGF stimulated phosphorylation) at pY1068 in different time points. Error bars indicate SEM. (Collected cells per time point = 500, number of repeats =1).

The data were corrected for the baseline phosphorylation of pY1068 (Figure 94). The phosphorylation levels of Y1068 at 25 ms and 50 ms were characterized by a significant decrease ($p < 0.0001$). At 75 ms, the phosphorylation of pY1068 was reduced dramatically and there was a significant decrease compared to the levels at 50 ms. At 100 ms, there was a significant increase (2.4-fold) of the pY1068 phosphorylation levels compared to the levels at 75 ms time point ($p < 0.0001$). The levels at 250 ms are similar to the levels at 100 ms and there is no significant difference between them ($p > 0.9999$). The phosphorylation levels of pY1068 at 500 ms are significantly decreased ($p < 0.0001$) compared to the 250 ms. At 750 ms the phosphorylation levels are increased significantly ($p < 0.0001$, Figure 94). Compared to Ya Yu's data, the temporal pattern of pY1173 seems to be consistent with the temporal pattern of pY1068 from my data, both temporal patterns are characterized by a sharp dephosphorylation at 500 ms.¹³

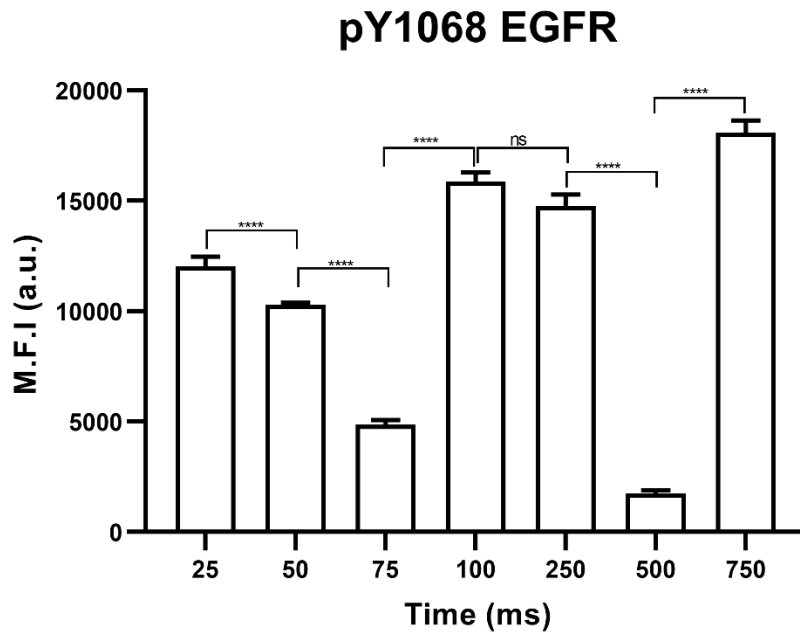


Figure 94. Median fluorescence intensity of EGF stimulated phosphorylation of pY1068 (baseline phosphorylation subtracted) at 25, 50, 75, 100, 250, 500 and 750 ms. The MFI indicates the levels of phosphorylation at pY1068 in different time points. It was observed that there is significant difference between the levels of phosphorylation at 25 and 50 ms. At 50, 75, and 100 ms the phosphorylation levels are significant. The same occurs between the 250, 500 and 750 ms. The phosphorylation levels of pY1068 at 100 ms and 250 ms are not significant. ns= not significant ($p \geq 0.05$) and **** significant ($p < 0.0001$), error bars indicate SEM. (Collected cells per time point = 500, number of repeats = 1).

The collected data from the first experiment (Section 4.3) were used to compare the M.F.I. of the phosphorylated pY1068 and pY1173 on the same cells. The phosphorylation levels of pY1068 were characterized by a significant increase compared to the phosphorylation levels of pY1173 ($p < 0.0001$, Figure 95).

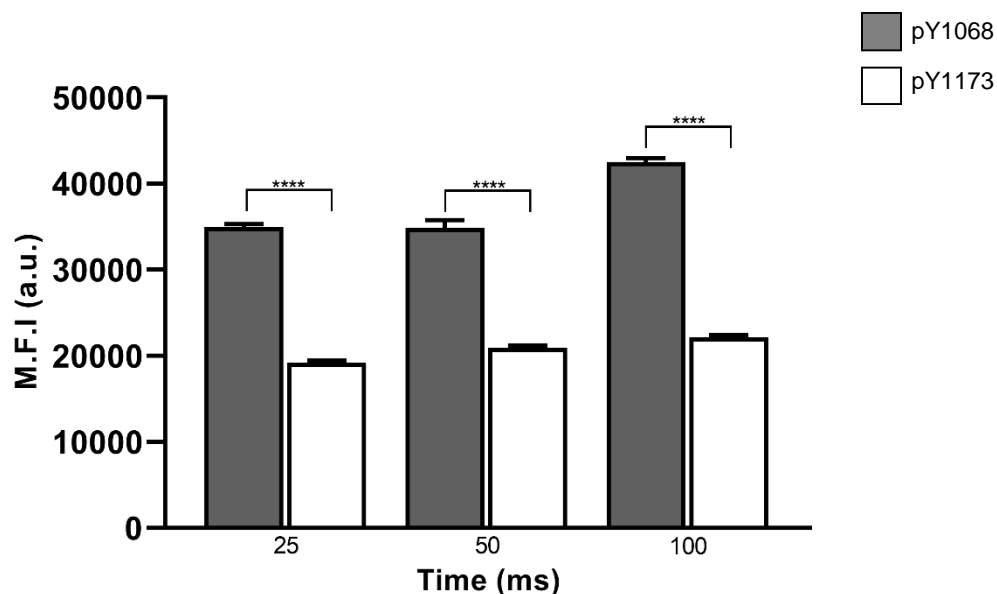


Figure 95. Median fluorescence intensity of EGF stimulated phosphorylation (baseline phosphorylation subtracted) of pY1068 and pY1173 were compared at three different time points (25, 50 and 100 ms). It was found that the levels of pY1068 are characterized by a significant increase compared to the levels of pY1173 in three different time points **** significant ($p < 0.0001$). Error bars indicate SEM, (Collected cells per time point = 500, number of repeats = 1).

In addition, the data from the second experiment (Section 4.3) were used to compare the M.F.I. of the phosphorylation levels of both tyrosine residues of the EGF receptor (Y1068 and Y1173, Figure 96). The levels of phosphorylation at 75 ms were characterized by low levels of phosphorylation with no significant difference between them ($p > 0.9999$, Figure 96). In addition, the phosphorylation of both tyrosines (Y1068 and Y1173) on the cells at 500 ms were characterized by a rapid dephosphorylation (lowest phosphorylation levels) and there is no significant difference. This phenomenon might be caused by a rapid dephosphorylation due to phosphatase activity or the tyrosine residues were occupied by other interaction partners (PLC- γ , GRB2, SHC) due to their function as docking sites. Therefore, the phosphorylation of the two tyrosine residues of the EGF receptors on the cells was prevented. Another important observation from both experiments was that the phosphorylated levels of pY1068 were higher compared to the levels of pY1173.

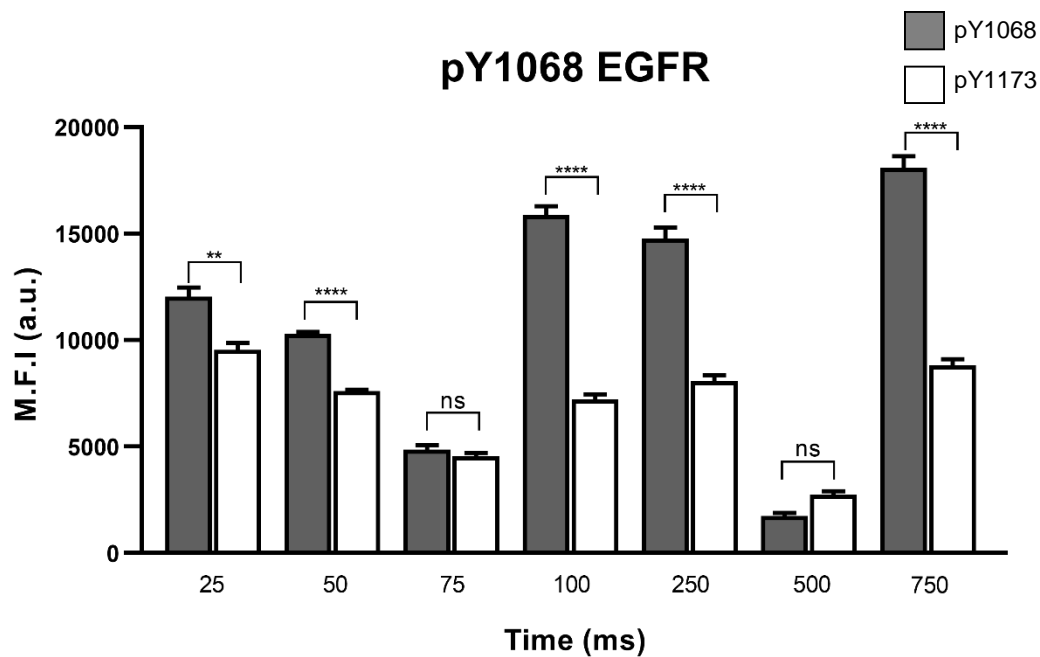


Figure 96. Median fluorescence intensity of EGF stimulated phosphorylation of pY1068 and pY1173 was compared at the same time points. It was found that there was significant difference between them at 25 ms. There was a significant difference (increased levels) of the pY1068 at 50 ms compared to the levels of pY1173. The phosphorylation levels of the two tyrosines were decreased (no significant) at the 75 ms time point. At 100 and 250 ms the pY1068 phosphorylation levels are higher compared to pY1173. The phosphorylation levels of both tyrosines were sharply decreased, reaching their lowest levels at 500 ms. At the 750 ms the phosphorylation level of both tyrosines was increased but there was a significant difference between the levels of pY1068 compared to the levels of pY1173. ns= not significant ($p \geq 0.05$), ** significant ($p = 0.001$ to 0.01), and **** significant ($p < 0.0001$). Error bars indicate SEM, (Collected cells per time point = 500, number of repeats = 1).

To summarise, the work described in this chapter was essential in order to confirm the specificity and sensitivity of the antibodies used during the Western blot analysis for detection of the different targets (pY1068, pY1173, PY20 and EGFR). Western blot analysis was not adequately sensitive due to the low protein concentration obtained from microfluidically processed cells. Therefore, developing a methodology for FACS for single cell analysis in multiplexed fashion was of a great significance because it gave the first evidence of detailed time course and unravelled new information on the phosphorylated levels of pY1068 and pY1173 in the sub second time regime.

5. Conclusion and future work

During this project, I designed, fabricated and optimized a microfluidic device that uses various microfluidic principles. This ensured high throughput (kHz) microfluidic single cell processing with incubation dwell times of 25-750 ms without damaging the cells. The use of an inertial microfluidic element allowed high efficiency of cell focusing and the use of curvatures in the incubation channel gave rise to Dean flow which allowed cells to attain uniform velocity and uniform incubation times with CV<5%. This led to precisely induce EGFR stimulation and quench the reactions in sub-second time points. Coupling with high throughput flow cytometry multiplexed receptor status analysis provided a convenient workflow to investigate the phosphorylation events that occurred during EGFR activation in sub-second timescales for the first time.

5.1 Poor temporal resolution characterises the conventional techniques used for studying EGFR phosphorylation dynamics

Biological processes are controlled by dynamic cellular signalling mechanisms (milliseconds to seconds). Despite the extensive research on the EGF receptor signalling, the immediate posttranslational changes that occur in response to the ligand binding stimulation remain obscure. Traditional biochemical techniques such as Western blot analysis, mass spectrometry revealed information on the phosphorylation however, most phosphorylation measurements have been on the timescales of several seconds up to minutes of stimulation when phosphorylation reach saturation levels. Reddy RJ and colleagues in 2016 used a mass spectrometry approach to examine the changes that occur between 10 s and 80 s resolution in response to eight different concentrations of the ligand (EGF).⁹⁰ It was found that significant changes occur as early as 10 s after stimulation. The receptor phosphorylation dynamics on Y1045, Y1068, Y1148 and Y1173 were characterised by high levels of phosphorylation.⁹⁰ A similar study was performed by Moehren and Kholodenko in 2002 where the cells were placed into vials with a Teflon stirrer and maintained the temperature at 37 °C in a water bath.¹ EGF was added by pipetting in order to stimulate the cells' receptors and preserved the reaction by the addition of the quench buffer. They managed to record early phosphorylation of EGFR events in the temporal resolution of a few seconds (1-10 s) and information on the downstream signalling pathways. However, the time required to achieve

homogenization of the large volume of reagents (ligand and quench) using a magnetic stirrer was not considered (few seconds). Therefore, these methodologies were characterized by poor temporal resolution.

5.2 The development of a circuit based on the inertial microfluidics coupled with Dean flow allowed sub-second cell stimulation and quenching

The lack of techniques that can rapidly manipulate cells to initiate and preserve these reactions gave rise to the development of a revolutionized methodology such as inertial microfluidics coupled with Dean flow. The implementation of different microfluidic elements allowed the generation of high speed and precision manipulation of cells into EGF, defined incubations and translation into PFA for rapid stimulation and preservation of EGFR intermediate phosphorylation events without affecting the membrane integrity and the capacity for authentic EGFR signal transduction. This was the first time where inertial microfluidics were used for the study of receptor activation dynamics. The use of optimal channel cross section dimensions (width 30 μm , height 65 μm) with a 2 mm length channel operating at high velocity (4 m/s) produced a switch time of 500 μs which is the fastest switch time used for cell manipulation compared to methods found in the literature (Chapter 1, p.38, Table 1). The use of Dean-coupled inertial focusing allowed uniform velocities and therefore, uniform incubation times. These microfluidic elements provided precise incubation cell control with a low velocity coefficient variation ($\text{CV} < 5\%$) for a range of velocities and channel aspect ratios required to satisfy incubation times of 25 to 2,000 ms. The study of velocity and positional evolution before and after each curvature of the incubation channel offered a better understanding of their effect and they were used for my advantage in order to achieve better cell incubation control. The identification of the correct equivalent circuit model for interpreting the pressure and resistance distribution ensure flow bifurcation to the two waste outlets.

5.3 The Inertial microfluidics coupled with Dean flow surpasses the limitations of other microfluidic techniques

A different microfluidic method that had been used to investigate the receptor activation dynamics was whole cell quenched flow analysis developed by Chiang and West in 2013.¹³ This method was an extension of Pinched flow fractionation

device developed by Yamada and colleagues in 2004 and was characterized by two stream thinning elements (STE) and an incubation channel.⁷⁵ The switch time in the first stream was 2.2 ms with a mean flow velocity of ~100 mm/s and switch time of 550 μ s in the second stream (quench stream). A multilayer fabrication was essential in order to achieve better incubation times (C.V. = 3.6%) compared to their single fabricated circuit which had a C.V. = 12.8%. Whole cell quenched flow analysis was also characterized by lower throughput (high dilution factor of cell and ligand input). Thus, the development of the Inertial microfluidic coupled with Dean flow circuit allowed higher throughput, more precise incubation control (CV=<5%) and even lower time points (25 - 2000 ms) compared to the whole cell quench flow analysis (100 - 2000 ms). Several microfluidics methods had been developed and used to examine the phosphorylation of the EGF receptor. Droplet microfluidics were used to stimulate the EGF receptor on lung cancer cells PC-9 with EGF within the droplets in order to examine the phosphorylation activity however, this method was ideal for observing only the late events (time = minutes) of phosphorylation due to the inability of the technique to quench the reaction intermediates. In addition, a high number of droplets did not contain any cells due to the inefficiency of the technique to encapsulate single cells in droplets.⁹⁴

5.4 Capturing early phosphorylation events of EGFR in sub-second time resolution

The use of Inertial microfluidic coupled with Dean flow circuits allowed rapid stimulation and quenching of the cells confirming the preservation of the phosphorylation intermediates that occur in sub-second timescales. Phosphorylation levels of pY1173 at 100 ms were increased compared to its levels at 25 and 50 ms and decreased compared to the levels of pY1068 (25, 50, 100 ms). In addition, another experiment with the microfluidic circuits showed that the phosphorylation levels of pY1068 in general are significantly increased compared to the phosphorylation levels of pY1173. An important observation from the data collected was the 75 ms time point which it was characterized by low levels of phosphorylation on both tyrosine residues (pY1068 and pY1173).

Western blot analysis of the samples collected from the microfluidic devices (100 ms and 250 ms) did not detect the levels of phosphorylation efficiently (low

signal/protein bands not visible enough) due to the low protein concentration. This was an indication that more cells are required to be collected from the microfluidic devices in order to have enough protein concentration to be detectable by Western blot analysis. In addition, protein complex immunoprecipitation (Co-IP) can be used to isolate and concentrate EGFR from the samples collected from the microfluidic devices so pY1068 and pY1173 can be detected on Western blotting analysis.

In addition, the collected data suggest a mechanism where both Y1068 to Y1173 residues are either dephosphorylated or occupied by proteins such as GRB2, SHC, PLC- γ STAT3. These proteins use the pY1068 and pY1173 tyrosine residues as docking sites in order to become phosphorylated and subsequently induce downstream signalling pathways. Thus the binding of these proteins lead to the dephosphorylation of the tyrosine residues (pY1068 and pY1173). The drop at 75 and 500 ms might be due to the activity of phosphatases (PTPs). In order to identify the cause of the drop, phosphatase inhibitors (PTPis) should be added to the cells before their stimulation with EGF. If the tyrosine residues of the cells at 75 and 500 ms are phosphorylated in the presence of the inhibitors, this is an indication that the drop is due to the phosphatases activity thus, tyrosines are getting dephosphorylated. However, if the phosphorylation levels of Y1173 and Y1068 at 75 and 500 ms remain low, even after the presence of PTPis inhibitors, this is due to the binding of protein partners which are involved in downstream signalling pathways.

5.5 pY1068 phosphorylation levels are higher compared to pY1173 not only in longer stimulation but also in sub-second stimulation times

One study performed by Erdem-Eraslan L. and colleagues examined the phosphorylation levels after EGF stimulation (5 min) by RPPA (Reverse Phase Protein Array) arrays.⁸⁶ It was found that pY1068 phosphorylation is characterized by a strong increase after stimulation with EGF and to a lesser extent the levels of pY1173 phosphorylation.⁸⁶ Importantly, the strong increase of pY1068 phosphorylation levels and to a lower degree the phosphorylation levels of pY1173 after EGF stimulation, was confirmed for the first time in our studies in sub-second time scales. In addition, the high levels of phosphorylated Y1068 were also observed by Vanmeter J. A. and colleagues in 2008 within laser capture

microdissected untreated, human non-small cell lung cancer and by Yamaoka and colleagues in 2011 when they studied the epidermal growth factor receptor autophosphorylation in mouse colon epithelial cell chemotactic migration.^{91 92} Another study by Curran and colleagues in 2015 used mass spectrometry to quantify the phosphorylation of pY1068 and pY1173 showed that the phosphorylation levels of pY1068 are higher compared to the levels of pY1173 after the stimulation of cells with EGF.⁸⁵ Also, the phosphorylation pattern may differ depending on the ligand used for stimulating EGF receptors.⁸⁵ Another study by Hartman Z. and his colleagues showed that the presence of HER2 blocks pY1068 phosphorylation on EGFR and causes increased pY1173 phosphorylation.⁸⁷ It would be interesting to examine the role of HER2 on altering the autophosphorylation patterns of EGFR in different cell lines where HER2 protein levels vary compared to EGFR levels in milliseconds time scales using my microfluidic devices. These observations raised interesting possibilities for potential pathway directed therapies.

5.6 Future work

A future experiment to consider is the use of the proximity ligation assay (PLA) to correlate receptor dimerization with the phosphorylation post-translational modifications of EGFR and investigate the role of HER2 when associated with EGFR. PLA is a method which was used to detect pY1068 phosphorylation of the EGFR.⁸⁸ This method uses two antibodies which bind simultaneously to EGFR and its phosphorylated site (e.g. pY1068). Then, a proximity ligation technique is used and coupled to an amplification reaction which detects these antibodies when they are in close proximity, indicating when the protein becomes phosphorylated (Figure 97). Further peroxidase detection and quantification of the amplified signals produced from the two antibodies are performed in a bright field microscope (Figure 97).⁸⁸ In this manner, the PLA can be used to infer the dimerization component involved in receptor activation and provide evidence for the existence of *trans* phosphorylation as well as *cis* phosphorylation.¹³

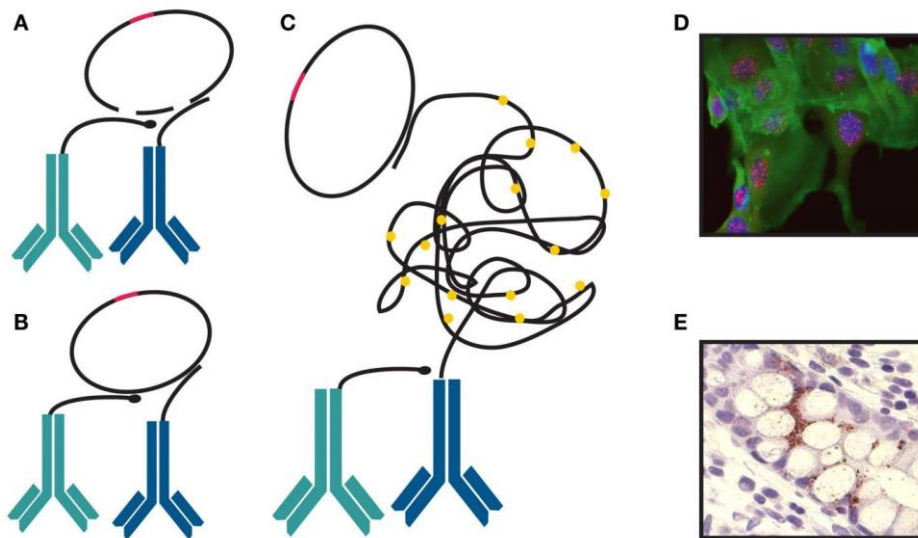


Figure 97. Two probes are in close proximity when bound to a protein or two proteins found in a protein complex (A). They are joined by a DNA ligation (circularized) after the addition of linear connector oligonucleotides and subsequently initiating rolling-circle amplification (RCA). The single stranded RCA products are labelled with oligonucleotides (C). The detection of these oligonucleotides can be done either with labelling with a fluorophore (D) or using a horse radish peroxidase label (E).

High throughput (kHz) microfluidic single cell processing, with incubation dwell times of 25-2000 ms, coupled with high throughput flow cytometry multiplexed receptor status analysis will provide a convenient workflow to investigate EGFR receptor activation dynamics. Multiplexed cytometry will be used to investigate the mechanistic role of HER2 in EGFR activation. Furthermore, the use of Mubritinib (TAK 165) an inhibitor of HER2/ErbB2 will allow us to understand the mechanistic role of HER2 in EGFR activation. This inhibitor blocks HER2 phosphorylation leading to downregulation of PI3K-Akt and MAPK pathway and it does not affect other ErbB members. Most probably, this will unravel new information on how the inhibitor acts on the phosphorylation that occurs on the milliseconds timescales. Blocking the pY1068 and pY1173 might also be an ideal way to induce apoptosis and cell death. This might be done by using Lipid polymer hybrid (LPH) nanoparticles loaded with nonapeptide (EV) mimicking the Y1068 or Y1173 site of EGFR.⁹³ This targetable lipid carrier system will deliver peptides to intracellular targets in human cancer cells and lead to the blocking of intracellular protein-protein interactions during EGFR signalling. The outcome of these reactions will provide us with valuable information on the role of pY1068 and pY1173 in the sub-second time resolution.

5.7 Conclusions

The results obtained during the duration of the project are highlighting the complexity of posttranslational modifications and provide new perspective into examining mechanistic hypotheses about the EGF receptor activation dynamics. The significance of the study of the sub-second phosphorylation sequence of events will generate new knowledge and provide strategies for the regulation of the cellular machinery understanding mechanisms underlying signalling network function providing breakthroughs in the critical controlling factors (*e.g.* phosphorylation) that will be targets for pharmacological interventions in the treatment of human diseases. In general, phosphorylation events are studied during their end points due to the inability of techniques to rapidly induce and preserve these reactions thus, the early points of phosphorylation events remain poorly elucidated. The use of microfluidics will unravel new insights in the key role of mediating cellular proliferation, ubiquitylation, calcium signalling, receptor tyrosine kinases as well as non-receptor tyrosine kinases: Src and Abl which are attractive candidates for therapeutic intervention therefore, additional information can be used for developing targeted therapeutics and establish a sequential map of these early events. In addition, the device can be optimized even further in order to surpass its limits and reach even shorter time scales (2.5, 5, 7.5, 10, 12.5, 15, 20 ms) allowing to investigate the receptor dynamics immediately after the binding of the ligand. The examination of these biochemical changes in the context of the full signalling network will provide a better understanding of the network behaviour. The microfluidic device is applicable for a variety of cells and examine different biological questions. Combining this method with tools that can make precise and high throughput measurements will improve our understanding of signalling systems and explored them in an unbiased manner, allowing novel cell signalling networks to be identified and create large-scale of atlases with potential directed therapies.

6. References

1. Moehren G, Markevich N, Demin O, Kiyatkin A, Goryanin I, Hoek JB, Kholodenko BN. Temperature dependence of the epidermal growth factor receptor signaling network can be accounted for by a kinetic model. *Biochemistry* 2002;41(1):306-20.
2. Shostak K, Chariot A. EGFR and NF-kappaB: partners in cancer. *Trends in Molecular Medicine* 2015;21(6):385-93.
3. Burgess AW, Cho HS, Eigenbrot C, Ferguson KM, Garrett TP, Leahy DJ, Lemmon MA, Sliwkowski MX, Ward CW, Yokoyama S. An open-and-shut case? Recent insights into the activation of EGF/ErbB receptors. *Molecular Cell* 2003;12(3):541-52.
4. Yewale C, Baradia D, Vhora I, Patil S, Misra A. Epidermal growth factor receptor targeting in cancer: a review of trends and strategies. *Biomaterials* 2013;34(34):8690-707.
5. Dengjel J, Akimov V, Olsen JV, Bunkenborg J, Mann M, Blagoev B, Andersen JS. Quantitative proteomic assessment of very early cellular signaling events. *Nature Biotechnology* 2007;25(5):566-8.
6. Malnasi-Csizmadia A, Pearson DS, Kovacs M, Woolley J. R., Geeves A. M., Bagshaw R. C. Kinetic resolution of a conformational transition and the ATP hydrolysis step using relaxation methods with a Dictyostelium myosin II mutant containing a single tryptophan residue. *Biochemistry* 2001;40(42):12727-37.
7. Berg JM, Tymoczko JL, Stryer L. *Biochemistry*. Basingstoke: W.H. Freeman 2012.
8. Wong QY, Liu N, Koh C-G, Li H-Y, Lew W. S. Isolation of magnetically tagged cancer cells through an integrated magnetofluidic device. *Microfluidics and Nanofluidics* 2016;20(10):139.
9. Di Carlo D. Inertial microfluidics. *Lab on a Chip* 2009;9(21):3038-46.
10. Zmijan R, Jonnalagadda US, Carugo D, Kochi Y, Lemm E, Packham G, Hilla M and Glynne-Jones P. High throughput imaging cytometer with acoustic focusing. *RSC Advances* 2015;5(101):83206-16.
11. Song H, Ismagilov RF. Millisecond kinetics on a microfluidic chip using nanoliters of reagents. *Journal of the American Chemical Society* 2003;125(47):14613-9.
12. Gossett DR, Weaver WM, Mach AJ, Hur SC, Tse HT, Lee W, Amini H, Di Carlo D. Label-free cell separation and sorting in microfluidic systems. *Analytical and Bioanalytical Chemistry* 2010;397(8):3249-67.
13. Chiang YY, West J. Ultrafast cell switching for recording cell surface transitions: new insights into epidermal growth factor receptor signalling. *Lab on a Chip* 2013;13(6):1031-4.
14. Chiang YY, Haeri S, Gizewski C, Stewart JD, Ehrhard P, Shrimpton J, Janasek D, West J. Whole cell quenched flow analysis. *Analytical Chemistry* 2013;85(23):11560-7.
15. Sharma SV, Bell DW, Settleman J, Haber DA. Epidermal growth factor receptor mutations in lung cancer. *Nature Reviews Cancer* 2007;7(3):169-81.
16. Fidalgo LM, Abell C, Huck WT. Surface-induced droplet fusion in microfluidic devices. *Lab on a Chip* 2007;7(8):984-6.

17. Cho S, Kang DK, Sim S, Geier F, Kim JY, Niu X, Edel JB, Chang SI, Wootton RC, Elvira KS, deMello AJ. Droplet-based microfluidic platform for high-throughput, multi-parameter screening of photosensitizer activity. *Analytical Chemistry* 2013;85(18):8866-72.
18. Herbst RS. Review of epidermal growth factor receptor biology. *International Journal of Radiation Oncology, Biology, Physics* 2004;59(2 Suppl):21-6.
19. Lemmon MA, Schlessinger J. Cell signaling by receptor tyrosine kinases. *Cell* 2010;141(7):1117-34.
20. Seger U, Gawad S, Johann R, Bertsch A, Renaud P. Cell immersion and cell dipping in microfluidic devices. *Lab on a Chip* 2004;4(2):148-51.
21. Miettinen PJ, Berger JE, Meneses J, Phung Y, Pedersen RA, Werb Z, Derynck R. Epithelial immaturity and multiorgan failure in mice lacking epidermal growth factor receptor. *Nature* 1995;376(6538):337-41.
22. Takeyama K, Dabbagh K, Lee HM, Agustí C, Lausier JA, Ueki IF, Grattan KM, Nadel JA. Epidermal growth factor system regulates mucin production in airways. *Proceedings of the National Academy of Sciences of the United States of America* 1999;96(6):3081-6.
23. Salomon DS, Brandt R, Ciardiello F, Normanno N. Epidermal growth factor-related peptides and their receptors in human malignancies. *Critical reviews in Oncology/Hematology* 1995;19(3):183-232.
24. Normanno N, De Luca A, Bianco C, Strizzi L, Mancino M, Maiello MR, Carotenuto A, De Feo G, Caponigro F, Salomon DS. Epidermal growth factor receptor (EGFR) signaling in cancer. *Gene* 2006;366(1):2-16.
25. Gschwind A, Fischer OM, Ullrich A. The discovery of receptor tyrosine kinases: targets for cancer therapy. *Nature Reviews Cancer* 2004;4(5):361-70.
26. Yarden Y. The EGFR family and its ligands in human cancer: signalling mechanisms and therapeutic opportunities. *European Journal of Cancer* 1990;2001:37
27. Yarden Y, Sliwkowski MX. Untangling the ErbB signalling network. *Nature Reviews Molecular Cell Biology* 2001;2(2):127-37.
28. Lenferink AE, Pinkas-Kramarski R, van de Poll ML, van Vugt MJ, Klapper LN, Tzahar E, Waterman H, Sela M, van Zoelen EJ, Yarden Y. Differential endocytic routing of homo- and hetero-dimeric ErbB tyrosine kinases confers signaling superiority to receptor heterodimers. *The EMBO Journal* 1998;17(12):3385-97.
29. Amin DN, Campbell MR, Moasser MM. The role of HER3, the unpretentious member of the HER family, in cancer biology and cancer therapeutics. *Seminars in Cell & Developmental Biology* 2010;21(9):944-50.
30. Arteaga CL, Engelman JA. ERBB receptors: from oncogene discovery to basic science to mechanism-based cancer therapeutics. *Cancer Cell* 2014;25(3):282-303.
31. Monsey J, Shen W, Schlessinger P, Bose R. Her4 and Her2/neu tyrosine kinase domains dimerize and activate in a reconstituted *in vitro* system. *The Journal of Biological Chemistry* 2010;285(10):7035-44.
32. Olayioye MA, Neve RM, Lane HA, Hynes NE. The ErbB signaling network: receptor heterodimerization in development and cancer. *The EMBO Journal* 2000;19(13):3159-67.
33. Koland JG. Coarse-grained molecular simulation of epidermal growth factor receptor protein tyrosine kinase multi-site self-phosphorylation. *PLoS Computational Biology* 2014;10(1):e1003435-e35.

34. Bessman NJ, Bagchi A, Ferguson KM, Lemmon MA. Complex relationship between ligand binding and dimerization in the epidermal growth factor receptor. *Cell Reports* 2014;9(4):130617.
35. Bessman NJ, Lemmon MA. Finding the missing links in EGFR. *Nature Structural & Molecular Biology* 2012;19(1):1-3.
36. Macdonald-Obermann JL, Pike LJ. Different epidermal growth factor (EGF) receptor ligands show distinct kinetics and biased or partial agonism for homodimer and heterodimer formation. *The Journal of Biological Chemistry* 2014;289(38):26178-88.
37. Lemmon MA, Schlessinger J, Ferguson KM. The EGFR family: not so prototypical receptor tyrosine kinases. *Cold Spring Harbor Perspectives in Biology* 2014;6(4):a020768.
38. Schulze WX, Deng L, Mann M. Phosphotyrosine interactome of the ErbB-receptor kinase family. *Molecular Systems Biology* 2005;1:2005.0008.
39. Chalhoub N, Baker SJ. PTEN and the PI3-kinase pathway in cancer. *Annual Review of Pathology* 2009;4:127-50.
40. Wilson KJ, Gilmore JL, Foley J, Lemmon MA, Riese DJ. Functional selectivity of EGF family peptide growth factors: implications for cancer. *Pharmacology & Therapeutics* 2009;122(1):1-8.
41. Sorkin A, Mazzotti M, Sorkina T, Scotto L, Beguinot L. Epidermal growth factor receptor interaction with clathrin adaptors is mediated by the Tyr974-containing internalization motif. *The Journal of Biological Chemistry* 1996;271(23):13377-84.
42. Garrett TP, McKern NM, Lou M, Elleman TC, Adams TE, Lovrecz GO, Zhu HJ, Walker F, Frenkel MJ, Hoyne PA, Jorissen RN, Nice EC, Burgess AW, Ward CW. Crystal structure of a truncated epidermal growth factor receptor extracellular domain bound to transforming growth factor alpha. *Cell* 2002;110(6):763-73.
43. Ogiso H, Ishitani R, Nureki O, Fukai S, Yamanaka M, Kim JH, Saito K, Sakamoto A, Inoue M, Shirouzu M, Yokoyama S. Crystal structure of the complex of human epidermal growth factor and receptor extracellular domains. *Cell* 2002;110(6):775-87.
44. Lynch TJ, Bell DW, Sordella R, Gurubhagavatula S, Okimoto RA, Brannigan BW, Harris PL, Haserlat SM, Supko JG, Haluska FG, Louis DN, Christiani DC, Settleman J, Haber DA. Activating mutations in the epidermal growth factor receptor underlying responsiveness of non-small-cell lung cancer to gefitinib. *The New England Journal of Medicine* 2004;350(21):2129-39.
45. Wu SL, Kim J, Bandle RW, Liotta L, Petricoin E, Karger BL. Dynamic profiling of the posttranslational modifications and interaction partners of epidermal growth factor receptor signaling after stimulation by epidermal growth factor using Extended Range Proteomic Analysis (ERPA). *Molecular & Cellular Proteomics* 2006;5(9):1610-27.
46. Wu SL, Kim J, Hancock WS, Karger B. Extended Range Proteomic Analysis (ERPA): a new and sensitive LC-MS platform for high sequence coverage of complex proteins with extensive post-translational modifications-comprehensive analysis of beta-casein and epidermal growth factor receptor (EGFR). *Journal of Proteome Research* 2005;4(4):1155-70.
47. Tong J, Taylor P, Jovceva E, St-Germain JR, Jin LL, Nikolic A, Gu X, Li ZH, Trudel S, Moran MF. Tandem immunoprecipitation of phosphotyrosine-mass spectrometry (TIPY-MS) indicates C19ORF19 becomes tyrosine-phosphorylated and associated with activated epidermal growth factor receptor. *Journal of Proteome Research* 2008;7(3):1067-77.

48. Rikova K, Guo A, Zeng Q, Possemato A, Yu J, Haack H, Nardone J, Lee K, Reeves C, Li Y, Hu Y, Tan Z, Stokes M, Sullivan L, Mitchell J, Wetzel R, Macneill J, Ren JM, Yuan J, Bakalarski CE, Villen J, Kornhauser JM, Smith B, Li D, Zhou X, Gygi SP, Gu TL, Polakiewicz RD, Rush J, Comb MJ. Global survey of phosphotyrosine signaling identifies oncogenic kinases in lung cancer. *Cell* 2007;131(6):1190-203.
49. Macek B, Mann M, Olsen JV. Global and site-specific quantitative phosphoproteomics: principles and applications. *Annual Review of Pharmacology and Toxicology* 2009;49:199221.
50. Padilla-Parra S, Tramier M. FRET microscopy in the living cell: Different approaches, strengths and weaknesses. *BioEssays* 2012;34(5):369-76.
51. Leray A, Padilla-Parra S, Roul J, Hélot L, Tramier M. Spatio-Temporal Quantification of FRET in living cells by fast time-domain FLIM: a comparative study of non-fitting methods. *PLoS One* 2013;8(7):e69335.
52. Becker W. Fluorescence lifetime imaging--techniques and applications. *Journal of Microscopy* 2012;247(2):119-36.
53. Reynolds AR, Tischer C, Verveer PJ, Rocks O, Bastiaens PI. EGFR activation coupled to inhibition of tyrosine phosphatases causes lateral signal propagation. *Nature Cell Biology* 2003;5(5):447-53.
54. Gibson QH, Greenwood C. Kinetic observations on the near infrared band of cytochrome C oxidase. *The Journal of Biological Chemistry* 1965;240:2694-8.
55. Fersht AR, Jakes R. Demonstration of two reaction pathways for the aminoacylation of tRNA. Application of the pulsed quenched flow technique. *Biochemistry* 1975;14(15):3350-6.
56. Ikeguchi M, Kuwajima K, Mitani M, Sugai S. Evidence for identity between the equilibrium unfolding intermediate and a transient folding intermediate: a comparative study of the folding reactions of α -lactalbumin and lysozyme. *Biochemistry* 1986;25(22):6965-72.
57. Tanford C, Aune KC. Thermodynamics of the denaturation of lysozyme by guanidine hydrochloride. III. Dependence on temperature. *Biochemistry* 1970;9(2):206-11.
58. Hu W, Berdugo C, Chalmers JJ. The potential of hydrodynamic damage to animal cells of industrial relevance: current understanding. *Cytotechnology* 2011;63(5):445-60.
59. Knoll G, Braun C, Plattner H. Quenched flow analysis of exocytosis in *Paramecium* cells: time course, changes in membrane structure, and calcium requirements revealed after rapid mixing and rapid freezing of intact cells. *The Journal of Cell Biology* 1991;113(6):1295-304.
60. Secko D. Protein phosphorylation: A global regulator of cellular activity. *The Science Creative Quarterly* 2003.
61. Whitesides GM. The origins and the future of microfluidics. *Nature* 2006;442(7101):36873.
62. Niu X, Gielen F, deMello AJ, Edel JB. Electro-coalescence of digitally controlled droplets. *Analytical Chemistry* 2009;81(17):7321-5.
63. Ashkin A. Forces of a single-beam gradient laser trap on a dielectric sphere in the ray optics regime. *Biophysical Journal* 1992;61(2):569-82.

64. Eriksson E, Enger J, Nordlander B, Erjavec N, Ramser K, Goksör M, Hohmann S, Nyström T, Hanstorp D. A microfluidic system in combination with optical tweezers for analyzing rapid and reversible cytological alterations in single cells upon environmental changes. *Lab on a Chip* 2007;7(1):71-6.
65. Wong HMK, Righini M, Gates JC, Smith R. G. P. Pruneri V., Quidant R., On-a-chip surface plasmon tweezers. *Applied Physics Letters* 2011;99(6):061107.
66. Pamme N, Manz A. On-chip free-flow magnetophoresis: continuous flow separation of magnetic particles and agglomerates. *Analytical Chemistry* 2004;76(24):7250-6.
67. Sasso LA, Johnston IH, Zheng M, Gupte RK, Ündar A, Zahn JD. Automated microfluidic processing platform for multiplexed magnetic bead immunoassays. *Microfluidics and Nanofluidics* 2012;13(4):603-12.
68. Lenshof A, Magnusson C, Laurell T. Acoustofluidics 8: Applications of acoustophoresis in continuous flow microsystems. *Lab on a Chip* 2012;12(7):1210-23.
69. Augustsson P, Malm J, Ekström S. Acoustophoretic microfluidic chip for sequential elution of surface bound molecules from beads or cells. *Biomicrofluidics* 2012;6(3):34115.
70. Liu Z, Huang F, Du J, Shu W, Feng H, Xu X, Chen Y. Rapid isolation of cancer cells using microfluidic deterministic lateral displacement structure. *Biomicrofluidics* 2013;7(1):11801.
71. Holm SH, Beech JP, Barrett MP, Tegenfeldt JO. Separation of parasites from human blood using deterministic lateral displacement. *Lab on a Chip* 2011;11(7):1326-32.
72. Beech JP, Holm SH, Adolfsson K, Tegenfeldt JO. Sorting cells by size, shape and deformability. *Lab on a Chip* 2012;12(6):1048-51.
73. Inglis DW, Morton KJ, Davis JA, Zieziulewicz TJ, Lawrence DA, Austin RH, Sturm JC. Microfluidic device for label-free measurement of platelet activation. *Lab on a Chip* 2008;8(6):925-31.
74. Morton KJ, Louthback K, Inglis DW, Tsui OK, Sturm JC, Chou SY, Austin RH. Crossing microfluidic streamlines to lyse, label and wash cells. *Lab on a Chip* 2008;8(9):1448-53.
75. Yamada M, Nakashima M, Seki M. Pinched flow fractionation: continuous size separation of particles utilizing a laminar flow profile in a pinched microchannel. *Analytical Chemistry* 2004;76(18):5465-71.
76. Amini H, Lee W, Di Carlo D. Inertial microfluidic physics. *Lab on a Chip* 2014;14(15):273961.
77. Mach AJ, Adeyiga OB, Di Carlo D. Microfluidic sample preparation for diagnostic cytopathology. *Lab on a Chip* 2013;13(6):1011-26.
78. Tan AP, Dudani JS, Arshi A, Lee RJ, Tse HT, Gossett DR, Di Carlo D. Continuous-flow cytomorphological staining and analysis. *Lab on a Chip* 2014;14(3):522-31.
79. Bhagat AA, Bow H, Hou HW, Tan SJ, Han J, Lim CT. Microfluidics for cell separation. *Medical & Biological Engineering & Computing* 2010;48(10):999-1014.
80. Ramachandraiah H, Ardabili S, Faridi AM, Gantelius J, Kowalewski JM, Mårtensson G, Russom A. Dean flow-coupled inertial focusing in curved channels. *Biomicrofluidics* 2014;8(3):034117.

81. Martel JM, Toner M. Particle Focusing in Curved Microfluidic Channels. *Scientific Reports* 2013;3:3340. 82. Paiè P, Bragheri F, Di Carlo D, Osellame R. Particle focusing by 3D inertial microfluidics. *Microsystems and Nanoengineering* 2017;3:17027.
83. Jørgensen PE, Eskildsen L, Nexø E. Adsorption of EGF receptor ligands to test tubes ? a factor with implications for studies on the potency of these peptides. *Scandinavian Journal of Clinical and Laboratory Investigation* 1999;59(3):191-97.
84. Ge G, Wu J, Lin Q. Effect of Membrane Fluidity on Tyrosine Kinase Activity of Reconstituted Epidermal Growth Factor Receptor. *Biochemical and Biophysical Research Communications* 2001;282(2):511-14.
85. Curran TG, Zhang Y, Ma DJ, Sarkaria JN, White FM. MARQUIS: A multiplex method for absolute quantification of peptides and posttranslational modifications. *Nature Communications* 2015;6:5924. 86. Erdem-Eraslan L, Gao Y, Kloosterhof NK, Atlasi Y, Demmers J, Sacchetti A, Kros JM, Sillevius Smitt P, Aerts J, French PJ. Mutation specific functions of EGFR result in a mutationspecific downstream pathway activation. *European Journal of Cancer* 2015;51(7):893-903.
87. Hartman Z, Zhao H, Agazie YM. HER2 stabilizes EGFR and itself by altering autophosphorylation patterns in a manner that overcomes regulatory mechanisms and promotes proliferative and transformation signaling. *Oncogene* 2013;32(35):4169-80.
88. Halle C, Lando M, Sundfør K, Kristensen GB, Holm R, Lyng H. Phosphorylation of EGFR measured with in situ proximity ligation assay: relationship to EGFR protein level and gene dosage in cervical cancer. *Radiotherapy and Oncology : Journal of the European Society for Therapeutic Radiology and Oncology* 2011;101(1):152-7.
89. Oh KW, Lee K, Ahn B, Furlani EP. Design of pressure-driven microfluidic networks using electric circuit analogy. *Lab on a Chip* 2012;7;12(3):515-45.
90. Reddy RJ, Gajadhar AS, Swenson EJ, Rothenberg DA, Curran TG, White FM. Early signalling dynamics of the epidermal growth factor receptor. *Proceedings of the National Academy of Sciences of the United States of America* 2016;113(11):3114-9.
91. VanMeter AJ, Rodriguez AS, Bowman ED, Jen J, Harris CC, Deng J, Calvert VS, Silvestri A, Fredolini C, Chandhoke V, Petricoin EF 3rd, Liotta LA, Espina V. Laser capture microdissection and protein microarray analysis of human non-small cell lung cancer: differential epidermal growth factor receptor (EGFR) phosphorylation events associated with mutated EGFR compared with wild type. *Molecular & Cell Proteomics* 2008;7(10):1902-24.
92. Yamaoka T, Frey MR, Dise RS, Bernard JK, Polk DB. Specific epidermal growth factor receptor autophosphorylation sites promote mouse colon epithelial cell chemotaxis and restitution. *American Journal of Physiology Gastrointestinal and Liver Physiology* 2011;301(2):368-76.
93. Kim SK, Huang L. Nanoparticle delivery of a peptide targeting EGFR signaling. *Journal of Controlled Release* 2012;157(2):279-86.
94. Ramji R, Wang M, Bhagat AA, Tan Shao Weng D, Thakor NV, Teck Lim C, Chen CH. Single cell kinase signaling assay using pinched flow coupled droplet microfluidics. *Biomicrofluidics* 2014;8(3):034104.
95. Krutzik PO, Nolan GP. Intracellular phospho-protein staining techniques for flow cytometry: monitoring single cell signalling events. *Cytometry A*, 2003;55(2):61-70.

96. Krutzik PO, Irish JM, Nolan GP, Perez OD. Analysis of protein phosphorylation and cellular signaling events by flow cytometry: techniques and clinical applications. *Clinical Immunology* 2004;110(3):206-21